ORIGIN OF THE INERTIAL ANOMALY IN SOLID HELIUM-4: DISLOCATION DYNAMICS VERSUS SUPERSOLIDITY

A Dissertation

Presented to the Faculty of the Graduate School

of Cornell University

in Partial Fulfillment of the Requirements for the Degree of

Doctor of Philosophy

by

Vikram Gadagkar

May 2013

ORIGIN OF THE INERTIAL ANOMALY IN SOLID HELIUM-4: DISLOCATION DYNAMICS VERSUS SUPERSOLIDITY

Vikram Gadagkar, Ph.D.

Cornell University 2013

Solid ^{4}He has been a considered a candidate supersolid, a bosonic crystal with an interpenetrating superfluid component, since 1969. It was not until 2004 however, that Kim and Chan observed an increase in the resonance frequency of torsional oscillators (TO) containing solid ^{4}He, an observation they interpreted as due to mass decoupling and hence as the first evidence for supersolidity.

We introduced a novel SQUID-based TO technique with increased sensitivity and dynamic range, and the generalized rotational susceptibility framework to study TOs containing solid ^{4}He. Below ~250 mK, the TO resonance frequency f increases and its dissipation D passes through a maximum as first reported by Kim and Chan. We found that equilibration times within $f(T)$ and $D(T)$ exhibit a complex synchronized ultraslow evolution toward equilibrium indicative of glassy freezing of crystal disorder conformations which strongly influence the rotational dynamics.

Then, by introducing the free inertial decay (FID) technique to solid ^{4}He TO studies, we carried out a comprehensive map of $f(T,a)$ and $D(T,a)$ where a is the maximum TO rim acceleration. These data indicated that the same microscopic excitations controlling the TO motions are generated independently by thermal and mechanical stimulation of the crystal and moreover, a measure for their relaxation times $\tau(T,a)$ diverges smoothly everywhere without exhibiting a critical temperature or velocity expected for a superfluid-like transition.

Following the observations of Day and Beamish, we showed that the combined

temperature-acceleration dependence of the TO response is indistinguishable from the combined temperature-strain dependence of the ^{4}He shear modulus. Together, these observations imply that ultra-slow equilibration of crystal disorder conformations controls the rotational dynamics and, for any given disorder conformation, the anomalous rotational responses of solid ^{4}He are associated with generation of the same microscopic excitations as those produced by direct shear strain.

We report a new apparatus for directly detecting mass flow where the pressure is applied electrostatically throughout the sample by enclosing a reservoir of helium between two plates of a capacitor. Mass flow can be detected by monitoring the capacitance of a second reservoir connected to the first by a set of tubes. We first establish a mass flow detection scheme by measuring acoustic resonances when the apparatus is filled with superfluid ^{4}He. This acoustic resonance technique provides an opportunity to search for AC mass flow in the kilohertz range, which is comparable to torsional oscillator frequencies. We find no evidence for superflow when the apparatus is filled with solid ^{4}He.

We have developed a new dislocation-vibration model starting with Iwasa's model to obtain both the temperature and acceleration dependence (through an acceleration-dependent binding energy) of the frequency shift and dissipation observed in TO experiments on solid ^{4}He. We provide a physical basis for the initially surprising result that temperature and acceleration have similar effects on the frequency and dissipation. The model captures almost all the essential features of the frequency shift and dissipation over the entire temperature-acceleration plane. This result, along with the argument that there is no evidence for a superfluid-like transition in the relaxation times or superflow provides strong support for dislocation-vibration being the microscopic excitations responsible for the inertial anomaly first reported by Kim and Chan.

BIOGRAPHICAL SKETCH

Vikram was born in Bangalore, India and grew up in the beautiful campus of the Indian Institute of Science. His interest in science was kindled very early through the strong influence of his father and he spent most of his childhood exploring the lives of birds, insects, snakes and other creatures that also called the campus their home.

When he was in high school, he attended a lecture by the famous neuroscientist Professor V. S. Ramachandran, which left him so inspired that he has since dreamed of one day unraveling the mysteries of the brain. With this long-term goal at the back of his mind, but with the conviction that the tools and insights that will ultimately crack the puzzles of neuroscience will come increasingly from physics, chemistry, and mathematics, he chose these very subjects to study formally for his bachelors degree at St. Joseph's College, Bangalore, while studying Biology informally in the evolutionary biology lab of Professor Amitabh Joshi.

He subsequently settled on physics, seduced by the physicist's way of thinking, for his masters degree at the Indian Institute of Science working with Professor Ajay Sood for his thesis. Here he used large-scale parallel computing molecular dynamics simulations and optical methods such as Raman scattering to study the mechanical properties of single- and double-walled carbon and boron-nitride nanotubes.

Having decided it was time to see the world, he flew across the globe to Ithaca, NY and immediately fell in love with this charming little place. He soon began work as a graduate student with Professor Séamus Davis at Cornell Physics, in whose labs he and his colleagues investigated the origin the putative 'supersolid' phase in solid helium. He feels the time has finally come to apply his knowledge of experimental physics to problems in neuroscience and his first step is this direction is to help build a brand new neuroscience lab as Professor Jesse Goldberg's first postdoc, also at Cornell.

To the “White House” and all the souls that pass through it

ACKNOWLEDGEMENTS

I could not have asked for a better advisor than Séamus Davis whose unwavering focus on only the most important questions, unbounded energy and enthusiasm and quick insights are truly inspiring. I thank Erich Mueller and Jeevak Parpia who have been on my special committee from the beginning and have always been immensely supportive and have had the most excellent advice.

I consider myself extremely lucky to have had the opportunity to work closely with Ethan Pratt, Ben Hunt, and Ethan Kassner, my primary collaborators. I'm grateful to Minoru Yamashita for building a fine cryostat and to Matthias Graf and Sasha Balatsky, our colleagues at Los Alamos National Labs. It was great fun mentoring Neal Harrington, Jim McArdle, and Praveen Narayanan while they were undergrad researchers in our lab. I have greatly enjoyed talking physics with Jim Sethna over the last few months and hope to continue to do so for a long time to come and John Reppy never ceases to be an inspiration.

A special thank you to Marco Aprili for going over my B Exam talk for 4 hours on a Friday afternoon. Many thanks to Milan Allan and Ming Chuang for never failing to make me smile and to Jean-Philippe Reid for his stress busting home remedies of exercise, herbal tea drinking, and other more interesting activities. The ups and downs of graduate life were celebrated and tolerated with a bunch of amazing people that made up the rest of the Davis Group during my time here - Jacob Alldredge, Warasinee Chaisangmongkon, Stephen Edkins, Inês Firmo, Kazu Fujita, Chris Gerig, Mo Hamidian, Chung Koo Kim, Andrey 'Neo' Kostin, Jinho Lee, Inhee Lee, Jhinhwan Lee, Freek Massee, Focko Meier, Hiro Miyaki, Sourin Mukhopadhyay, Andreas Rost, Andy Schmidt, Peter Sparu, Curry Taylor, Peter Wahl, Alfred Wang, Yang Xie, Jerry Yoon, and many others. I also greatly treasure the interactions I've had with the many undergrads, graduate students, postdocs and faculty in the Physics Department over the years.

Great research is possible at Cornell Physics in large part due to the excellent facilities and the truly amazing support staff, many of whom have become great friends. Eric Smith is a walking encyclopedia of low temperature techniques and has never tired of helping me out. I thank Nate Ellis for running a 'free counseling service' for students in distress. Many thanks to Rodney Bowman, Chris Cowulich, Jeff Koski, Stan McFall, and Bob Tillotson at the machine shop for having the motto, 'if you can draw it, we can make it'. Thanks to Linda Hatch and Nick Brown at the stock room and to David Bowman, Leonard Freelove, Bob Kenyon, and Dan Sheerer at Research Services for their patience in dealing with my often strange and demanding requests. Thanks to Dan Blakely and Barry Robison for computer help and to LiLynn Graves for pushing me to take my B Exam for the last two years. I have also benefited from the assistance of Mick Thomas, Steve Kriske, and Jonathan Shu at CCMR.

A special thanks to John Miner at the Physics Office for saving my life on multiple occasions with a TA position as well as taking me to an Ice Hockey game, my first introduction to American college sport. Graduate school would have been very different without the support of and many conversations with Deb Hatfield, Kacey Acquilano, Rosemary French, and Cindee Ball. I have a tendency to get myself into strange and unprecedented administrative tangles and I could not have survived without the wonderful people that make up the LASSP administration. Many thanks to Brenda Irvin-Bryant, Becky Jantz, Tracey Davenport, Keane Leitch, Douglas Milton, Todd Pfeiffer, and Judy Wilson. On April 1, 2011 a flood destroyed all the electronics in my part of the lab. I'm grateful to everyone who helped me get through this difficult time and rebuild the lab. A special thanks to Brenda Irvin-Bryant for all her untiring help in dealing with the aftermath.

I will forever cherish the beauty of Ithaca and the friendliness and character of the Ithaca community that have made my graduate school experience special. My life would

have been very different if I had not had the privilege of being a ‘White House’ resident. If you live at the ‘White House’, ‘life’ comes to you and I’m grateful for crossing paths with all the wonderful and interesting people too many to list individually here. Special thanks go my close friends Watson, Justin Vines, Ben Machta, and Phil Kidd for their continued love, support, entertainment, and valuable life lessons. Being able to continue to live at the ‘White House’ was a major factor in deciding to stay in Ithaca for my postdoc. I would also like to say a huge ‘I Love You’ to the extended ‘White House’ family. A warm thank you to Deeptha Umapathy for her friendship and never ending love of Ithacan Snow.

Many many thanks to Lakshmi Rajaram who grew up with me in India and has shared so many aspects of the ‘American Experience’. I thank my Father (for still being my greatest inspiration), my mother (for her love and youthful energy), and my grandfather (who at 93 still lives life with more gusto than I can muster). And finally I think it is fair to say that I would probably not have been able to see this day without Jennifer Brown, who put her blood, sweat, and tears (her words) into getting me across the finish line and who is a prime example of that rare breed of people - strong, intelligent, sensitive, and caring all at once.

TABLE OF CONTENTS

LIST OF TABLES

LIST OF FIGURES

CHAPTER 1

INTRODUCTION

A supersolid may be defined as a quantum solid a fraction of whose mass is superfluid. The existence of this exotic state of matter was postulated in 1969 and solid ^{4}He was considered a good candidate, but not a hint of experimental evidence was found for more than three decades. In 2004 however, Kim and Chan, in a now famous experiment, claimed to have discovered supersolidity in solid helium. The last eight years have seen a renewal of interest in the field with several experimental and theoretical groups publishing hundreds of papers in an attempt to explain the experimental results. The picture that has emerged is far more complex than what was initially expected and there is mounting evidence that the phenomenon discovered by Kim and Chan might not be due to supersolidiy after all. In the following sections, we review some properties of helium, introduce the idea of supersolidity, describe the Kim and Chan experiment and give a brief overview of the key experiments and theoretical ideas that have been subsequently developed.

1.1 Helium and Superfluidity

Let us begin by looking at the helium atom. The ^{4}He atom, with 2 protons, 2 neutrons, and 2 electrons, is a boson. Figure 1.1 shows the phase diagram of ^{4}He. The boiling point of ^{4}He is 4.21 K and it becomes a superfluid at 2.18 K. Unlike all other liquids, liquid He-4 does not become solid under its own vapor pressure even when cooled to absolute zero. This strange property can be attributed to fact that the binding forces between atoms (Van der Waals forces) are extremely weak due to the closed electronic s-shell. ^{4}He has no static dipole moment and the smallest known atomic polarizibility while its small mass leads to a large quantum mechanical zero-point energy. Since the

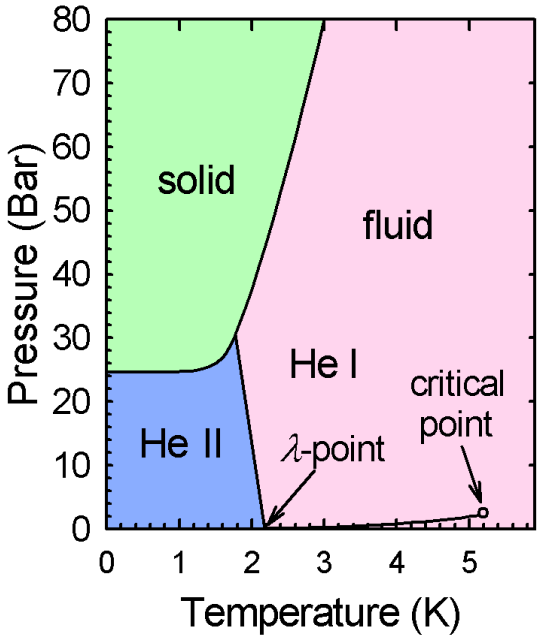

Figure 1.1: The phase diagram of ^{4}He. He I is the normal phase and the He II is the superfluid phase. Notice that ^{4}He does not solidify under its own vapor pressure even if the temperature is lowered to absolute zero. A pressure of $\sim$ 25 bar needs to be applied before solidification can occur. Image adapted from Beamish 2008 (Cornell Physics Colloquium).

zero-point energy is greater than the binding energy, we can think of liquid ^{4}He as a quantum liquid. As can be seen from Figure 1.1, the only way to obtain solid ^{4}He is to apply a pressure of $\sim$ 25 bar.

The most fascinating property of liquid ^{4}He is superfluidity (superfluid phase shown in blue in Figure 1.1). Superfluidity was discovered by Allen, Misener, and Kapitza [1, 42] in 1938. ^{4}He in the superfluid phase can be thought of as a two component fluid, with a normal component and a superfluid component. The superfluid component has zero viscosity, zero entropy, and infinite thermal conductivity. These properties lead to some very strange effects. Figure 1.2 shows three of these effects that can be observed in superfluid ^{4}He.

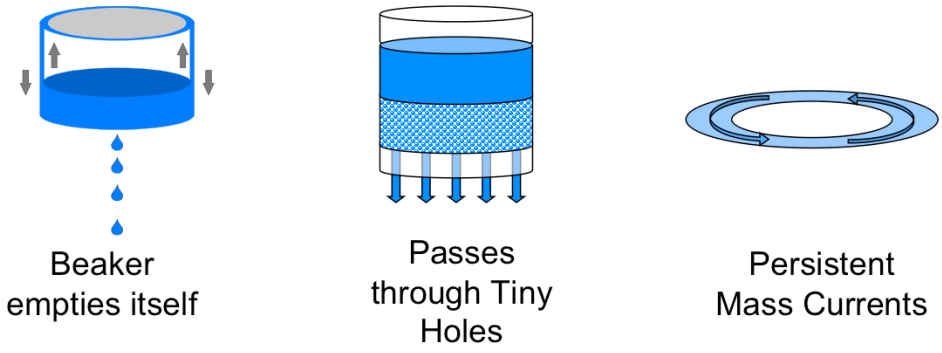

Figure 1.2: Some strange effects that can be observed in superfluid ^{4}He. Adapted from Beamish 2008 (Cornell Physics Colloquium).

1.2 Macroscopic Quantum Phenomena and the Supersolid State

Quantum mechanics is undoubtedly one of the most fascinating aspects of all of physics. The problem with studying quantum phenomena, most of the time however, is that quantum effect are large enough to be directly measurable only when the system size gets extremely small. In most large systems the quantum effects of the constituent atoms and molecules get 'washed out' because the constituent wave functions are out of phase with each other. Is it possible to have a large number of atoms all in phase? Only under very special conditions.

It all began in 1924 when the Indian physicst Satyendra Nath Bose wrote to Albert Einstein describing his ideas on how to treat the electromagnetic waves of the black-body as a gas of identical particles. Einstein immediately saw that Bose was on to someting big and extended Bose's ideas to particles with mass and thus was born Bose-Einstein statistics, the quantum mechanical generalization (for identical particles with integer spin - bosons) of the classical Maxwell-Boltzmann statistics. A profound consequence of Bose-Einstein statistics is the phenomenon of Bose-Einstien Condensation (BEC), which predicts that below a critical temperature, a gas of identical bosons should all (or a macroscopic number of them) settle into the same quantum mechanical ground

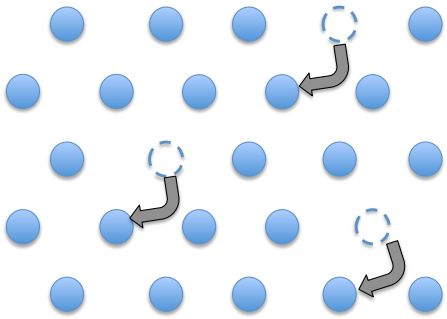

Figure 1.3: The original theoretical proposal for the mechanism by which solid ^{4}He could become a supersolid, which involved the Bose condensation of zero-point vacancies. The zero viscosity motion of this 'vacancy superfluid' would be tantamount to dissipation free mass transport within the solid.

state. This is an example of a macroscopic quantum phenomenon. We now have a situation where the strange and intriguing effects of quantum mechanics can be observed on a macroscopic (large) scale.

Examples of macroscopic quantum phenomena have been discoverd in gases (Bose-Einstein Condensates) [3] and in liquids (superfluidity in liquid ^{4}He). It is natural to ask if such phenomena can occur in solids. In superfluid ^{4}He, a macroscopic number of atoms get into the ground state and can flow with zero viscosity - hence the term 'superfluid'. It is hard to imagine how such resistance-less flow would occur in a solid. In 1969 it was theoretically proposed by Thouless, Andreev, Lifshitz [90, 8] that solid ^{4}He might exhibit supersolidity. Their proposal was based on the existance vacancies in the solid helium-4 lattice even at very low temperatures (called zero-point vacancies). The idea was that these vacancies can themselves Bose condense and form a superfluid. As the vacancies move like a superfluid, this is tantamount to the atoms themselves moving with no resistance. It was thus conceived that there could be a lattice of atoms, but a fraction of which could move around with zero viscosity - a supersolid.

1.3 The Kim and Chan Effect

For more than three decades, searches for the supersolid state proved fruitless [55]. In 2004, however, Kim and Chan at Penn State found the first evidence that solid ^{4}He might display supersolidity. A classical technique for detecting the supefluid transiton uses a torsional oscillator - a container attached to a torsion spring. The frequency of such an oscillator is given by

$$f = \frac{1}{2\pi}\sqrt{\frac{\kappa}{I}} \tag{1.1}$$

where κ is the spring constant and I is the moment of inertia of the oscillator. If the container is filled with liquid helium and the frequency of the oscillator is measured as a function of temperature, one sees an increase in the resonance frequency as the temperature is lowered below the superfluid transition temperature. This is because below the superfluid transition, less and less of the helium is entrained by the wall of the container, thus reducing the effective moment of inertia and increasing the resonance frequency. Can a similar effect be observed if the container is filled with solid instead of liquid ^{4}He? Indeed, as early as 1970, Leggett [48] had noted that a supersolid should show anomalous rotation similar to a superfluid. The Penn State group found just such an increase in the frequency of a torsion oscillator even when it was filled with solid helium. This was interpreted as evidence for the elusive supersolid state.

Figure 1.4A shows the schematic of the Kim and Chan experiment [45]. The body of the oscillator was filled with a porous glass (Vycor) within which was the solid helium. The oscillator was driven and its motion detected using capacitor plates. A lock-in amplifier and a frequency counter measured the resonance frequency of the oscillator. Figure 1.4B shows the results of the experiment. The empty cell background (plus signs) is flat. The superfluid transition for a thin film is shown in open squares. As expected, the period of the oscillator shows a sharp drop at the transition temperature. The surprising

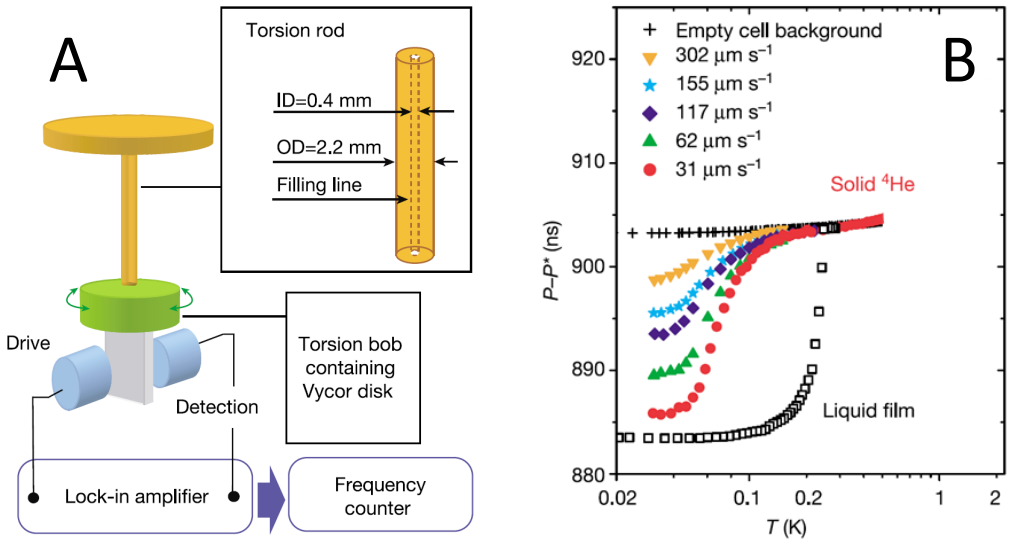

Figure 1.4: The Kim and Chan effect. **(A)** The torsional oscillator along with the detection scheme used in the experiment is shown. The solid helium was contained inside a nanoporous material (Vycor glass) which was itself inside the torsion bob. The torsion rod provided the torsion constant for the oscillator as well as served as the fill line for the helium. **(B)** The period of the oscillator is plotted against temperature. The empty cell background (plus sign) is flat as expected. The transition of a liquid helium film (open squares) is shown for comparison. The surprising finding was the period drop observed when the cell contained solid helium (red filled circles). The 'signal' magnitude decreases with increasing velocity of oscillation. Adapted from [45].

result is when the cell is filled with solid helium. Similar to the superfluid case, a drop in the period is once again observed. Kim and Chan interpreted this drop as a decoupling of a fraction of the mass ($\sim 1\%$) of the solid from the rest of the oscillator. In other words, they interpreted it as evidence for supersolidity. Notice that the the period drop is not sharp like it is for the superfluid case. In addition, the magnitude of the signal decreases with oscillation velocity. This observation was interpreted as a critical velocity of the system.

As we will see shortly, the difference in shape of the period drop for a superfluid and solid was only the first of many dissimilarities. Figure 1.5A shows another phenomenon that is not observed in a bulk superfluid transition. Kim and Chan found that a dissipa-

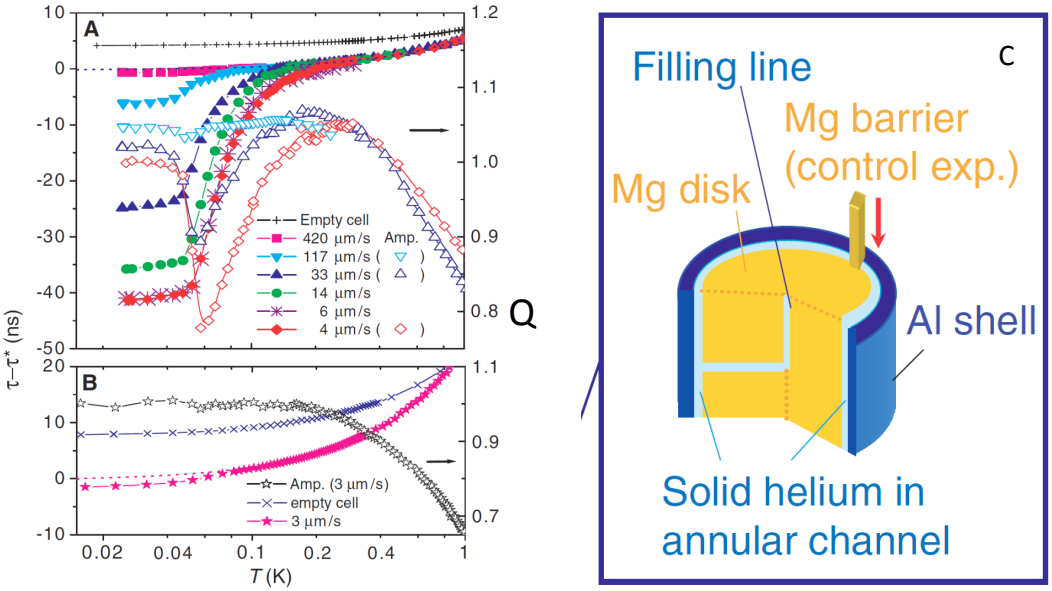

Figure 1.5: **(A)** A dissipation peak always accompanies the period shift. **(B)** The results of the blocked annulus experiment shown in **(C)**. When a barrier is introduced blocking the annulus for solid helium, the signal magnitudes of both the period shift and the dissipation peak are greatly reduced. This result was considered the strongest evidence for supersolidity. Adapted from [44].

tion peak always accompanies the period shift [44]. Moreover, the dissipation peak also shows the magnitude reduction with rim velocity just like the period shift.

Figure 1.5C shows a schematic for the so called blocked annulus experiment, Kim and Chan's first control experiment [44]. They reasoned that if the observed period shift was indeed caused by a fraction of mass being decoupled and not co-rotating with the oscillator, then blocking the circular flow path should force all the mass to rotate and thus eliminate the period shift. When they performed the experiment by blocking the flow path with a barrier in a torsional oscillator with an annular channel, this is exactly what they found (Figure 1.5B). The blocked annulus experiment still remains the most compelling evidence for supersolidity although it has subsequently been argued that there might be non supersolid explanations for these results [40].

1.4 A Selection of Solid ^{4}He Phenomena

Since the discovery of the Kim and Chan effect [45, 44], intense research has subsequently been conducted on this phenomenon and the growing evidence points toward far more complex physics than that of the simple supersolid ideas of the 1970s. In the following sections we present a few of the most salient experimental results that have shaped the thinking in this field.

1.4.1 Effect of ^{3}He Impurities

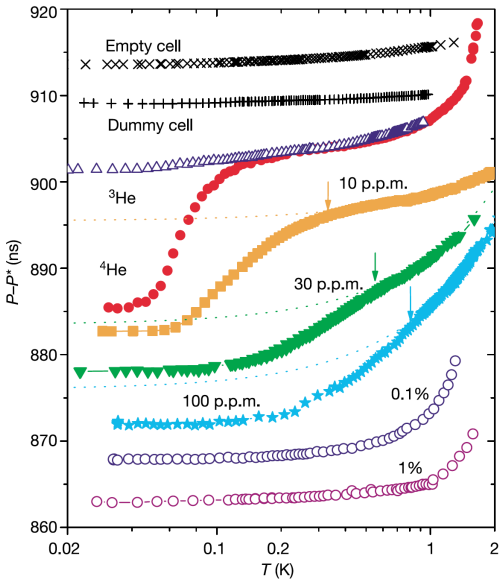

Figure 1.6: The effect of ^{3}He on the Kim and Chan period shift. The empty cell response is flat. The flat response of a dummy cell, with a solid brass block instead of the Vycor disk demonstrates that the effect is not due to the helium in the torsion rod. While the Kim and Chan effect is not observed for pure ^{3}He, the addition of small concentrations of ^{3}He to solid ^{4}He has the effect of increasing the onset temperature of the period shift. Adapted from [45].

One of the first investigations into the nature of the Kim and Chan signal involved looking at the effect of small concentrations of ^{3}He impurities [45]. Commercially available

^{4}He has a nominal ^{3}He concentration of 300 ppb. Figure 1.6 shows first that the Kim and Chan effect is not observed in pure solid ^{3}He. At low concentrations of ^{3}He, the period shift is seen to broaden and shift to higher temperatures as the concentration is increased. It is known that ^{3}He atoms can adsorb and pin dislocations in solid ^{4}He [39, 57]. This has led to the proposal that the Kim and Chan effect can be explained based solely on the dynamics of pinning and unpinning of dislocations within solid ^{4}He [40].

1.4.2 The Importance of Disorder

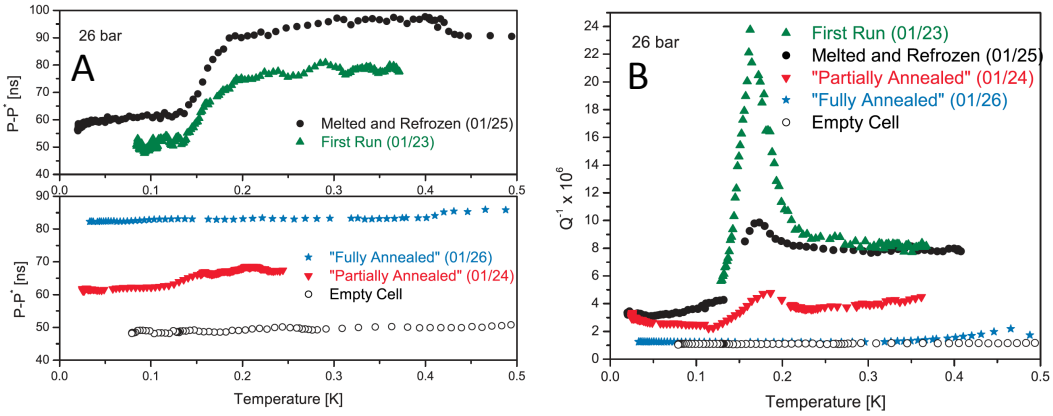

Figure 1.7: The importance of disorder demonstrated by annealing experiments. Both the period shift and dissipation peak disappear or are greatly reduced in annealed samples. The partially annealed sample was maintained between 1.1 and 1.2 K for 5 hours and the fully annealed sample was maintained between 1.4 and 1.5 K for 13 hours before cooling down. Adapted from [74].

Another clue to the mystery of the Kim and Chan effect came from Rittner and Reppy [74] right here at Cornell. They showed that the magnitude of the rotational anomaly can be greatly influenced by how disordered the sample of solid ^{4}He is. They could control the amount of disorder in their samples by the process of annealing, which involves maintaining the solid at a high temperature for extended periods of time to reduce the defect density. Figure 1.7 shows that the magnitude of both the period shift and the

dissipation peak is highest in the most disordered samples and decreasing the disorder (annealing for longer) can almost eliminate the Kim and Chan effect. They also showed that by increasing the disorder by quench freezing samples, rotational anomaly magnitudes corresponding to $\sim 20\%$ mass decoupling could be produced. These results provided strong evidence for the key role that disorder plays even though it was shown that a small rotational anomaly can be found even in the best crystals [22].

1.4.3 Shear Modulus Stiffening

A pivotal development in our story came from the measurements of the shear modulus of low temperature solid ^{4}He in a shear cell by Day and Beamish [28]. They found that as the temperature is lowered in the Kim and Chan regime, the shear modulus μ of solid ^{4}He increases, or the solid becomes stiffer. This was a counterintuitive result since the natural expectation was that if part of the solid was turning into a superfluid, it should somehow now be more like a liquid and thus be easier to shear, not harder. The relevance of this discovery to the recently discovered Kim and Chan effect was underscored by the fact that the temperature dependence of the rotational anomaly and the shear modulus was almost identical. Figure 1.8 shows the exact match between the shear modulus and the rotational anomaly by plotting them on top of each other. Note that the Non-Classical Rotational Inertia or NCRI is a measure of the rotational anomaly and is defined as the percentage of mass that would need to be decoupled to produce the observed period shift. It is a commonly reported quantity in the field although it is not a particularly good one since it presupposes the origin of the Kim and Chan rotational anomaly.

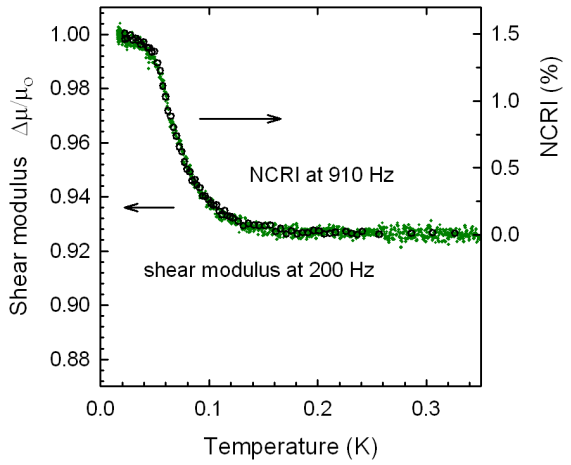

Figure 1.8: Shear modulus stiffening. Soon after the discovery of the Kim and Chan effect, Day and Beamish [28] reported the intriguing result that the shear modulus of solid ^{4}He increases at low temperatures. Furthermore, the temperature dependence of the shear modulus (green diamonds) measured in a shear cell corresponded exactly with the so called NCRI or Kim and Chan signal (black circles) measured in a torsional oscillator. Adapted from Beamish 2008 (Cornell Physics Colloquium).

In addition, Day and Beamish found that the shear modulus increase is also dependent on concentrations of ^{3}He just like the rotational anomaly, further strengthening the connection between the two effects. They proceeded to interpret their results within the framework of the motion of dislocations. The argument is that solid ^{4}He contains mobile dislocations, whose contribution to the response to stress needs to be added to that of lattice deformation. Since these dislocations can be pinned by ^{3}He atoms at low temperatures, one would expect the solid to get stiffer at lower temperatures or higher ^{3}He concentrations. We will discuss this idea more thoroughly in Chapter 4.

1.4.4 Dependence on Measurement Frequency

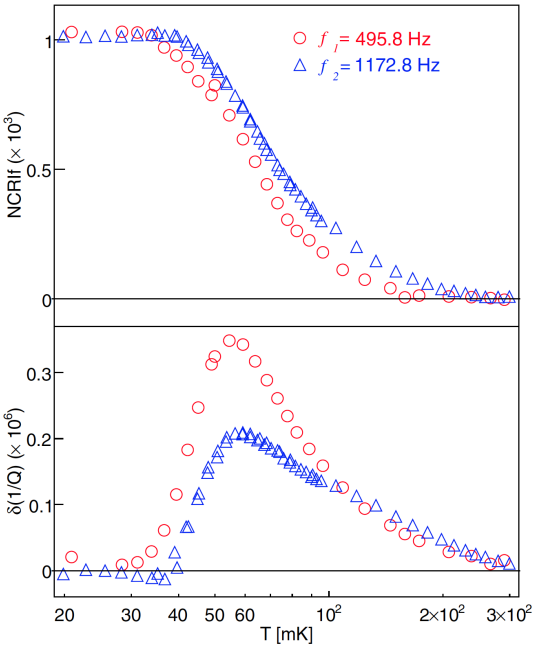

Figure 1.9: Dependence on measurement frequency. By using a double resonance oscillator, Kojima and coworkers [9] showed that both the NCRI and the dissipation peak shifts to higher temperatures at a higher frequency of measurement. Adapted from [9].

The torsional oscillator technique described above, while being exquisitely sensitive to tiny changes in the resonance frequency, has a limitation in that a single oscillator always operates at a single frequency (its resonance frequency). This makes it difficult to study any effects the measurement frequency might have on the rotational anomaly. Although different groups used torsional oscillators with different resonance frequencies, the sensitivity of the Kim and Chan effect to sample preparation history makes it impossible to meaningfully compare these results. To overcome this problem, Aoki *et al.* [9] built a torsional oscillator with two resonance modes (a double resonance oscillator) so that the rotational response of the exact same sample could be measured at two different frequencies. For some ideas on how to construct a variable frequency torsional oscillator, see Appendix D.

Figure 1.9 shows that both the frequency shift and the dissipation peak shift to higher temperatures at a higher frequency of measurement. This is also not an effect that is observed for a superfluid transition.

1.4.5 DC Mass Flow

As discussed in section 1.1, one of the hallmarks of superfluid ^{4}He is its ability to flow through extremely tiny holes. Should a supersolid possess a similar property? Soon after Kim and Chan's claim that solid ^{4}He enters a supersolid state, Day and Beamish attempted to force solid helium thorough an array of fine capillaries [27]. Figure 1.10 shows the setup which consists of two cylindrical chambers separated by a superleak, which was an array of 36000 3 mm long 25 μm diameter holes. The outer wall of the larger chamber was a flexible membrane which could be moved using a piezoelectric actuator. The smaller chamber contained a sensitive capacitive pressure gauge. Day and Beamish found no evidence for low temperature pressure-driven flow and were able to put stringent limits on the flow velocity. The average flow velocity was determined to be less than 1.2×10^{-14} ms^{-1}, 7 orders of magnitude less than the critical velocity inferred by Kim and Chan [45].

Although Day and Beamish did not observe significant flow of solid ^{4}He, it can be argued that applying mechanical pressure on the solid (squeezing the lattice) might not be the best strategy to induce flow. Another idea is to connect two reservoirs of superfluid to each other through the solid and introduce a chemical potential difference between them. If solid ^{4}He is able to provide a path for superflow, helium atoms should go from one reservoir to the other. For our own work using this idea see Chapter 3. Hallock and collaborators [34] used this idea to search for DC mass transport through

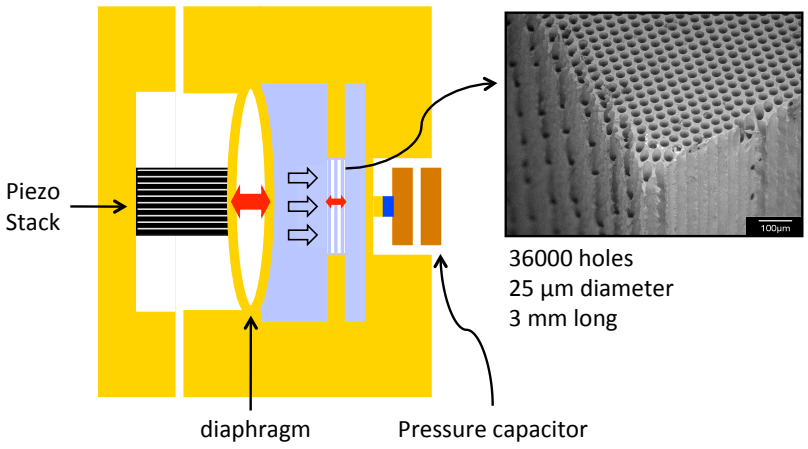

Figure 1.10: Does solid ^{4}He flow through tiny capillaries? Day and Beamish [27] tried to force solid ^{4}He through an array of fine capillaries to see it would flow like a superfluid. They found no evidence for low temperature flow of solid helium (the average flow speed was 7 orders of magnitude smaller than required to explain the Kim and Chan results). Adapted from Beamish 2008 (Cornell Physics Colloquium).

solid ^{4}He. Their apparatus consists of two reservoirs of superfluid ^{4}He connected to each other through nanoporous Vycor rods in series with a sample of solid ^{4}He. They introduce a chemical potential between the two reservoirs either by using the thermomechanical effect or by direct mass injection. All their observations are made off but near the melting curve. Their principal results are that no DC flux of atoms was observed above 650 mK while an increasing flux was seen as the temperature was lowered below 650 mK, with a flux minimum between 75-80 mK. They have interpreted these observations as being caused by a Bosonic Luttinger liquid. While the result of Hallock *et al.* [34] are extremely interesting, their connection to the Kim and Chan effect is not yet elucidated.

1.5 Theoretical Interpretations

The original proposal in 1969 by Thouless, Andreev, and Lifshitz [90, 8] for the mechanism of supersolidity involved the Bose-Einstein condensation of zero-point vacancies in solid ^{4}He. Such a vacancy condensate should display frictionless transport, which, since a vacancy is a lack of an atom, would be equivalent to dissipation less mass transport. Soon afterward, in 1970, Leggett [48] pointed out that such a supersolid should exhibit anomalous rotational properties similar to a superfluid. The first obvious question that needed to be answered after the 2004 discovery of the Kim and Chan effect [45, 44] was whether this effect was a manifestation of vacancy condensation.

The first part of this question concerns the existence of vacancies in the ground state of solid ^{4}He at $T = 0$ K. What conditions would favor vacancies at the lowest temperatures? It can be argued that removal of an atom will result in a potential energy cost (since there would now be fewer bonds) but it could lead to a kinetic energy gain (if the vacancy is delocalized). From the point of view of energy minimization, therefore, if the gain is greater than the cost, we say that the balance is negative and we should expect zero-point vacancies. Monte Carlo simulations [65, 16, 19] have now shown however, that the energy balance is positive and large. It requires energies corresponding 10 K to create vacancies. These results indicate that it is unlikely that the rotational anomaly observed at ~ 0.1 K is due to vacancy-induced supersolidity.

Although the Monte Carlo results argue that supersolidity cannot exist in perfect crystals of solid ^{4}He [65, 19], they do not rule out mechanisms of disorder-induced supersolidity. Some theories suggest that dislocations [17] in single crystals and grain boundaries [62] in polycrystals can support superfluid within them and thus in a three dimensional connected defect network, one could observe mass decoupling and supersolid

behavior. It should be noted, however, that there not universal agreement that disorder is essential for supersolidity. Anderson has proposed that the Kim and Chan effect [45, 44] is due to vortex liquid model [4, 5, 6] in which, while disorder can enhance the effect, it is not necessary in the first place.

Not all models constructed to explain the Kim and Chan effect are supersolid models. There have been numerous attempts to explain the observed phenomena without invoking any superfluidity. The observations of Day and Beamish [28] that the shear modulus mimics the rotational anomaly and furthermore that it shows a similar dependence on ^{3}He concentration drew attention to dislocations. Since it is known that dislocation motion can be frozen out with lowering temperature and pinned with increasing ^{3}He concentration [39, 57], dislocation motion has emerged as an important idea to explain Kim and Chan's and other observations [28, 88, 77, 40, 81, 83, 84]. For a more detailed discussion of dislocation motion, see Chapter 4. There are also non-superfluid models in which the population of inertially active crystal excitations are proposed to be atomic-scale tunneling two-level systems [7, 47, 82], or the glassy response of defects distributed throughout the solid [11, 56, 32].

1.6 Is Solid ^{4}He a Supersolid?

It is clear from the experimental evidence and the theoretical effort that the Kim and Chan effect [45, 44] is not a direct manifestation of solid ^{4}He entering a classic supersolid state as envisioned by Thouless, Andreev, and Lifshitz [90, 8]. Whether the underlying physics is of some kind of exotic supersolid or we will eventually explain all the observations with purely non-superfluid models is still not entirely clear. The following chapters present a few clues to the puzzle.

CHAPTER 2

GENERALIZED ROTATIONAL SUSCEPTIBILITY STUDIES

Using[12] a novel SQUID-based torsional oscillator (TO) technique to achieve increased sensitivity and dynamic range, we studied TOs containing solid ^{4}He. Below ~250 mK, the TO resonance frequency f increases and its dissipation D passes through a maximum as first reported by Kim and Chan. To achieve unbiased analysis of such ^{4}He rotational dynamics, we implemented a new approach based upon the generalized rotational susceptibility $\chi^{-1}_{^4He}(\omega, T)$. Upon cooling, we found that equilibration times within $f(T)$ and $D(T)$ exhibit a complex synchronized ultraslow evolution toward equilibrium indicative of glassy freezing of crystal disorder conformations which strongly influence the rotational dynamics. We explored a more specific $\chi^{-1}_{^4He}(\omega, \tau(T))$ with $\tau(T)$ representing a relaxation rate for inertially active microscopic excitations. In such models, the characteristic temperature T^* at which df/dT and D pass simultaneously through a maximum occurs when the TO angular frequency ω and the relaxation rate are matched: $\omega\tau(T^*) = 1$. Then, by introducing the free inertial decay (FID) technique to solid ^{4}He TO studies, we carried out a comprehensive map of $f(T, V)$ and $D(T, V)$ where V is the maximum TO rim velocity. These data indicated that the same microscopic excitations controlling the TO motions are generated independently by thermal and mechanical stimulation of the crystal. Moreover, a measure for their relaxation times $\tau(T, V)$ diverges smoothly everywhere without exhibiting a critical temperature or velocity, as expected in $\omega\tau = 1$ models. Finally, following the observations of Day and Beamish, we showed that the combined temperature-velocity dependence of the TO response is indistinguishable from the combined temperature-strain dependence of the ^{4}He shear modulus. Together, these observations imply that ultra-slow equilibration of crystal disorder

[1]The work described in this chapter was done in collaboration with E. J. Pratt, B. Hunt, M. Yamashita, M. J. Graf, A. V. Balatsky, and J. C. Davis.

[2]The presentation of this chapter closely follows that first put forward in Gadagkar *et al.* [31].

conformations controls the rotational dynamics and, for any given disorder conformation, the anomalous rotational responses of solid ^{4}He are associated with generation of the same microscopic excitations as those produced by direct shear strain.

2.1 Introduction

Solid ^{4}He is a bosonic crystalline material that is a candidate to become a supersolid at low temperature [90, 8, 70, 20, 48, 55, 12]. Studies using high-Q torsional oscillators (TO) containing solid ^{4}He [45, 44, 74, 9, 59, 46, 37, 64, 21, 76] have revealed that the TO resonant angular frequency of rotation ω increases rapidly below both ~250 mK and maximum TO rim-velocity $V \sim 10^{-4}$ ms^{-1}, perhaps as if superfluid inertia becomes decoupled from the container below a critical [91] temperature T_c and velocity V_c. Moreover, these TO resonant frequency increases [45, 44, 74, 9, 59, 46, 37, 64, 21] are reported to be greatly diminished by blocking the TO annulus [44, 76], as if due to reconnection of that inertia. Features in the specific heat capacity ascribed to a supersolid phase transition [50, 51] or disorder-induced dynamic crossover [82] also occur in this same temperature range.

Nevertheless the phenomenology of this solid also contains many unexpected effects. In DC mass-flow studies, the maximum mass-current densities are several orders of magnitude smaller than those implied by the TO experiments [27, 79, 67, 68, 69, 66] and are observed at temperatures far higher than those characteristic of the Kim and Chan effects [79, 67, 68, 69]. Experiments in which the ^{4}He solid is annealed near the melting temperature with the objective of diminishing any crystal disorder have also shown that the maxima in df/dT and D can be greatly reduced within the same sample [74, 79, 75, 22, 23, 78]. Moreover, the temperature dependence of the resonance frequency $f(T)$ of TOs containing solid ^{4}He [45, 44, 74, 9, 59, 46, 37, 64, 21] is also very similar to that

of its shear modulus $\mu(T)$ [28] and, coincident with the maximum rates of increase of $f(T)$ and $\mu(T)$ are unexplained maxima in TO dissipation [44, 74, 9, 46, 37] and shear-dissipation [28, 88], respectively. Finally, the increased values of both f and μ at lowest temperatures are extinguished by increasing TO maximum rim velocity [45, 44, 74, 9, 59, 46, 21] or shear strain ε [28, 29], respectively. A simple transition to a supersolid appears, at present, to be inconsistent with all these phenomena.

A number of different classes of theoretical models have been proposed to explain the complex rotational dynamics observed for solid ^{4}He. The first is a basic supersolid in which Bose-Einstein condensation of vacancies produces a superfluid component interpenetrating the crystal [90, 8, 70, 20, 48, 55, 12]. The second class describes an incipient supersolid lacking long range quantum phase coherence [4, 60]. A third class of model is that nanoscale heterogeneous superfluidity can be generated by specific types of crystalline disorder [37, 80, 17, 93, 18, 14, 87, 89]. Finally, there are also non-superfluid models in which solid ^{4}He contains a population of inertially active crystal excitations [77, 11, 56, 32, 7, 40] whose relaxation time τ lengthens smoothly with falling T. These excitations are proposed variously to be a dynamical network of pinned dislocations [28, 88, 77, 40, 81, 83, 84] atomic-scale tunneling two-level systems [7, 47, 82], or the glassy response of defects distributed throughout the solid [11, 56, 32]. All inertially active excitation models have the property that, as $\tau(T)$ passes through the condition $\omega\tau = 1$, a strong maximum in $|df/dT|$ and D should occur [37, 64, 11, 56, 32, 7, 40] even though there is no supersolid T_c and V_c.

2.2 Generalized Rotational Susceptibility: The Framework

An unbiased approach to TO studies of solid ^{4}He can be achieved by using the TO rotational susceptibility $\chi(\omega, T) = \theta(\omega, T)/\Gamma(\omega)$ [11, 56, 32]. Here $\theta(\omega, T)$ represents the amplitude of angular displacement as a function of ω and T in response to a constant magnitude harmonic torque $\Gamma(\omega)$. It can be shown that [11, 56, 32]

$$\chi^{-1}(\omega, T) = K - I\omega^2 - i\gamma\omega - \chi^{-1}_{^4He}(\omega, T) \tag{2.1}$$

describes the properties of the bare TO plus the back action of the solid ^{4}He through its complex rotational susceptibility $\chi^{-1}(\omega, T) = \Re(\chi^{-1}_{^4He}) + i\Im(\chi^{-1}_{^4He})$ [56]. I is the combined moment of inertia of the TO plus ^{4}He at zero-temperature, K is the torsional spring constant, and γ is the TO damping constant (see Figure 2.1).

These concepts can be made concrete by considering, for example, a classic (Debye) form for the rotational susceptibility [11, 56, 32] that describes the freeze-out of an ensemble of excitations whose relaxational time-constant $\tau(T)$ increases with decreasing T

$$\chi^{-1}_{^4He}(T) = \frac{g}{1 - i\omega_0\tau(T)} \tag{2.2}$$

(for a discussion of the Debye form with a distribution of activation energies, see Ref. [88]). For solid ^{4}He, g/ω_0^2 would then represent the rotational inertia associated with the relevant excitations, and the components of inertial and dissipative back action on the TO at resonance ω_0 are given respectively by

$$\Re[\chi^{-1}_{^4He}(T)] = \frac{g}{1 + \omega_0^2\tau^2} \tag{2.3a}$$

$$\Im[\chi^{-1}_{^4He}(T)] = \frac{g\omega_0\tau}{1 + \omega_0^2\tau^2} \tag{2.3b}$$

As is always the case with such $\omega\tau = 1$ models, when $\Re(\chi^{-1}_{^4He})$ changes due to the $\tau(T)$ term, then $\Im(\chi^{-1}_{^4He})$ must always change in a quantitatively related fashion. Such changes

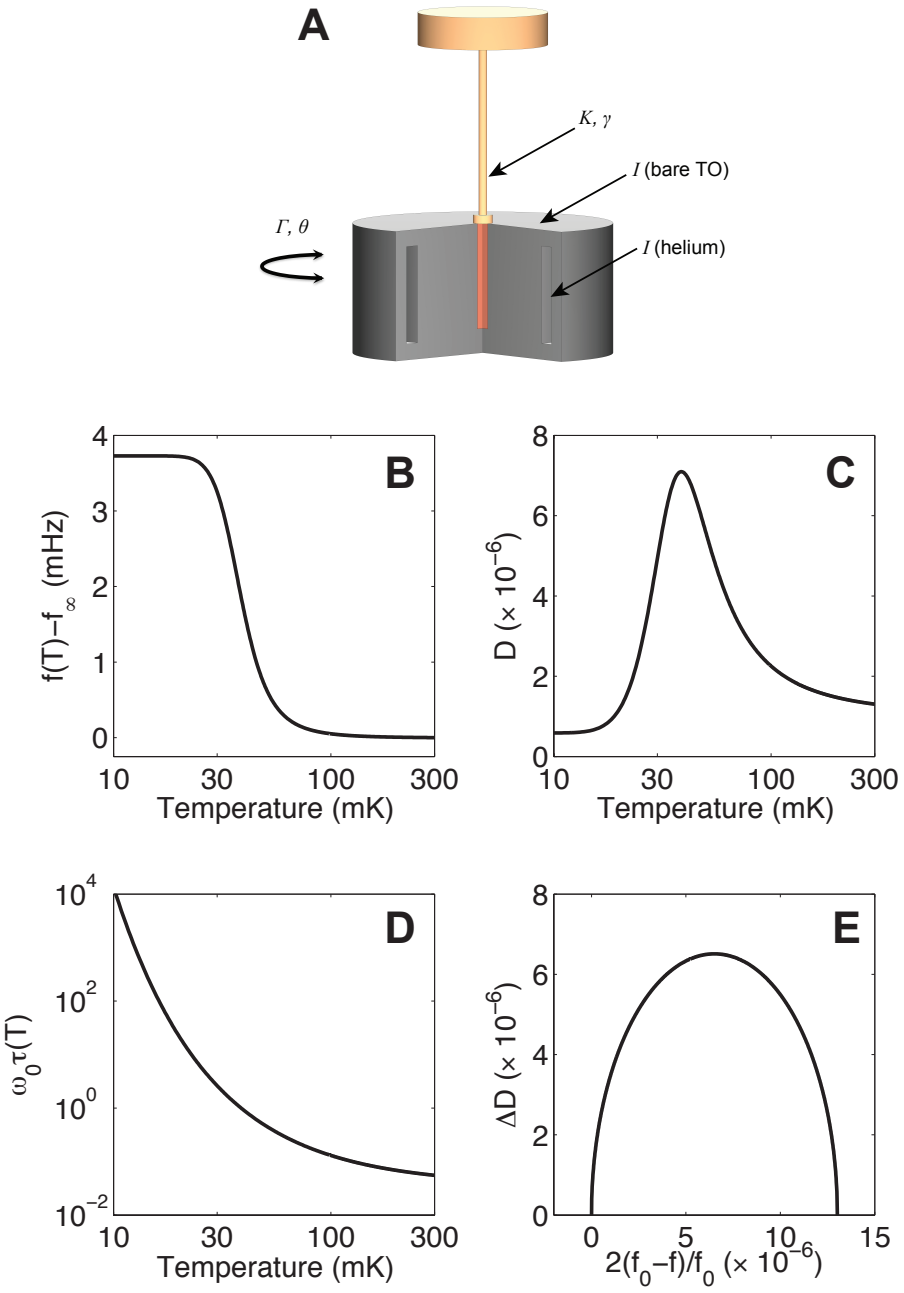

Figure 2.1: The generalized rotational susceptibility approach to studying torsional oscillator dynamics. **(A)** Schematic of a torsional oscillator containing solid ^{4}He with the various parameters appearing in Equation 2.1 of the main text. The **(B)** frequency shift predicted by the Debye susceptibility (Equation 2.4a) for **(C)** dissipation (Equation 2.4b) obtained by fitting to data. The ratio of the imaginary to the real part of the Debye susceptibility yields the **(D)** relaxation time (Equation 2.5). The **(E)** Davidson-Cole plot of the Debye susceptibility (Equation 2.6) is a semicircle.

would be measurable because (see Figure 2.1 B and C), for a high-Q TO containing solid ^{4}He governed by Equation 2.2

$$\frac{2(f_0 - f(T))}{f_0} = \frac{1}{I\omega_0^2}\Re[\chi^{-1}_{^4He}(T)] \tag{2.4a}$$

$$D(T) - D_\infty = \frac{1}{I\omega_0^2}\Im[\chi^{-1}_{^4He}(T)] \tag{2.4b}$$

where f_0 is the frequency at lowest temperature and D_∞ is the dissipation far above T^*, and $D(T) = Q^{-1}(T) - Q^{-1}(T \to \infty)$ is the inverse contribution to the TO quality factor Q from the solid ^{4}He [11, 56, 32]. Moreover for the susceptibility of Equation 2.2

$$\frac{\Im(\chi^{-1}_{^4He})}{\Re(\chi^{-1}_{^4He})} = \frac{D(T)f(0)}{2(f(0) - f(T))} = \omega_0\tau(T) \tag{2.5}$$

(see Figure 2.1 D) so that access to $\tau(T)$ of the microscopic excitations is therefore possible, at least in principle, from measurements of $\Re(\chi^{-1}_{^4He})$ and $\Im(\chi^{-1}_{^4He})$.

A well defined characteristic temperature T^* for any such susceptibility occurs when $\omega_0\tau(T^*) = 1$. Both the $f(T)$ slope and the dissipation $D(T)$ of a physically plausible susceptibility achieve their respective maxima when the temperature is very close to T^*. Figure 2.1 B and C are examples of this, using Equation 2.3, the susceptibility in Equation 2.2 and the $\tau(T)$ in Figure 2.1 D. This T^* is a very different concept to that of a critical temperature, since it is not related to a thermodynamic phase transition but is, instead, the temperature at which a probe frequency and the microscopic relaxation rate are matched: $\omega_0\tau(T^*) = 1$.

A common tool to illuminate the relationship between the real and imaginary components of such a susceptibility is a direct plot of $\Im(\chi)$ vs. $\Re(\chi)$ in the complex plane [25, 26]. When used in the context of the dielectric susceptibility ϵ of classical glasses or polarized liquids, this is called a Cole-Cole or Davidson-Cole (D-C) plot [25, 26] where it is the locus of points $(\Re[\epsilon], \Im[\epsilon])$ which is plotted with the implicit control parameter being typically the measurement frequency ω. In high-Q TO experiments,

by contrast, the measurement frequency is fixed at the resonant frequency and the response of the system is varied by changing T . The analogous plot would then be the locus of points $(\Re[\chi^{-1}], \Im[\chi^{-1}])$, and it should reveal characteristics of the underlying physical mechanism; e.g. deviations from the Debye susceptibility appear as prominent geometric features in the D-C plot. In the case of the rotational susceptibility of the TO-helium system, the D-C plot also eliminates the need for specific models of the relaxation time $\tau(T)$. Specifically, the susceptibility, $\chi^{-1}_{^4He}(\omega, T) = g/(1 - i\omega_0\tau(T))$, generates a semicircle (see Figure 2.1 E) centered on $X = \Re[\chi^{-1}_{^4He}] = g_0/2$ with radius $g_0/2$, as can be seen by eliminating $\omega_0\tau$ from Equation 2.3a and 2.3b. One finds that $(X - g_0/2)^2 + Y^2 = (g_0/2)^2$, where $Y = \Im[\chi^{-1}_{^4He}]$. The natural abscissa and ordinate for a Davidson-Cole plot for TO studies are:

$$\Delta D \quad \text{versus} \quad \frac{2\Delta f}{f_0} \tag{2.6}$$

where $\Delta D = D(T) - D_\infty$ and $\Delta f = f_0 - f(T)$.

2.3 Squid-Based High-Resolution Torsional Oscillator

Our main development in solid helium TO techniques was the introduction of a superconducting quantum interference device (SQUID)-based displacement sensor. Such sensors have been used to study aspects of superfluid helium too sensitive to be otherwise detected, such as phase slippage and the Josephson effect in ^{3}He and ^{4}He [61, 35], and were originally invented for gravity wave detectors. In our experiments, we detect the motion of a high-field permanent samarium cobalt (SmCo) magnet attached to the bottom of the TO (see inset to Figure 2.2 A) by sensing the change in magnetic flux through a nearby stationary pickup coil. The pickup coil is in series with an input coil inductively coupled to the loop of a DC-SQUID; the two coils and the wire connecting

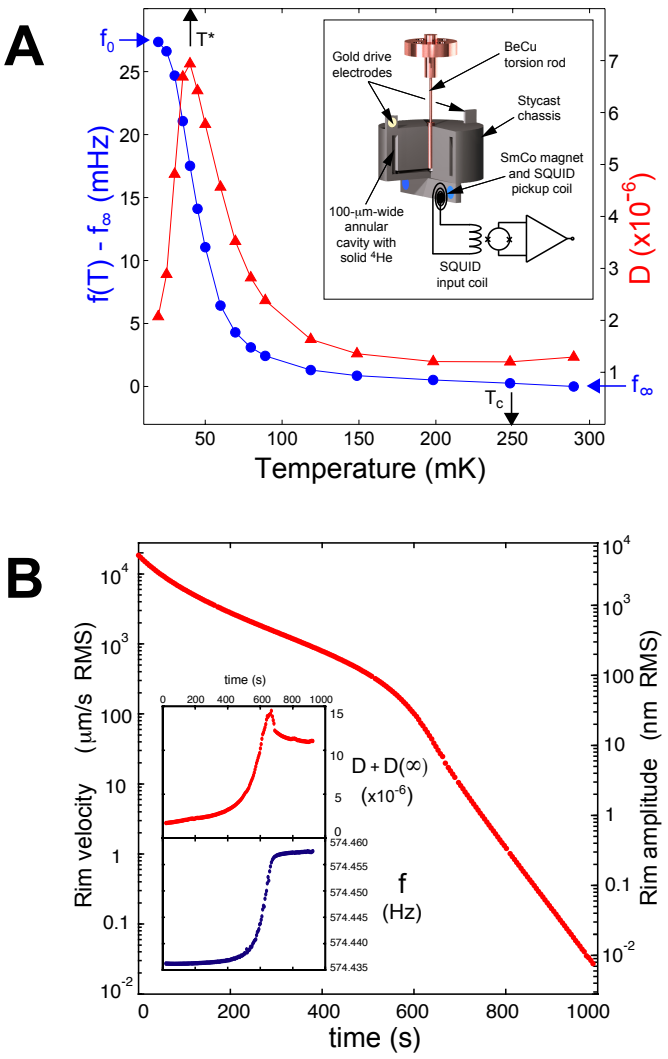

Figure 2.2: **(A)** The resonant frequency shift $f(T) - f_\infty$ (blue circles) and dissipation $D(T)$ (red triangles) for our TO-solid ^{4}He system. Indicated with black arrows are T^*, the temperature at which $D(T)$ peaks and the slope of $f(T) - f_\infty$ is maximal, and T_c, the temperature at which a change in $f(T) - f_\infty$ becomes detectable above the noise. **(Inset to A)** A schematic of the SQUID-based torsional oscillator (TO). Applying an AC voltage to the drive electrodes rotates the Stycast chassis (containing the solid ^{4}He in a 100 μm-wide annular cavity of radius 4.5 mm) about the axis of the BeCu torsion rod. The angular displacement of a SmCo magnet mounted on the TO generates a change in the magnetic flux through the stationary pickup and input coils of a DC-SQUID circuit and thereby a voltage proportional to displacement. **(B)** A typical Free-Inertial Decay (FID), taken at 47 mK. This was acquired by stabilizing the temperature, driving the oscillator to high amplitude, and then suddenly turning off the AC drive. **(Inset to B)** The corresponding frequency and dissipation as a function of time during the FID.

them form a superconducting loop. When a moving magnet attached to the TO changes the magnetic flux through the pickup coil, a current is generated in the superconducting loop and therefore in the input coil as well. The resultant magnetic flux is detected by the DC-SQUID. The DC-SQUID is operated in a flux-locked loop [24] and therefore generates an output voltage V_{sq} proportional to the change in flux $\Delta\varphi_{sq}$ in the SQUID loop.

The type of SQUID-based sensor used in the earlier studies noted above also used a superconducting circuit to couple flux changes generated by a moving element into a DC-SQUID loop, but the moving element was not a permanent magnet. In that case, the moving element was a superconducting plane that modified the inductance L of a nearby pickup coil in a (primary) superconducting loop containing a persistent current I. Since $\Delta\Phi = 0$ in a superconducting loop, a change in the inductance due to the moving superconducting plane generated a change in the persistent current $I_1 \rightarrow I_1 + \delta I_1$, which could be coupled (via a secondary superconducting loop and a secondary persistent current I_2) into the DC-SQUID. For more details about this detection scheme, see [58]. Our novel permanent magnet method has several advantages over the older method. These are related primarily to the simplicity of our circuit. First, the probability of success of either detection scheme is related to the number of superconducting (SC) joints that need to be made between the various superconducting elements in the two circuits. Our new scheme has 6, whereas the older scheme has 9, including two 3-way SC joints. Additionally, the SC joints determine the critical current of the primary superconducting loop I_c and therefore the maximum persistent current $I_{max} = I_c$ that can be injected into the loop. Since the displacement responsivity η of the circuit is directly proportional to the injected current, the responsivity of the displacement sensor can be severely limited by a single low critical current joint. The permanent magnet-scheme is much more reliable in this regard with no loss in responsivity. Second, the

injection of the persistent current can be a delicate matter, involving decoupling of the 4 K superconducting circuit and the 300 K current-injection source via a long retractable conduit; the permanent magnet scheme is free of such complications. The DC-SQUID[3] we used has limiting flux sensitivity of ~5 $\mu\varphi_0/\sqrt{\text{Hz}}$. The output voltage of the DC-SQUID is proportional to the displacement δx of the magnet, with the proportionality constant called the responsivity η_{sq}: $V_{sq} = \eta_{sq}\delta x$. The responsivity is a function of both the DC-SQUID circuitry and also the particulars of the coupling between the magnet and the pickup coil. For the highest gain settings of the DC-SQUID feedback loop, typical values are $\eta_{sq} = 1$ V/nm and a displacement noise sensitivity δx_{min} (corresponding to the flux noise quoted above) below 10^{-15} m/$\sqrt{\text{Hz}}$. Such responsivity is so high that, for some purposes, we often had to decrease it by moving the coil away from the magnet.

Our solid ^{4}He samples were grown from a high-pressure liquid (at 73 bar and 3.3 K) with a nominal ^{3}He concentration of 300 ppb by the blocked capillary method, cooling rapidly along the melting curve (approximately 100 minutes from 3.2 K to < 1 K). Samples typically reach a low-temperature pressure of 39 bar. The samples are formed inside an annular chamber with a cross-section of 100 microns × 3 mm and radius of 4.5 mm (see inset to Figure 2.2 A). The torsion rod is made of annealed beryllium copper and the helium sample chambers are made of Stycast 1266 for low inertia. For most of the studies reported here, the resonant frequency at 300 mK is 575.018 Hz for the empty cell and 574.433 Hz for the full cell. The full-cell Q at 300 mK is 4×10^5. The torsional motion was detected either by a capacitor electrode (used at highest velocities) or via the DC-SQUID based position detector.

Using a TO containing solid ^{4}He (Figure 2.2 A inset) we then measure $f(T)$ and $D(T)$ effects in good agreement with other research groups [45, 44, 74, 9, 59, 46]. Figure 2.2A shows the evolution of $f(T)$ (blue circles) and $D(T)$ (red triangles) for our

[3]Quantum Design, Model 550

typical sample; the change in $f(T)$ between 300 mK and 10 mK would represent a supersolid fraction of 4.8% if the frequency shift were ascribable to a superfluid decoupling. Our samples, while formed by the blocked capillary procedure and therefore amorphous[4], are of the type most widely studied in the field [45, 44, 74, 9, 59, 46].

2.4 Ultra-Slow Equilibration

To examine the sample equilibration characteristics of solid ^{4}He, we performed the experiment outlined in [37]. The temperature is decreased stepwise from an initial temperature T_i to a final equilibrium temperature T_{eq}, and the rapid co-evolution of $f(T)$ and $D(T)$ are observed as the thermometers approach T_{eq}. More importantly, the subsequent changes after the thermometers equilibrate, $f(t, T_{eq})$ and $D(t, T_{eq})$, are measured. While for the initial $t < t_{eq}$ part of each trace both $f(T)$ and $D(T)$ change rapidly with temperature, their slopes change sharply at t_{eq} indicating that the solid inside the TO maintains thermal equilibrium with the mixing chamber. Above $T^* \sim 65$ mK which is identified as the point of maximum rate of increase of $f(T)$and of the peak in $D(T)$, these equilibration rates are independent of temperature and less than 100 s. But below this temperature both equilibration rates begin to increase rapidly on indistinguishable trajectories, indicating that the ultra-slow equilibration processes in f and D are intimately linked. Such ultra-slow equilibration processes for solid ^{4}He have also been reported in other studies [9, 23, 10, 33, 52, 60].

We examine the relationship between the equilibration of dissipation and the frequency shift - as both approach their long-time equilibrium states. In the relevant experiment, the ^{4}He sample is cooled to 17 mK and then equilibrated for a time > 20,000

[4]The word 'amorphous' (meant to include polycrystalline) is here used to distinguish these samples from single crystals

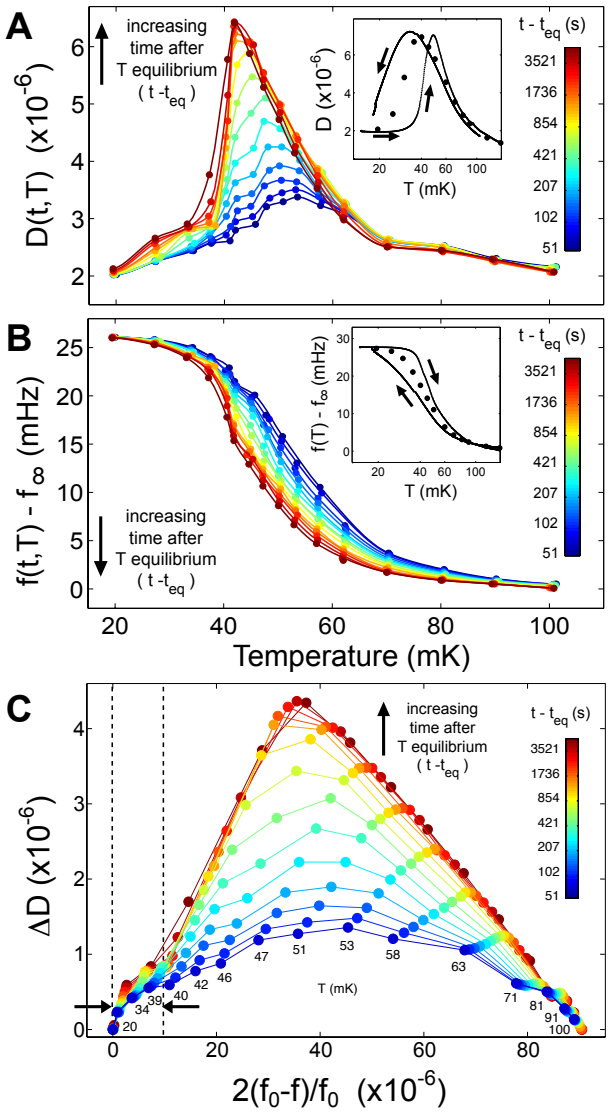

Figure 2.3: Measured time evolution of **(A)** $D(t,T)$ and **(B)** $f(t,T)$ for the abrupt warming experiment described in the text and in [37]. The data are colored circles and the lines are smooth interpolations, intended as guides to the eye. The dark blue lines represent $D(t,T)$ and $f(t,T)$ at $t \sim 50$ s while the dark red lines represent $D(t,T)$ and $f(t,T)$ at ~ 5000 s. **(Insets)** Thermal hysteresis in the dynamical response as shown by the black curves in $D(T)$ **(Inset to A)** and in $f(T)$ **(Inset to B)**, with the direction of the temperature change indicated by black arrows. The data indicated by circles were acquired after waiting $t \gg 5{\times}10^3$ seconds at each temperature as the dynamical response (of Figure 2.3 A and B) asymptotically approached the infinite-time limit. **(C)** Time-dependent Davidson-Cole plot. This is a parametric plot of the data shown in Figure 2.3 A and B the real and imaginary parts of χ (see Equation 2.3) removing the explicit dependence on temperature. The vertical dashed lines indicate the maximum value of $2(f_0 - f)/f_0$ that would be predicted by the Debye susceptibility (Equation 2.2), given the peak height of ΔD.

s to achieve an unchanging state. It is then heated abruptly to a temperature T and the subsequent equilibration in both $f(t,T)$ and $D(t,T)$ are monitored. The resulting time dependence of dissipation $D(t,T)$ is shown in Figure 2.3 A. At short times after temperature stabilization, the dissipation increases slightly (dark blue in Figure 2.3 A). But these dissipative processes are actually very far out of equilibrium. As time passes, the dissipation slowly increases on a trajectory indicated by the transition from the blue line representing $D(t,T)$ at $t \sim 50$ s to the dark red line representing $D(t,T)$ at ~ 5000 s. In the same experiment, the time dependence of $f(t,T)$ is also measured (Figure 2.3 B). It differs from that of $D(t,T)$; at shortest times after stabilization at T the frequency has already changed greatly from its lowest temperature value (Figure 2.3 B). This means that much of the frequency change responds immediately to the mixing chamber temperature change (and therefore also that rapid thermal equilibrium always exists between the sample and the mixing chamber thermometer (for a detailed discussion of the relevant thermal and mechanical time constants, see section 2 of the supplementary online materials of Ref. [37]). The subsequent equilibration of the remaining component of the frequency shift exhibits an ultra-slow reduction in f as indicated by the transition from the blue line at $t \sim 50$ s to the dark red line representing $t \sim 5000$ s in Figure 2.3 B.

These data illustrate how the slowing equilibration dynamics within $D(t,T)$ and $f(t,T)$ are synchronized in such samples of solid ^{4}He. They also imply that thermal hysteresis should occur when temperatures are swept faster than the relevant equilibration times in Figure 2.3 A and B. In the insets to Figure 2.3 A and B swept-temperature measurements on the same sample show that thermal hysteresis occurs in both $D(T)$ (inset to Figure 2.3 A) and $f(T)$ (inset to Figure 2.3 B), with their long-time equilibrium values (solid circles) falling within the hysteresis loops, as expected. Such ultra-slow hysteresis effects are also observed in many other solid ^{4}He TO studies [9, 60].

Equation 2.4b can be fit to the measured $D(T)$. Comparison of the resulting prediction from Equation 2.4a for $f(T)$ to the measured $f(T)$ shows that a Debye susceptibility is inconsistent with the relationship between D(T) and $f(T)$ [37]. Nevertheless, as the equilibration processes of $D(t,T)$ and $f(t,T)$ are synchronized (Figure 2.3 A and B), there must be an intimate relationship between $\Re(\chi^{-1}_{^4He})$ and $\Im(\chi^{-1}_{^4He})$. To study this relationship following Equation 2.6, we make a Davidson-Cole plot of $D(T) - D_\infty$ versus $2(f_0 - f(T))/f_0$ in Figure 2.3 C. It reveals that, instantaneously upon warming, the D-C plot is a symmetric elliptical curve, whereas after several thousand seconds the response has evolved into a skewed D-C curve. But the maximum frequency shift expected from the maximum observed dissipation within the Debye susceptibility (vertical dashed lines) is again far too small. Moreover, no temperature equilibration lag between the solid ^{4}He sample and the mixing chamber could generate the complex dynamics reported in Figure 2.3 because, for any given frequency shift f, a wide variety of different dissipations D are observed [37].

2.5 The Free Inertial Decay Technique

With sufficiently high signal-to-noise ratio and dynamic range, a TO free inertial decay (FID) during which oscillations of large initial amplitude (and maximum rim-velocity V) are allowed to decay freely in time during which $f(V)$ and the dissipation rate $D(V)$ are measured continuously allows complete mapping of the dynamics in the $V-T$ parameter space. We introduced this FID approach to TO studies of solid ^{4}He [64]. High precision sensing of rotational motions is achieved primarily using the DC-SQUID-based detection (inset to Figure 2.2 A) of the magnetic flux from a permanent magnet attached to the TO body. From a typical FID (Figure 2.2 B) at a single temperature T, $f(T,V)$ is measured by using a high-precision frequency counter, and $D(T,V)$ is determined by the

measured rate of energy loss from the TO. The experimental procedure[5] then consists of such measurements over many orders of magnitude in V during each FID, at a closely spaced sequence of different temperatures T. Following this approach, the first complete map of rotational susceptibility of a TO containing solid ^{4}He throughout the $V-T$ plane was achieved. The results in Figure 2.4 A and B show that the frequency increase and dissipation peak are bounded by closely corresponding $V-T$ contours. This means that the same dissipation peak seen with falling temperature near the proposed supersolid T_c is found also with diminishing V in the range of the proposed [45, 44] supersolid V_c. The highly similar contours of both $f(T,V)$ and $D(T,V)$ also reveal that the maxima in $|df/dT|$ and D are always linked - as if controlled by some combined function of T and V. Similar results were obtained in three distinct samples.

2.6 Analysis of Rotational Susceptibility Throughout the Velocity-Temperature Plane

To explore the relationship between thermal and mechanical stimulation of the solid ^{4}He sample revealed by $f(T,V)$ and $D(T,V)$, we compare the rotational dynamics versus T as $V \rightarrow 0$ to those versus $V^{0.5}$ as $T \rightarrow 0$. Figure 2.5 A and C show $f(T)|_{V\rightarrow 0}$ and $D(T)|_{V\rightarrow 0}$ while Figure 2.5 B and D show $f(V)|_{T\rightarrow 0}$ and $D(V)|_{T\rightarrow 0}$. This shows an unexpected similarity between the results of what, for a simple superfluid, would be two distinct experiments - one stimulating the sample thermally and the other mechanically. To examine this effect, we defined an empirical measure τ_E of relaxation times for any combination of T and V (see Equation 2.5):

$$\tau_E(T,V) = \frac{D(T,V)f(0)}{2\omega_0(f(0)-f(T,V))} \tag{2.7}$$

[5] See Appendix A for details of background subtraction employed.

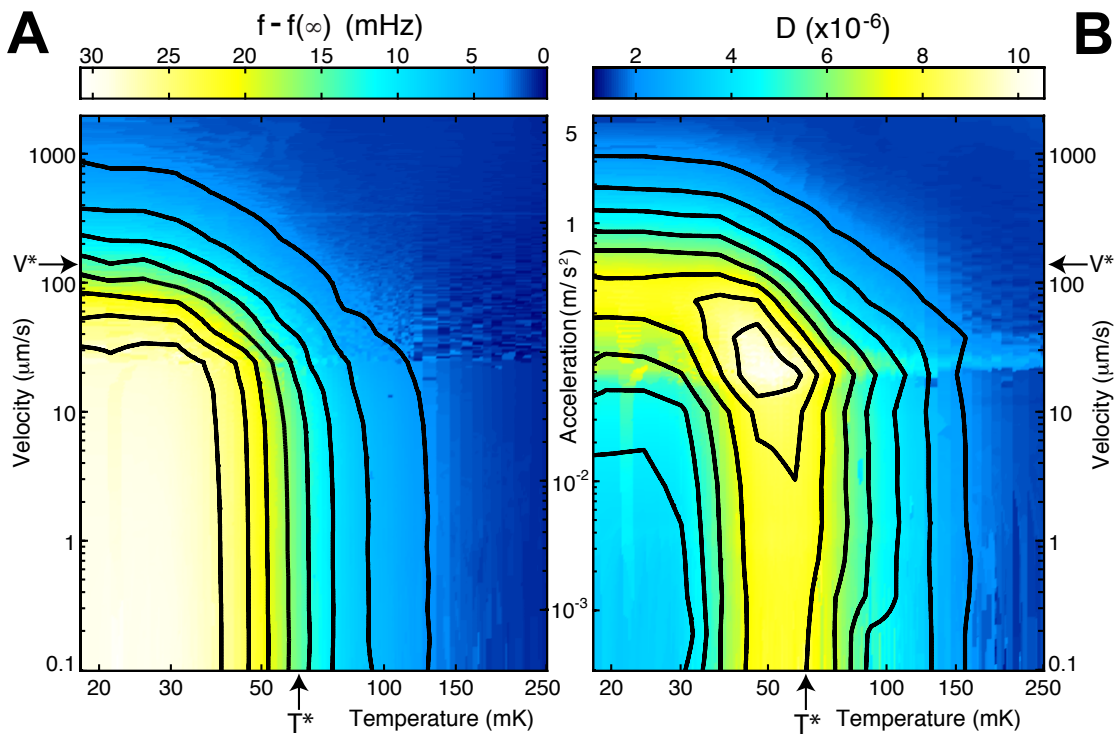

Figure 2.4: **(A)** TO resonant frequency shift $f(T) - f_\infty$ and **(B)** dissipation $D(T)$ data mapped throughout the $V - T$ plane. Ninety eight FID curves (each at a different temperature) were smoothly interpolated into the two color-coded surfaces displayed here on identical log-log axes. The low-velocity maximum frequency shift ($\sim$ 33 mHz) would correspond to a superfluid fraction of 5.6%.

In Figure 2.5 E we show $\log \tau_E(T)$ plotted versus $\log(T/T^*)$ for the lowest rim-velocity data (Figure 2.5 A and C). In Figure 2.5 F, $\log \tau_E(V)$ is likewise plotted versus $\log(V/V^*)$ for the lowest temperature data (Figure 2.5 B and D). Here we define T^* and V^* as the temperature and rim-velocity respectively at which half the total frequency shift has occured (Figure 2.4, 2.5 A and B). This analysis reveals that τ_E diverges smoothly as T^ζ with $\zeta = -2.75 \pm 0.1$ when $V \to 0$, and as V^λ with $\lambda = -1.17 \pm 0.05$ when $T \to 0$. Thus, the effects of temperature on $f(T)|_{V\to 0}$ and $D(T)|_{V\to 0}$ appear identical to those of rim-velocity on $f(V^\gamma)|_{T\to 0}$ and $D(V^\gamma)|_{T\to 0}$ respectively, where $\gamma = \lambda/\zeta = 0.43$ is the ratio of power-law exponents. Figure 2.5 E and F also show that the peak in D is *always* canceled by the peak in $|df/dT|$ to produce smoothly diverging functions $\tau_E(T)|_{V\to 0}$ and $\tau_E(V)|_{T\to 0}$. Microscopic relaxational processes represented by τ_E could be expected

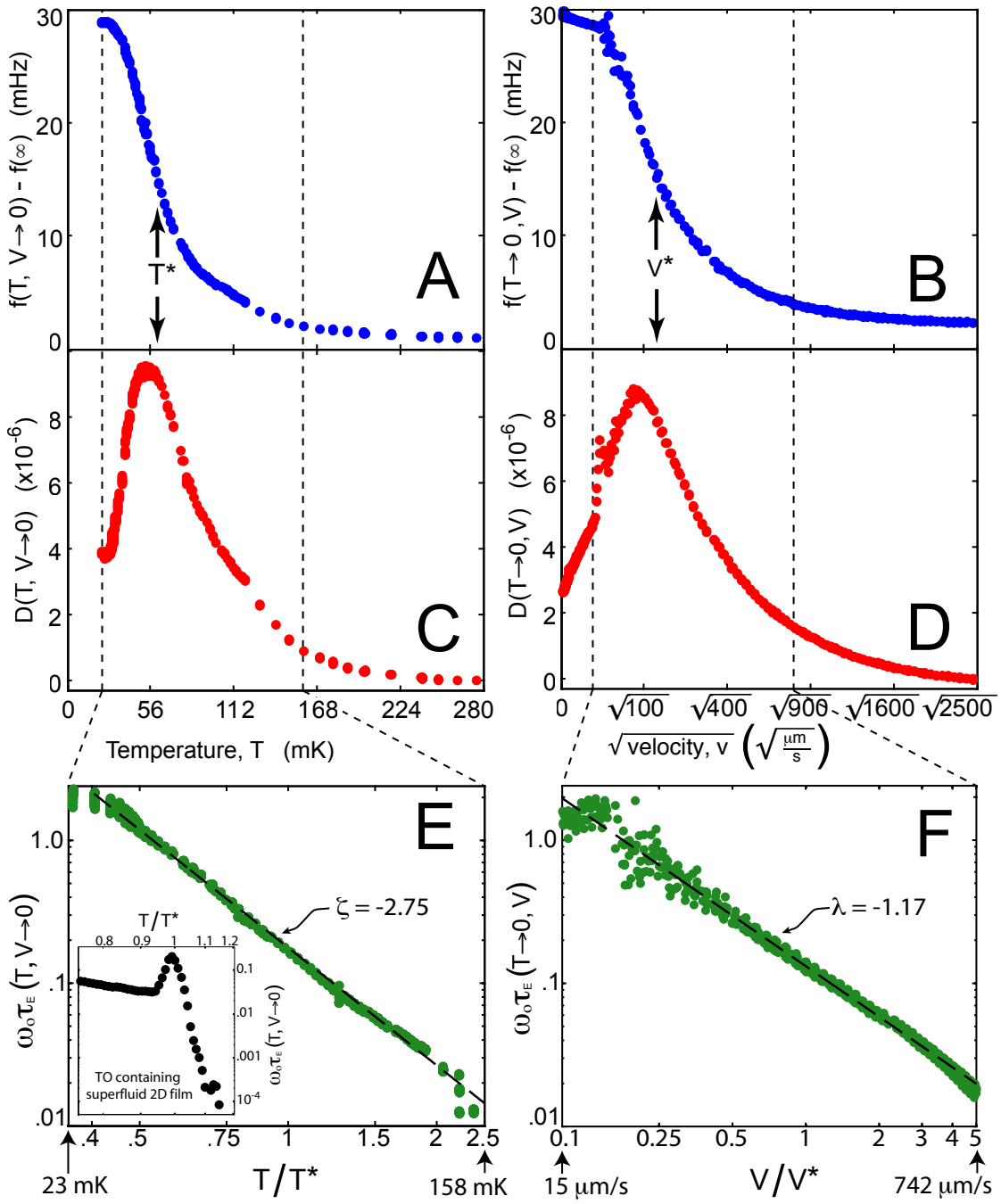

Figure 2.5: **(A)** TO resonant frequency shift $f(T)$ measured at lowest rim-velocity. T^* is defined as the temperature at which 50% of the frequency change has occurred (Figure 2.4). **(B)** TO resonant frequency shift $f(\sqrt{V})$ measured at lowest temperature. V^* is defined as the rim-velocity at which 50% of the frequency change has occurred (Figure 2.4). **(C)** TO dissipation $D(T)$ measured at lowest rim-velocity. **(D)** TO dissipation $D(\sqrt{V})$ measured at lowest temperature. **(E)** The empirical measure of microscopic relaxation times $\omega_0\tau_E(T)|_{V\to 0}$ from data in Figure 2.5 A and C. **(Inset to E)** The equivalent analysis using Eq. 7 for the BKT transition of a superfluid ^{4}He film. **(F)** The empirical measure of microscopic relaxation times $\omega_0\tau_E(V)|_{T\to 0}$ from data in Figure 2.5 B and D.

to change dramatically at a superfluid phase transition; a good example of this is seen in $\tau_E(T)$ at the BKT superfluid phase transition of liquid ^{4}He [15, 2] shown inset to Figure 2.5 E. However, no indications of such a sudden change signifying a supersolid T_c or V_c is observed in Figure 2.5 E and F. Instead, τ_E exhibits everywhere the smooth divergence expected in $\omega\tau = 1$ models.

2.7 Equivalence of Mechanical and Thermal Stimulation of Solid ^{4}He

Figures 2.4 and 2.5 provide direct empirical evidence that the effects of T and V on the solid ^{4}He within the TO are intimately related. One may then ask whether a single rotational susceptibility could describe the whole $V - T$ plane dynamics in Figure 2.4 when the effects of V on the relaxation time τ are correctly incorporated. In attempting to explore this issue we make the simple hypothesis that the a total microscopic relaxation rate $1/\tau(T, V)$ is due to a combination of two effects

$$\frac{1}{\tau(T,V)} = \frac{1}{\tau(T)} + \frac{1}{\tau(V)} \tag{2.8}$$

As the overall phenomenology appears identical as a function of $T^{\zeta}|_{V\to 0}$ and $V^{\lambda}|_{T\to 0}$ (Figure 2.5) and interpolates smoothly between these limits (Figure 2.4) the ansatz:

$$\frac{1}{\tau(T,V)} = \frac{\Sigma}{T^{\zeta}} + \frac{\Lambda}{V^{\lambda}} \tag{2.9}$$

is natural. Here Σ and Λ quantify the relative contributions to the relaxation rate from thermally and mechanically stimulated excitations. Figure 2.6 A shows that by using this ansatz, all the complex solid ^{4}He rotational dynamics in $f(T, V)$ and $D(T, V)$ shown in Figure 2.4 can be collapsed onto just two functions $\Re(\chi^{-1})$ and $\Im(\chi^{-1})$ merely by

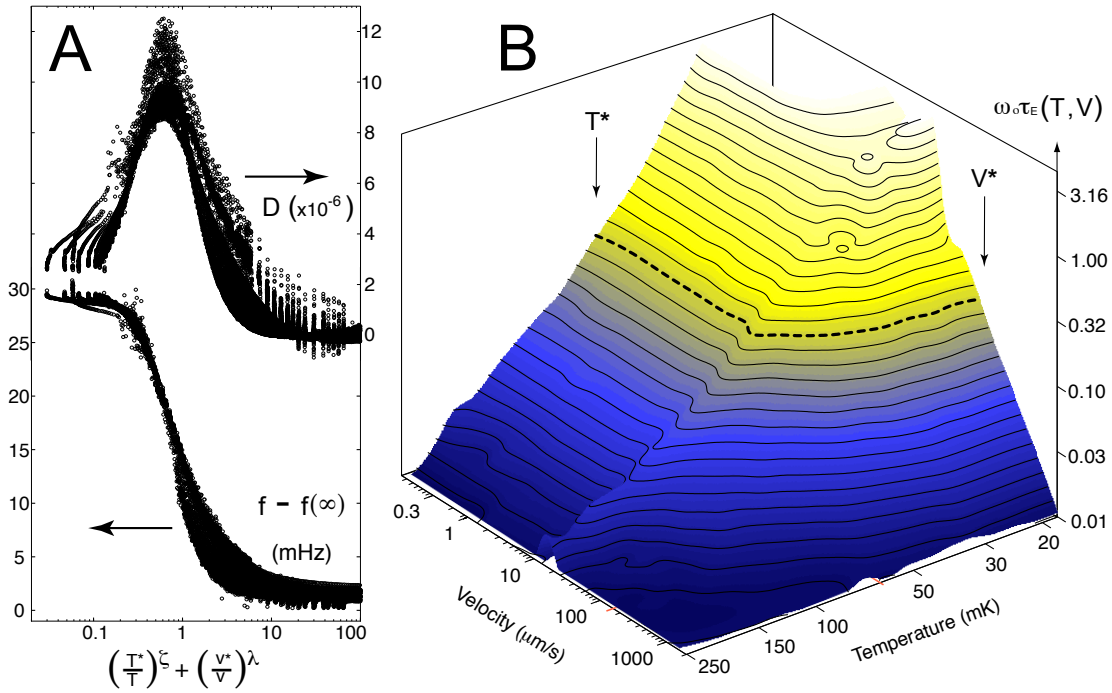

Figure 2.6: **(A)** All of the TO dynamical responses throughout the $V - T$ plane ($f(T, V)$ from Figure 2.4 A and $D(T, V)$ from Figure 2.4 B) are collapsed onto just two curves (very similar in structure to the $\Re(\chi^{-1})$ and $\Im(\chi^{-1})$ components of the Debye susceptibility) by plotting $f[(T^*/T)^{\zeta} + (V^*/V)^{\lambda}]$ and $D[(T^*/T)^{\zeta} + (V^*/V)^{\lambda}]$. Here we find that $\Re(\chi^{-1}) \propto f[(T^*/T)^{\zeta} + (V^*/V)^{\lambda}]$ is always too large in comparison to $\Im(\chi^{-1}) \propto D[(T^*/T)^{\zeta} + (V^*/V)^{\lambda}]$ to be explained quantitatively by a Debye susceptibility model; this point has been used to motivate a superglass hypothesis [37]. **(B)** A comprehensive map of empirical relaxation times $\omega_0\tau_E(T, V)$ deduced using Equation 2.7 represented as a surface in the $\log T - \log V$ plane. The equally-spaced contour lines in $\log \omega_0\tau_E(T, V)$ reveal the underlying divergence of $\omega_0\tau_E(T, V)$ as combined power laws $[(T^*/T)^{\zeta} + (V^*/V)^{\lambda}]$.

plotting $f[(T^*/T)^{\zeta} + (V^*/V)^{\lambda}]$ and $D[(T^*/T)^{\zeta} + (V^*/V)^{\lambda}]$. This collapse implies, further, that Equation 2.7 could yield a comprehensive image of $\tau_E(T, V)$ throughout the $V - T$ plane by dividing all the data in Figure 2.4 B by that in Figure 2.4 A, as shown in Figure 2.6 B. Here, although the proposed $V - T$ ranges for a supersolid phase transition [45, 44, 50] are at or below the dashed $T^* - V^*$ contour, the τ_E surface exhibits everywhere the smoothly diverging relaxation processes expected in $\omega_0\tau = 1$ models. We emphasize that all the above empirical results (Figures 2.4-2.6) are independent of the choice of $\chi^{-1}_{^4He}(T, V)$.

2.8 Relating Solid ^{4}He Shear Dynamics to the Rotational Susceptibility

Measurements of the shear modulus μ of solid ^{4}He by Day and Beamish [28] revealed that the temperature dependence of the shear modulus $\mu(T)$ is highly similar to the temperature dependence of the frequency $f(T)$ measured in TOs. They also observed a corresponding dissipation peak in the shearing experiments [28]. Furthermore, they discovered that μ has the same dependence on the amplitude of shear strain ε, ^{3}He concentration, and annealing as does the TO frequency f on rim velocity, ^{3}He concentration, and annealing [28]. Because the solid ^{4}He shear modulus $\mu(T)$ exhibits a very similar temperature dependence to $f(T)$ [28], and because this shear stiffening effect is extinguished by a characteristic strain as opposed to a critical velocity [29], a key issue is whether the microscopic excitations generated by direct shearing are the same as those controlling the TO dynamics. Our approach provided a new opportunity to directly examine this issue.

Figures 2.4 and 2.5 provide evidence that identical microscopic excitations are being generated by thermal and mechanical stimulation, and that the overall rotational dynamics in $f(V,T)$ and $D(V,T)$ are consistent with a single $\omega_0\tau = 1$ mechanism that is controlled by a relaxation rate $(T^*/T)^\zeta + (V^*/V)^\lambda$ due to the combined influences from these two sources (Figure 2.6). If excitations induced by inertial strain ε in the TO (where $\varepsilon \propto V$) are the cause of the anomalous rotational dynamics, then the indistinguishable structure of $f(T)|_{V\to 0}$ and $f(V^\gamma)|_{T\to 0}$ (Figure 2.7 A) should be mirrored by an equivalently indistinguishable relationship in shear modulus between $\mu(T)|_{\varepsilon\to 0}$ and $\mu(\varepsilon^\gamma)|_{T\to 0}$. When the measured μ from Ref. [29] is plotted simultaneously versus T and ε^γ in Figure 2.7 B (using the power-law ratio γ derived from our TO studies), this is what

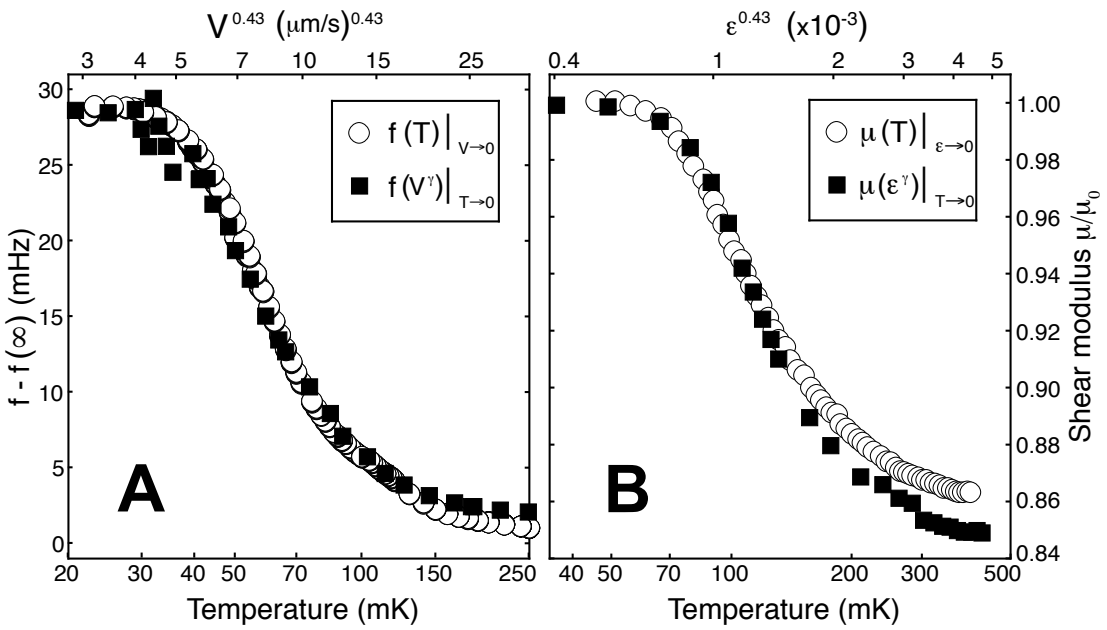

Figure 2.7: **(A)** Plots of our simultaneously measured $f(T)|_{V\to 0}$ (open circles) and $f(V^{\gamma})|_{T\to 0}$ (filled squares) from Figures 2.4 and 2.5. **(B)** Simultaneous plots of measured $\mu(T)|_{\varepsilon\to 0}$ (open circles) and $\mu(\varepsilon^{\gamma})|_{T\to 0}$ (filled squares) from Ref. [29] acquired at 2000 Hz.

we find. That the combined temperature-velocity dependence of the TO response mirrors quantitatively the combined temperature-strain dependence of the shear modulus, along with the original observation that $\mu(T)$ tracks $f(T)$ [28], implies strongly that the rotational dynamics of solid ^{4}He are closely associated with the generation (presumably by inertial shearing) of the same type of microscopic excitations which are generated by direct shear strain ε. These deductions are also in good accord with the absence of any signature in estimated relaxation times $\tau_E(T, V)$ for the T_c or V_c of the proposed supersolid phase transition (Figures 2.5 and 2.6), and the associated observation of the universal smoothly diverging $\tau_E(T, V)$ expected in $\omega\tau = 1$ models.

2.9 Conclusions

In this chapter we described the development and implementation of novel high-precision and high-data-volume techniques for TO studies of solid ^{4}He. Our DC-SQUID-based TO system allows unprecedented sensitivity and dynamic range making the free inertial decay technique viable, and yielded the first comprehensive map of $f(T,V)$ and $D(T,V)$ for solid ^{4}He. Our introduction of the generalized rotational susceptibility $\chi^{-1}_{^4He}(\omega,T)$ technique also allows an unbiased approach to studying solid ^{4}He rotational dynamics. Moreover, a specific model for $\chi^{-1}_{^4He}(\omega,\tau(T))$ in which $\tau(T)$ represents the relaxation rate for inertially active microscopic excitations provides an intuitively satisfying model for why df/dT and D pass simultaneously through a maximum when $\omega\tau(T^*) = 1$. Our studies reviewed here have all been carried out in the context of these new approaches to the solid ^{4}He problem.

Solid ^{4}He sample characteristics are notoriously non-universal. And indeed, in our studies, we found that equilibration times within $f(T)$ and $D(T)$ exhibit a complex synchronized ultraslow evolution toward equilibrium indicative of uncontrolled glassy freezing of crystal disorder conformations. During this slowing down, the synchronized relationship of $\Re(\chi^{-1}_{^4He})$ to $\Im(\chi^{-1}_{^4He})$ is always retained, meaning that each precise crystal disorder conformation strongly influences the rotational dynamics. Such slow conformation changes linked to rotational dynamics are actually endemic to studies of solid ^{4}He and are manifested variously as hysteresis effects [9, 60], annealing effects [74, 79, 75, 22, 23, 78], and glassy dynamics [37, 23, 10, 33].

However, once a given disorder conformation has been stabilized (the situation in which most solid ^{4}He studies are presumed to be carried out) we found that analysis of $\chi^{-1}_{^4He}(\omega,\tau(T,V))$ provides evidence that microscopic excitations controlling the TO mo-

tions are generated independently by thermal and mechanical stimulation of the crystal. Moreover, a measure for their relaxation times $\tau(T, V)$ diverges smoothly everywhere, as expected in $\omega\tau = 1$ models with no indication whatsoever of a thermodynamic transition. Finally, the combined temperature-velocity dependence of the TO response is indistinguishable from the combined temperature-strain dependence of the ^{4}He shear modulus directly linking the shearing characteristics to the TO effects.

Overall, our observations imply that ultra-slow equilibration of crystal disorder conformations continues to evolve even at lowest temperatures in solid ^{4}He. Then, for any given disorder conformation, the rotational responses of solid ^{4}He are associated with generation of the same microscopic excitations as those produced by direct shear strain. If superfluidity is the correct interpretation of the blocked annulus experiments [44, 76], then one hypothesis consistent with all these observations is that amorphous low temperature solid ^{4}He is a superglass a state in which dynamical excitations within the solid control the superfluid phase stiffness. A key experiment to test this hypothesis would use a variable frequency oscillator to measure the frequency dependent rotational susceptibility (see Appendix D). Firstly, by severely constraining theoretical models, such a susceptibility would help identify if these microscopic excitations are crystal dislocations as implied. Secondly, if a superfluid component does exist, then the real and imaginary parts of this susceptibility would not satisfy the Kramers-Kronig relations.

CHAPTER 3

SEARCH FOR MASS TRANSPORT THROUGH SOLID ^{4}HE

In this chapter[1] we introduce a novel apparatus, the mass flow chip, designed to directly detect mass flow through solid ^{4}He. The mass flow chip allows the detection of AC mass flow. We first present the design and construction of the chip, followed by some recent results for searches for AC mass flow. We find no evidence for mass flow through solid ^{4}He and put limits on the maximum mass current density allowed by our signal to noise. Finally, we present some recommendations for how the design and construction of the chip could be improved so that more stringent limits on flow may be obtained.

3.1 Previous Mass Flow Studies in Solid ^{4}He

Soon after Kim and Chan's claim that solid ^{4}He enters a supersolid state, Day and Beamish attempted to force solid helium thorough an array of fine capillaries [27]. Their setup consisted of two cylindrical chambers separated by a superleak, which was an array of 36000 3 mm long 25 μm diameter holes. The outer wall of the larger chamber was a flexible membrane which could be moved using a piezoelectric actuator. The smaller chamber contained a sensitive capacitive pressure gauge. Day and Beamish found no evidence for low temperature pressure-driven flow and were able to put stringent limits on the flow velocity. The average flow velocity was determined to be less than 1.2×10^{-14} ms^{-1}, 7 orders of magnitude less than the critical velocity inferred by Kim and Chan [45].

Rittner *et al.* [73] searched for low frequency (mHz) supersolid flow by applying an

[1] The work described in this chapter was done in collaboration with E. Kassner, E. J. Pratt, and J. C. Davis.

ac pressure gradient to a sample of solid ^{4}He. They find no evidence for superflow and set an upper bound of 9.6×10^{-4} nm/s on the mass transport velocity and 8.4×10^{-6} for the supersolid fraction at 25 mK.

Although the experiments of Day and Beamish [27] and Rittner *et al.* [73] did not observe significant flow of solid ^{4}He, it can be argued that applying mechanical pressure on the solid (squeezing the lattice) might not be the best strategy to induce flow. Another idea is to connect two reservoirs of superfluid to each other through the solid and introduce a chemical potential difference between them. If solid ^{4}He is able to provide a path for superflow, helium atoms should go from one reservoir to the other. We discuss the implementation of this idea in the following section. Hallock and collaborators [34] have also used this idea to search for DC mass transport through solid ^{4}He. Their apparatus consists of two reservoirs of superfluid ^{4}He connected to each other through nanoporous Vycor rods in series with a sample of solid ^{4}He. They introduce a chemical potential between the two reservoirs either by using the thermomechanical effect or by direct mass injection. All their observations are made off but near the melting curve. Their principal results are that no DC flux of atoms was observed above 650 mK while an increasing flux was seen as the temperature was lowered below 650 mK, with a flux minimum between 75-80 mK. They have interpreted these observations as being caused by a Bosonic Luttinger liquid. While the result of Hallock *et al.* [34] are extremely interesting, their connection to the Kim and Chan effect is not yet clear.

3.2 A Proposal for the Direct Measurement of Mass Flow

As discussed above, the idea is to connect two reservoirs of superfluid to each other through the solid and introduce a chemical potential difference between them. The first

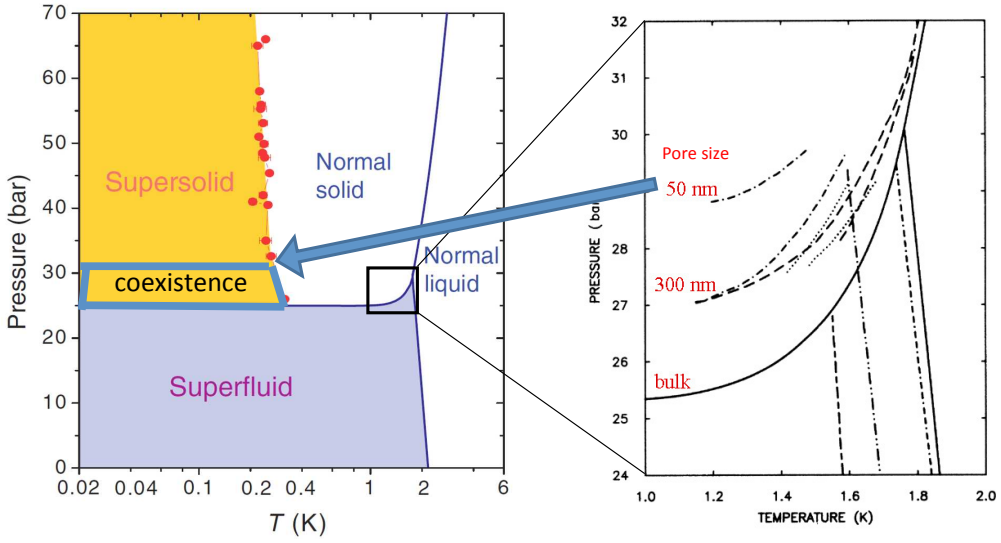

Figure 3.1: Confinement of ^{4}He in nanometer-sized pores raises the pressure required for solidification. This property allows the fabrication of a new class of device in which solid and superfluid ^{4}He can coexist next to each other at the same temperature and pressure if a bulk region is present adjacent to a porous material. Figure adapted from [44] and [49].

technical challenge for the proposed experiment is figuring out how to have superfluid and solid coexisting at the same temperature and pressure. For this, we turn to the properties of ^{4}He in confined geometries. The phase diagram of ^{4}He confined to nanometer sized pores is modified in two major respects [49]. Firstly, the superfluid transition temperature is lowered and more importantly for the present proposal, the pressure required for solidification is increased. The right panel of Figure 3.1 shows the relevant parts of the phase diagram for a number of different pore sizes. This immediately suggest a coexistence region on the phase diagram (see left panel of Figure 3.1) in which, at the same temperature and pressure, we have stable solid in bulk regions and stable superfluid in porous regions. The smaller the pores, the larger is the coexistence region.

The apparatus, then, should consist of two porous regions separated by a bulk region. This geometry would allow solid ^{4}He to be sandwiched between two superfluid reservoirs. We now address the problem of how to drive and detect superfluid from one

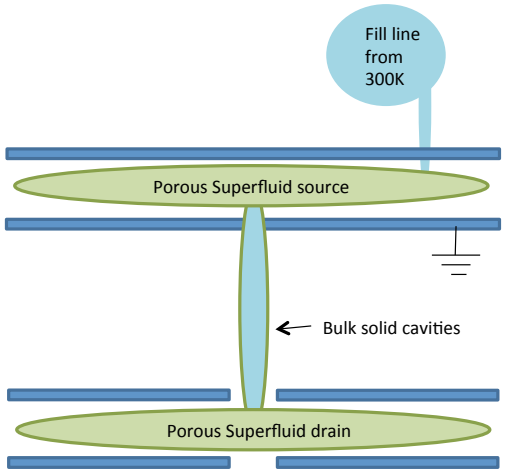

Figure 3.2: Schematic of the mass flow chip. Two porous superfluid reservoirs (the source and the drain) are connected through bulk solid cavities. The reservoirs are sandwiched between metal electrodes for capacitive drive and detection. The drain electrode is split to enable superfluid transport detection within the drain when the bulk is filled with solid.

reservoir to the other. Unlike Hallock and colleagues [34] who used the themomechanical effect and direct mass injection with a pressure gradient, we propose capacitive drive and detection. The superfluid reservoirs are placed between the plates of a capacitor. When a voltage is applied between these plates, an electric field is produced in the reservoirs. The principal difference between this scheme and the pressure gradient scheme is that the applied electric field penetrates the entire reservoir and changes the chemical potential for the whole superfluid. The second advantage of this scheme is that it allows the entire experiment to be cold (and at the same temperature throughout). We propose to use capacitors to detect flow as well. If ^{4}He atoms flow into a reservoir and increase the density, the increased effective dielectric constant can be detected as an increased capacitance. Similarly, an outward flow should result in a decreased capacitance.

A schematic implementation of the mass flow chip is depicted in Figure 3.2. The two reservoirs are the porous superfluid source and the porous superfluid drain. These two reservoirs are separated by bulk cavities. If the pores are of the right size and the temper-

ature and pressure are in the coexistence region, we expect superfluid in the source and drain and solid in the bulk cavities. The reservoirs are sandwiched between capacitor plates for capacitive drive and detection. Notice that the drain capacitor electrodes are split. This arrangement can be used to demonstrate the existence of superfluid in the pores when the bulk cavities are solid.

3.3 Construction and Assembly of the Mass Flow Chip

Figure 3.3 depicts the functional electrode schematic of the mass flow chip. The chip is built from three macor plates - the top, center, and bottom plates (not shown in the figure). The electrodes are sputtered onto the macor plates in the pattern shown. The top and bottom plates have one side coated with gold and the center plate has both sides coated. The center macor plate has 13 0.4 mm dia $\times$ 1 mm holes drilled in it which serve as the bulk cavities separating the source and drain reservoirs. The bottom electrode for the source reservoir is grounded. Notice that the drain electrodes are split into the spot and ring electrodes. This feature of the design is meant to allow intra-drain transport studies. Specifically, this was designed so we could demonstrate the existence of liquid in the pores (by sloshing liquid back and forth between the spot and ring) when there is solid in the bulk cavities.

The following procedure was followed for the assembly of the mass flow chip (see Figure 3.4 for a few snapshots of the assembly process):

1. Machining: All the macor plates and teflon ballasts were machined. The complete set of machine drawings is presented in Appendix B.
2. Electrode deposition: The macor plates were polished before electrode deposi-

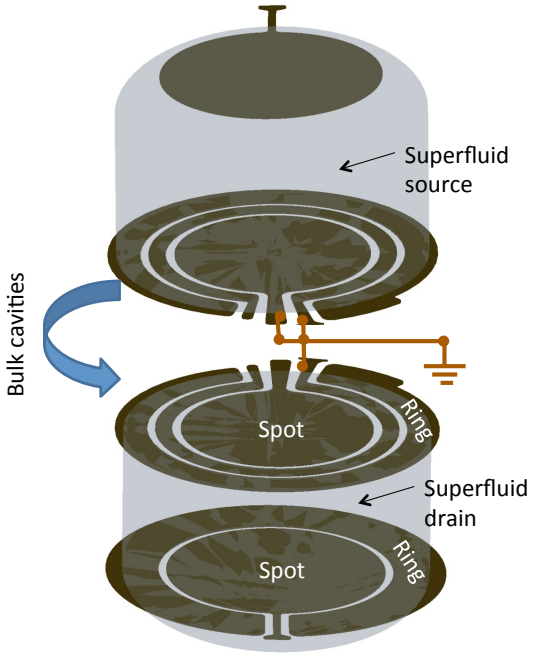

Figure 3.3: Electrode functional schematic of the mass flow chip. The electrodes are deposited on three macor plates (not shown) - the top, the bottom, and the center plates. One side of the top and bottom plates serves as electrodes while both sides of the center plate serve as electrodes. The center macor plate has 13 cylindrical holes (0.4 mm dia × 1 mm) drilled in it which serve as the bulk cavities connecting the source and drain reservoirs.

tion. For the top and bottom macor plates, a titanium (Ti) adhesion layer (50 nm) followed by a platinum (Pt) electrode layer (150 nm) were sputtered. For the center macor plate, a chromium (Cr) adhesion layer (25 nm) followed by a gold (Au) electrode layer (100 nm) were sputtered. The patterns were created using scissors and carbon tape with mylar as a mask. See Figure 3.4A.

3. Porous Layers: The porous reservoirs were made by firing zirconia tape obtained from the Maryland Ceramic and Steatite Company Inc. The 17 μm tape consists of grains of ceramic in an organic glue. The organic glue evaporates at $\sim$ 800 C and at higher temperatures (800 - 1400 C) the ceramic grains begin to coalesce, forming a dense mass at $\sim$ 1400 C. At intermediate temperatures, a porous material is formed, with smaller pores at higher temperature. The top and bottom macor plate electrode surfaces (after electrode deposition) were laminated with

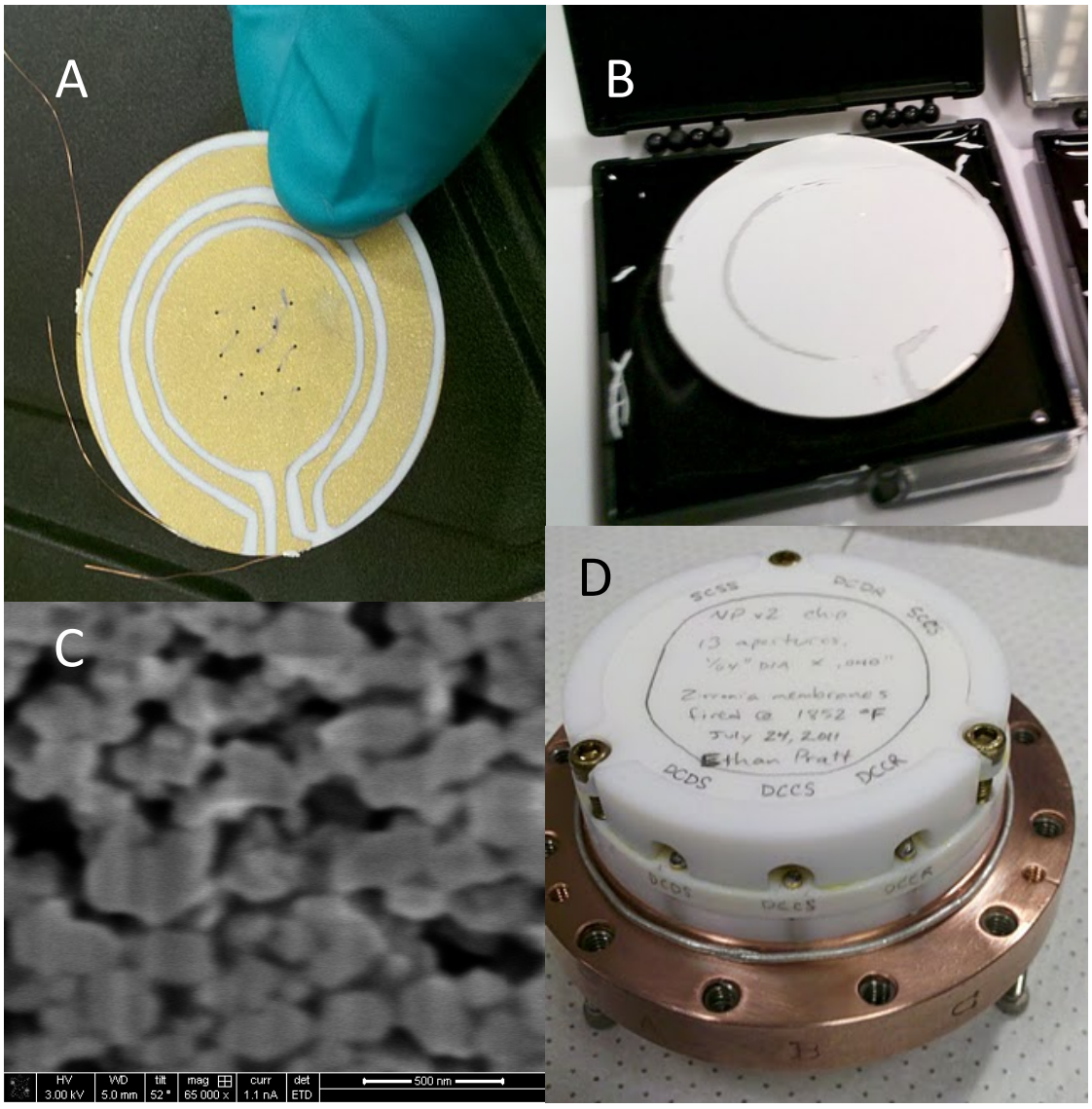

Figure 3.4: Some snapshots in the assembly process of the mass flow chip. **(A)** The center macor plate (view of drain side) sputtered with gold electrodes. Also visible are the 13 bulk cavities drilled through the center plate and the wires coming off the electrodes. **(B)** The macor bottom plate laminated with zirconia tape and fired at 1000 C. **(C)** A scanning electron microscope (SEM) image of the fired zirconia tape taken from the drain reservoir showing the pores. **(D)** The fully assembled chip on the bottom piece of the copper housing or cell. The top piece will subsequently fully enclose the chip.

zirconia tape and fired at 1000 C (see Figure 3.4B). This created a porous layer adjacent to the electrodes (see Figure 3.4C).

4. Putting the plates together: The three macor plates - the top plate with the platinum electrode and the porous source reservoir, the bottom plate with the platinum electrode and the drain reservoir, and the center plate with gold electrodes on either side and the bulk cavities - are pressed together, secured with the teflon ballasts, and placed in the copper cell (see see Figure 3.4D and Figure B.1).

The copper cell, which is mounted on the cryostat and thermally linked to the mixing chamber, has coaxial cables connections for the various electrodes. It also houses a Straty-Adams type capacitance pressure gauge to measure the the pressure of the solid ^{4}He or superfluid sample under study. A fill line from 300 K leads into the cell and is used for filling the mass flow chip with ^{4}He as described in the next section.

3.4 Filling the Mass Flow Chip with ^{4}He

In this section, we discuss filling the mass flow chip with superfluid and solid ^{4}He.

3.4.1 Superfluid ^{4}He Filling and Porosity

Figure 3.5 shows the capacitance of the drain capacitor as a function of time during which the mass flow chip was filled with superfluid ^{4}He. The capacitance increases as the cell is filled, as expected. We can estimate the porosity (fraction of volume that is empty in the porous reservoirs) from this increase in capacitance. Working with a highly simplified model, we assume that the drain capacitor (of area A and separation

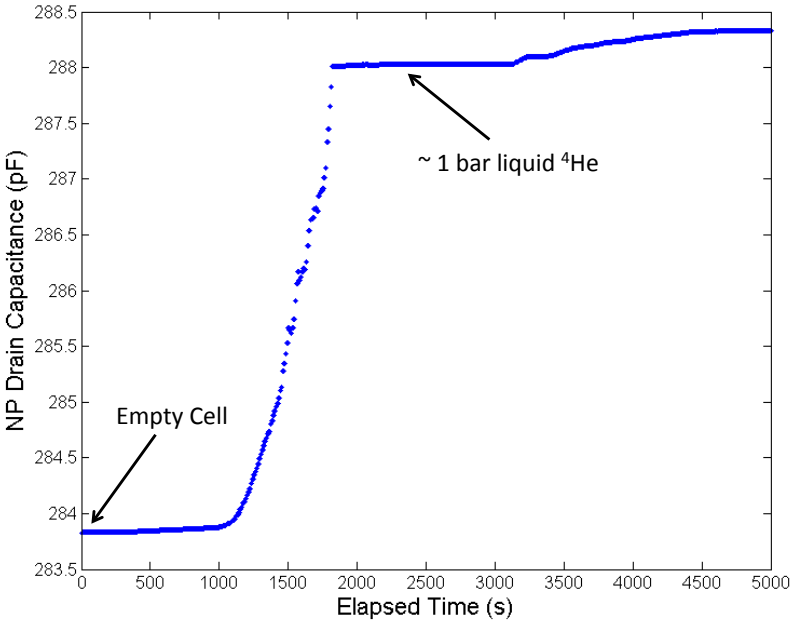

Figure 3.5: Filling the cell with superfluid ^{4}He

d) consists of two capacitors in parallel, one completely empty (of area pA) and one entirely filled with dielectric (of area $(1-p)A$), both of separation d. The porosity, then, is given by p.

To determine p we note that the change in capacitance of the drain capacitor upon filling with liquid helium is given by

$$\Delta C = \frac{(\epsilon_{He} - \epsilon_0)pA}{d}. \tag{3.1}$$

In terms of the dielectric constant κ of liquid ^{4}He we have for the porosity

$$p = \frac{d\Delta C}{\epsilon_0(1-\kappa)A}. \tag{3.2}$$

Using $d = 17\ \mu$m, $\Delta C \sim 4$ pF (from Figure 3.5), $\kappa \sim 1.05$, and the radius of the drain electrode $r \sim 22$ mm, we estimate a porosity $p \sim 10\%$.

3.4.2 Solid ^{4}He Sample Formation

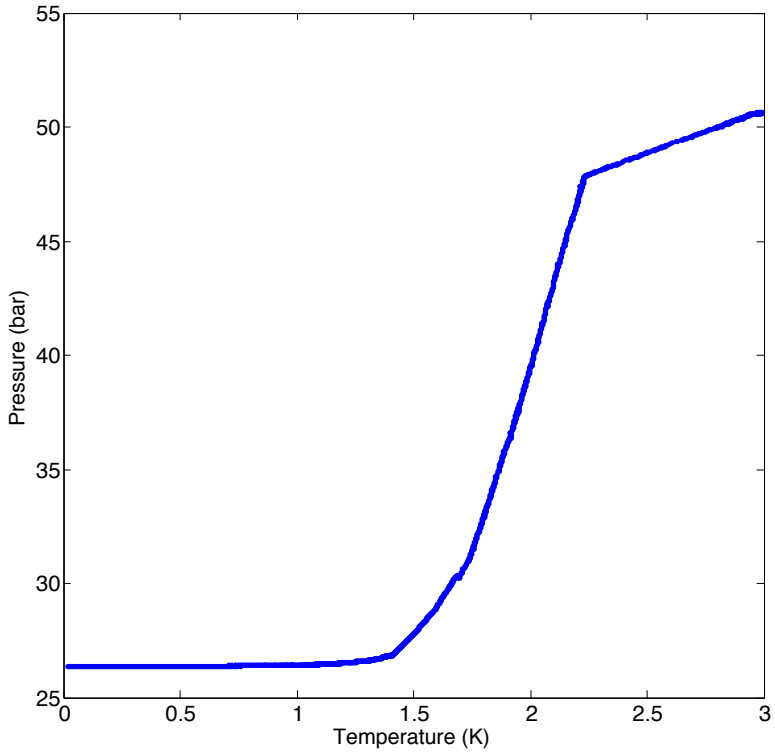

Figure 3.6: Pressure-temperature plot during solid ^{4}He sample formation.

The solid sample was formed using the blocked capillary method, similar to what is employed in most torsional oscillator studies. Figure 3.6 shows the pressure-temperature diagram of sample preparation. The cell is first filled with liquid ^{4}He to a high pressure ($\sim$ 50 bar) at $\sim$ 3 K. The temperature is then rapidly reduced. The pressure decreases linearly till it hits the melting curve, which it then follows. The curve subsequently pinches off the melting curve and flattens out resulting in an over pressure.

Figure 3.7 shows our procedure for estimating the overpressure of the solid ^{4}He sample. A sample is first formed on the melting curve and the pressure reached at low temperature ($<$ 20 mK) is recorded as P_0. When $\log(P - P_0)$ is plotted against $\log(T)$ for both the sample formed on the melting curve and the solid sample (see above), it

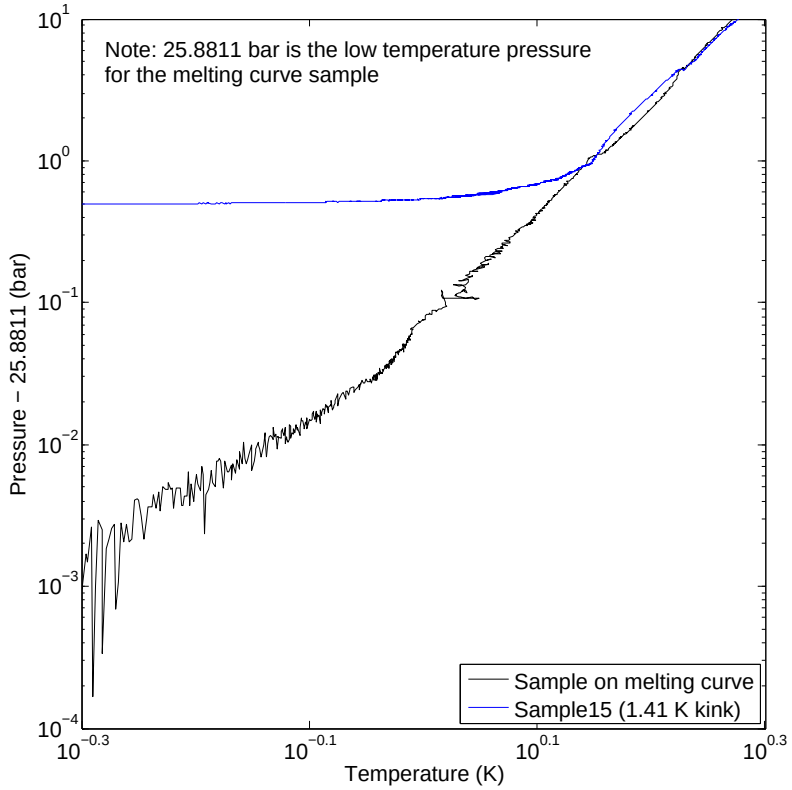

Figure 3.7: Plot showing the formation of a sample of solid ^{4}He. A sample is first formed on the melting curve (black) and the pressure reached at low temperature (< 20 mK) is recorded as P_0. When $\log(P - P_0)$ is plotted against $\log(T)$ for both the sample formed on the melting curve and the solid sample, it can be clearly seen that the solid sample pinches off the melting curve at ∼1.41 K and reaches a low temperature overpressure above the melting curve of ∼0.5 bar.

can be clearly seen that the solid sample pinches off the melting curve at ∼1.41 K and reaches a low temperature overpressure above the melting curve of ∼0.5 bar. Since our pore sizes were large, we wanted to have as little over pressure as possible while being sure that we had a solid sample. As the overpressure becomes small (less than ∼1 bar), it becomes difficult to see the kink on a simple P-T plot like that shown in Figure 3.6 but can still be seen clearly using the procedure outlined here (Figure 3.7). This procedure does not rely too sensitively on the calibration of the pressure gauge.

3.5 Acoustic Flow Measurements

We now discuss a mass flow detection scheme that involves measuring acoustic resonances when the apparatus is filled with superfluid ^{4}He. This acoustic resonance technique provides an opportunity to search for AC mass flow in the kilohertz range, which is comparable to torsional oscillator frequencies. We find that when the apparatus is filled with solid ^{4}He, the acoustic peaks, and hence mass flow, can no longer be observed. We then consider the upper limits on the mass current density J that can be placed within the framework of two different supersolid models.

3.5.1 Predictions for Bessel Modes in the Mass Flow Chip

We can use the wave equation with the appropriate boundary conditions to calculate the first few acoustic modes expected in the mass flow chip. The wave equation is given by

$$\nabla^2 z = \frac{1}{v^2}\frac{\partial^2 z}{\partial t^2} \tag{3.3}$$

where v is the speed of the vibration (the speed of sound in our case). Solving the wave equation for a cylindrical geometry with the boundary condition that the displacement is 0 at the edge of the cylinder at radius $r = a$ yields:

$$z = J_n(kr/a)\left\{\begin{array}{c}\sin n\theta\\ \cos n\theta\end{array}\right\}\left\{\begin{array}{c}\sin kvt/a\\ \cos kvt/a\end{array}\right\} \tag{3.4}$$

Using the solution, we get the mode frequencies to be

$$f = \frac{\omega}{2\pi} = \frac{kv}{2\pi a} \tag{3.5}$$

where the possible values of k are the zeros $k(m,n)$ of the Bessel functions. The smallest four $k(m,n)$ values predict the following mode frequencies:

$$\begin{aligned} k(1,0) &= 2.4 \quad f_{10} = 4117.5 \text{ Hz} \\ k(1,1) &= 3.8 \quad f_{11} = 6560.7 \text{ Hz} \\ k(1,2) &= 5.1 \quad f_{12} = 8793.2 \text{ Hz} \\ k(2,0) &= 5.5 \quad f_{20} = 9451.5 \text{ Hz} \end{aligned} \tag{3.6}$$

using speed of sound at low temperature (20 mK) to be 235 ms^{-1} and the radius of the cylinder to be 2.2 cm.

3.5.2 Acoustics Measurement Setup and Superfluid Peaks

A schematic of the setup used to measure the acoustic signals is shown in Figure 3.8. The mass flow cell is shown enclosed in a red box. The basic idea of the acoustic measurements is to apply a combination of an AC ripple and a large DC voltage ($V = V_{\text{AC}} + V_{\text{DC}}$) to the drive reservoir (represented by the solid-line capacitor on the left) and measure an AC signal at the detect reservoir (represented by the solid-line capacitor on the right). The purpose of V_{DC} is to make the applied pressure, which goes as V^2 linear in V_{AC}. Furthermore, the applied pressure is amplified (it now goes as $2V_{\text{AC}}V_{\text{DC}}$) without having to apply dangerously hight AC voltages.

We found that there was some electrical AC crosstalk between the drive and detect capacitors. In other words, when a pure AC ripple was applied to the drive capacitor, a fraction of this drive signal was being measured across the detect capacitor regardless of drive frequency. This electrical cross talk is shown schematically as the capacitors (drawn in dotted lines) coupling the two reservoirs in the figure. This presents a problem in measurement because now the detected signal contains both the genuine signal due

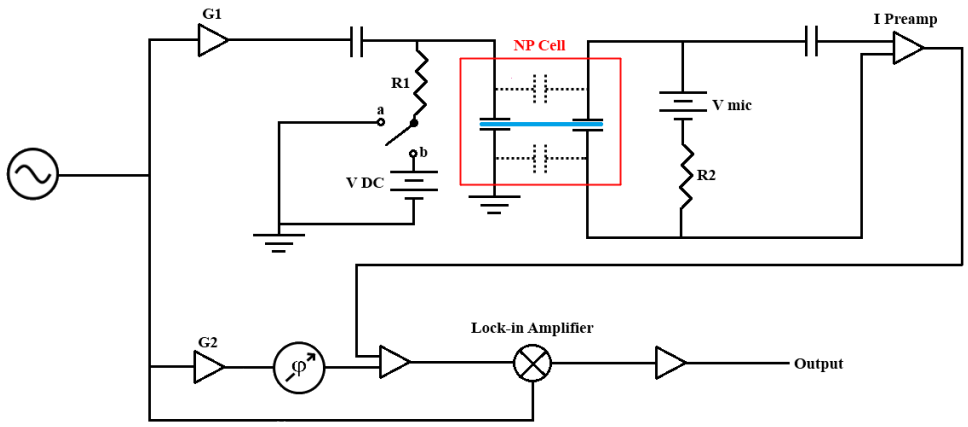

Figure 3.8: Schematic of the acoustic flow measurement setup. The drive capacitor receives an AC signal with a DC bias. An oscillator applies the AC signal, while the switch position determines the applied DC bias. When the switch is in position (a), 0 V DC bias is applied to the cell; the cell receives 200 V DC bias when the switch is in position (b). The large bias serves to make the net applied pressure, which goes as V^2, linear in V_{AC} and allows us to access regimes of applied pressure not accessible through pure AC driving voltages in our setup. A bias of 225 V is applied to the detect-side capacitor to make the response linear in V_{AC}. Changes in the detect-side capacitance cause currents that go to a current pre-amp, and the resulting signal is then routed to a lock-in input. Due to some electrical crosstalk (dashed lines), we found it necessary to actively cancel background signal (defined as the signal at 0 V DC bias) in order to maximize measurement sensitivity; this was done at 0 V bias by finding the amplitude (G2) and phase (φ) necessary to minimize the differential lock-in signal at 0 V bias. Signals at non-zero DC bias were then measured while holding the amplitude G2 and phase (φ) at the values optimized for the particular applied frequency.

to flow and the signal due to electrical crosstalk. To circumvent this problem, we implemented a crosstalk cancellation scheme in which the signal measured with $V_{DC} = 0$ (the cancellation signal) is subtracted from the signal obtained when the DC bias was applied. In this manner, the signal due only to flow can be isolated.

Figure 3.9 shows the acoustic peaks measured in the mass flow chip using the acoustic measurement setup discussed above. The lowest four observed frequencies are at 2022.0 Hz, 3048.8 Hz, 3618.0 Hz, and 4000.5 Hz. As we can see the predicted and observed frequencies are about a factor of 2 off. We are approximating the geometry inside the mass flow chip to be a perfect cylinder of radius a = 2.2 cm. This might not

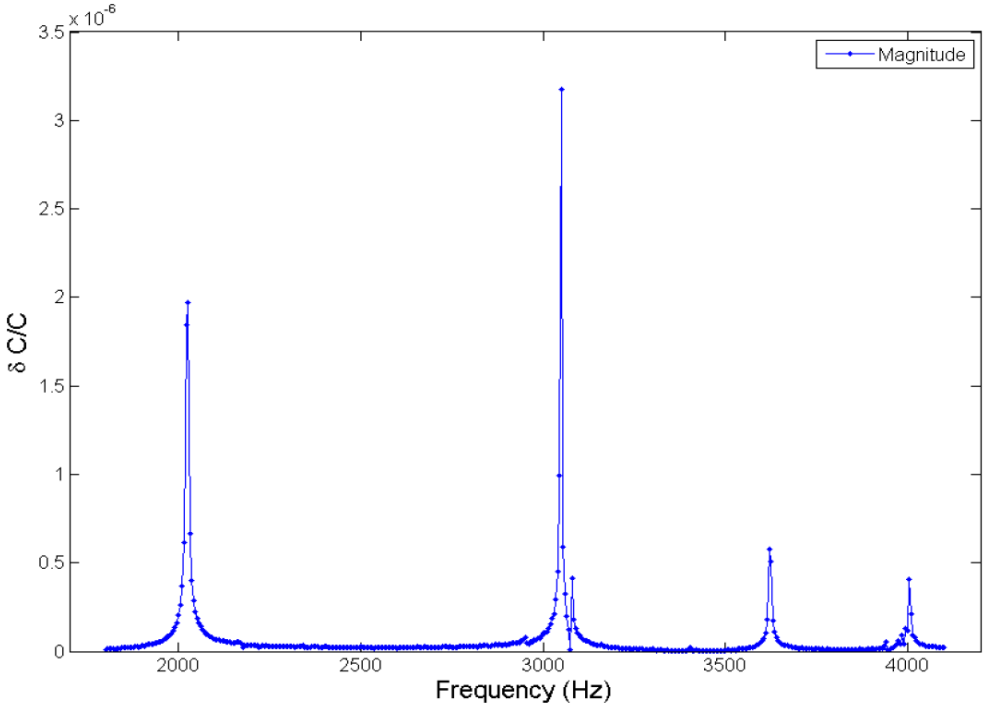

Figure 3.9: The acoustic spectrum observed using the acoustic measurement scheme when the mass flow chip was filled with superfluid at 6 bar. The data were collected at 5 Hz resolution.

be a valid assumption. Even if the effective radius is different, the ratios of the modes should be approximately right. Table 3.1 compares the predicted and observed ratios of the mode frequencies to that of the lowest modes. The ratio of the first two modes is close (off by ~5%). The ratios of the higher modes are worse. It is possible that these discrepancies are due to the the actual shape of the chip electrodes not being an ideal cylinder. We also confirmed that the observed peaks scaled linearly with drive voltages (both V_{AC} and V_{DC}).

As mentioned in Section 3.3, the reservoirs are made of a porous ceramic tape. It is very important to know if helium within these pores are feeling any effects of confinement. The simplest way to find out is to measure the temperature dependence of the observed acoustic peaks. If the acoustic peaks are due to liquid helium that is confined, the peak frequency should follow Equation 3.5 with the velocity v interpreted

Mode	Predicted Frequency (Hz)	Observed Frequency (Hz)	Predicted Ratio (freq./freq. (1,0))	Observed Ratio (freq./lowest freq.)
(1,0)	4117.5	2022.0	1.0	1.0
(1,1)	6560.7	3048.8	1.6	1.5
(1,2)	8793.2	3618.0	2.1	1.8
(2,0)	9451.5	4000.5	2.3	2.0

Table 3.1: Comparison of the first four predicted and observed acoustic peaks.

as the fourth sound velocity. On the other hand, if the acoustic signal is originating from unconfined liquid helium, the velocity v should be interpreted as the first sound velocity. Figure 3.10 shows such a comparison. The peak frequency normalized by the peak frequency at low temperature (~0 K) is plotted against temperature for the observed lowest frequency peak along with predictions for lowest frequency first sound or fourths sound modes. Clearly, the behavior of the observed peak is not significantly different from a first sound mode. This demonstrates that the observed acoustic signal is not originating from liquid helium that is significantly confined. The first and fourth sound velocities used for making the predictions were obtained from Ref. [30].

3.5.3 Relating Capacitance Change to Mass Flow

Let us first consider the effect of applying an AC voltage on one reservoir (the drive reservoir) and measuring the response on another reservoir (the detect reservoir) of the mass flow chip. The mass flow rate λ out of the drive reservoir due to a change in the density of the superfluid $\delta\rho$ can be approximated to be

$$\lambda = pS\,V_r\delta\rho 2f \tag{3.7}$$

where p is the porosity, S is the superfluid fraction, V_r is the volume of the reservoir, and f is the frequency of the drive voltage. If we assume that the mass exiting the drive

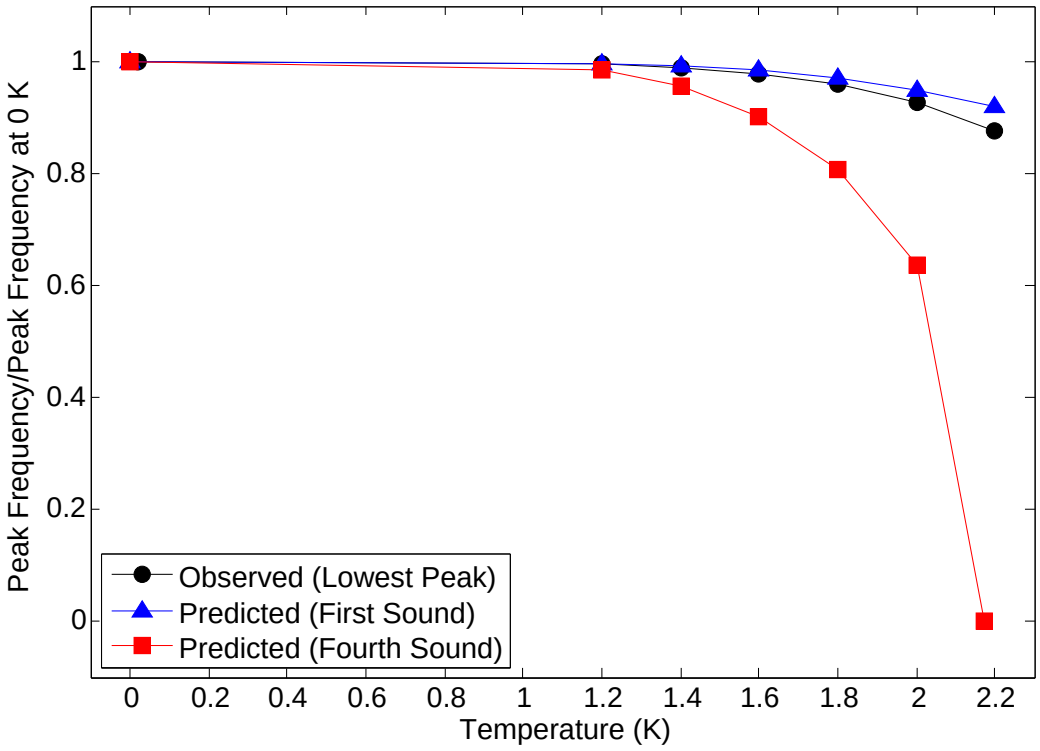

Figure 3.10: Are the observed acoustic peaks due to first sound or fourth sound resonances? The peak frequency normalized by the peak frequency at low temperature is plotted against temperature for the lowest observed mode as well as for the predicted first sound and fourth sound peaks. The behavior of the observed peak is consistent with it being due to a first sound resonance. This indicates that the acoustic signal is originating from liquid helium that is not significantly confined. The first and fourth sound speeds were obtained from Ref. [30].

reservoir enters the detect reservoir, then the mass flow rate should also be given by

$$\lambda = \rho p S A_t v_{flow} \tag{3.8}$$

where A_t is the total cross-sectional area separating the two reservoirs and v_{flow} is the velocity at which the superfluid is flowing. The effective area is the total area reduced by the porosity and the superfluid fraction. Eliminating λ from Equations 3.7 and 3.8 we obtain an expression for the flow velocity

$$v_{flow} = \frac{2 f V_r}{A_t} \frac{\delta\rho}{\rho} \tag{3.9}$$

where ρ is the average density of the superfluid in the reservoirs.

The fractional change in density $\delta\rho/\rho$ needs to be related to the fractional change in capacitance $\delta C/C$. The Clausius-Mossoti relation gives roughly 1/3 change in the capacitance for a unit change in density of simple materials with low dielectric constants. Including the effect of a reduced porosity, a reduced superfluid fraction, and the finite dielectric constant of the porous ceramic material, we get

$$\frac{\delta C}{C} = \frac{pS}{3\epsilon_D^2}\frac{\delta\rho}{\rho} \tag{3.10}$$

Eliminating $\delta\rho/\rho$ from Equations 3.9 and 3.10, we get

$$v_{flow} = \frac{6fV_r\epsilon_D^2}{A_t pS}\frac{\delta C}{C} \tag{3.11}$$

The mass current density J can be related to the mass flow rate λ and the flow velocity v_{flow} as

$$J = \frac{\lambda}{A_t} = \rho pS\, v_{flow} \tag{3.12}$$

Eliminating v_{flow} from Equations 3.11 and 3.13, we get

$$J = \frac{6fV_r\epsilon_D^2\rho}{A_t}\frac{\Delta C}{C} \tag{3.13}$$

3.5.4 Model Dependent Limits on Mass Flow

When the reservoirs are filled with solid ^{4}He as described in Section 3.4.2, the acoustic peaks disappear. We find no evidence for any acoustic peaks above our noise floor in the range of 200 Hz to 10 kHz. The lowest frequency superfluid peak and the noise floor when the reservoirs are filled with solid are shown in Figure 3.11. We can now compare the mass flow observed in the superfluid to the noise floor in the solid case to place limits on the superfluid fraction that can exist in the solid. The question of what should happen to the acoustic peaks if solid ^{4}He did indeed contain a superfluid component depends

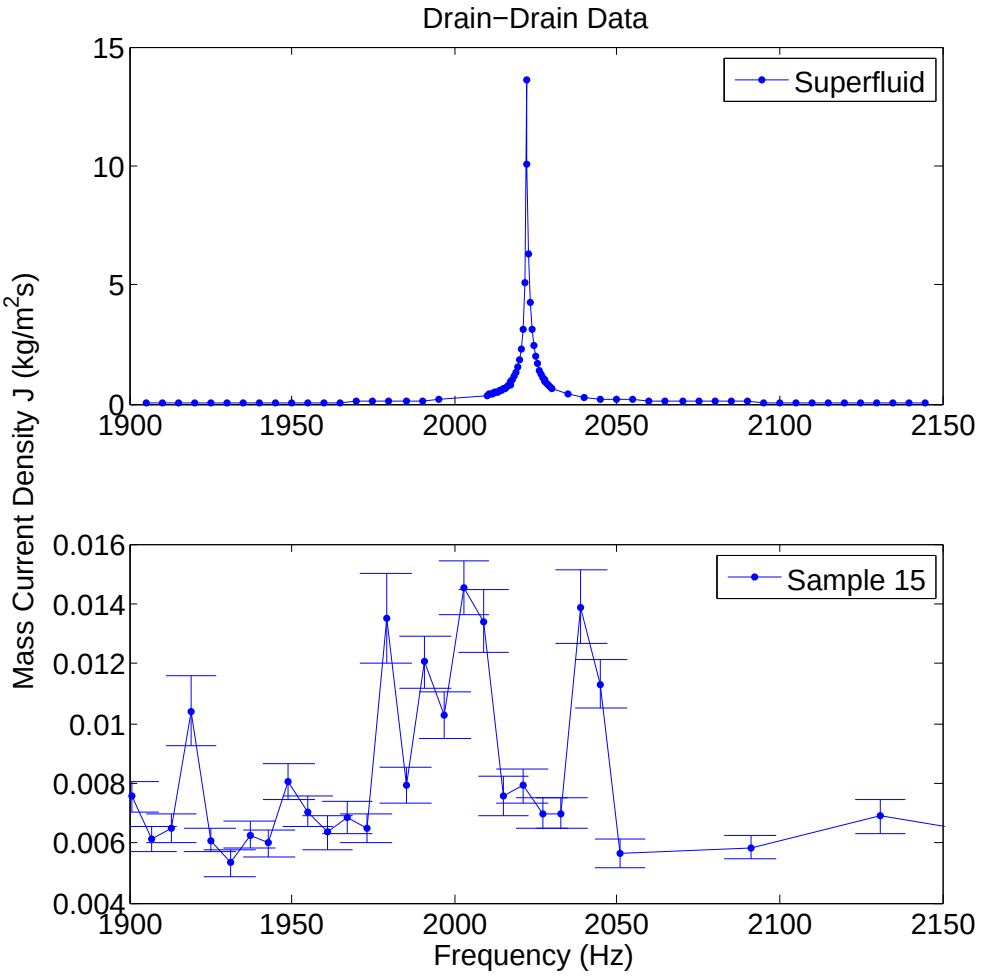

Figure 3.11: **(A)** The acoustic peak observed when the reservoirs are filled with superfluid at 6 bar. **(B)** When the reservoirs are filled with solid ^{4}He, the acoustic peak disappears. The measured noise floor lets us put an upper limit on the mass current density in the solid.

on the supersolid model one considers. We will consider two models of supersolidity in the following discussion. The first is a solid which contains an interconnected network of superfluid channels. The second is a solid with a homogeneous superfluid density. We then make reasonable assumptions for each model to place limits on the superfluid fraction that can exist within such a solid.

Before we consider the two simplified models of supersolidity, we can first use Equa-

tion 3.11 to estimate the flow velocity in the superfluid case. We use the following values for the various parameters: $f = 2022$ Hz, $V_r = \pi(r_o^2 - r_i^2)d = 1.3 \times 10^{-8}$ m^3, where $r_o = 0.86$ in is the outer radius of the ring, $r_i = 0.6$ in is the inner radius of the ring electrode, and $d = 17$ microns is the thickness of the reservoirs, $\epsilon_D = 4$ is the dielectric constant of the ceramic tape, $A_t = 2\pi r_c d = 1.5 \times 10^{-6}$ m^2, where $r_c = 0.55$ in is the radius of the center electrode, $p = 1/3$, $S = 1$, and $\Delta C/C = 13.63$ ppm. Substituting these values in Equation 3.11, we get $v_{flow} = 69$ mm/s.

We first consider the model where the solid contains an interconnected network of superfluid channels. As far as the equations for mass flow are concerned, the effect of filling the reservoirs with such a solid is equivalent to reducing the porosity of the reservoirs and filling them with superfluid. We use Equation 3.11 to note that

$$\frac{\Delta C}{C} \propto pS\, v_{flow} \tag{3.14}$$

This means that a smaller observed $\Delta C/C$ when the reservoirs are filled with solid could result either due to a lower superfluid fraction S, a lower effective porosity p as discussed, or a decreased allowed flow velocity v_{flow}. Within this model, however, we can either let the porosity or the superfluid fraction decrease but not both. In other words, we can think of the channels as contributing to a lower porosity but containing within them superfluid of fraction 1 or we can keep the porosity unchanged and think of the channels as contributing to a reduced superfluid fraction within the solid. We choose the latter alternative - we keep the porosity unchanged and let the superfluid fraction S vary. Within this model, we expect the frequency of the acoustic mode to remain unchanged with a reduction in the superfluid fraction. Only the amplitude of the peak is assumed to change. Furthermore, we assume that there might be a critical velocity for the solid such that superfluid can only flow at or below this velocity regardless of how strongly the flow is driven. This provides the rationale for the construction of an exclusion diagram. On the X-axis of such a diagram is plotted the superfluid fraction S ranging from

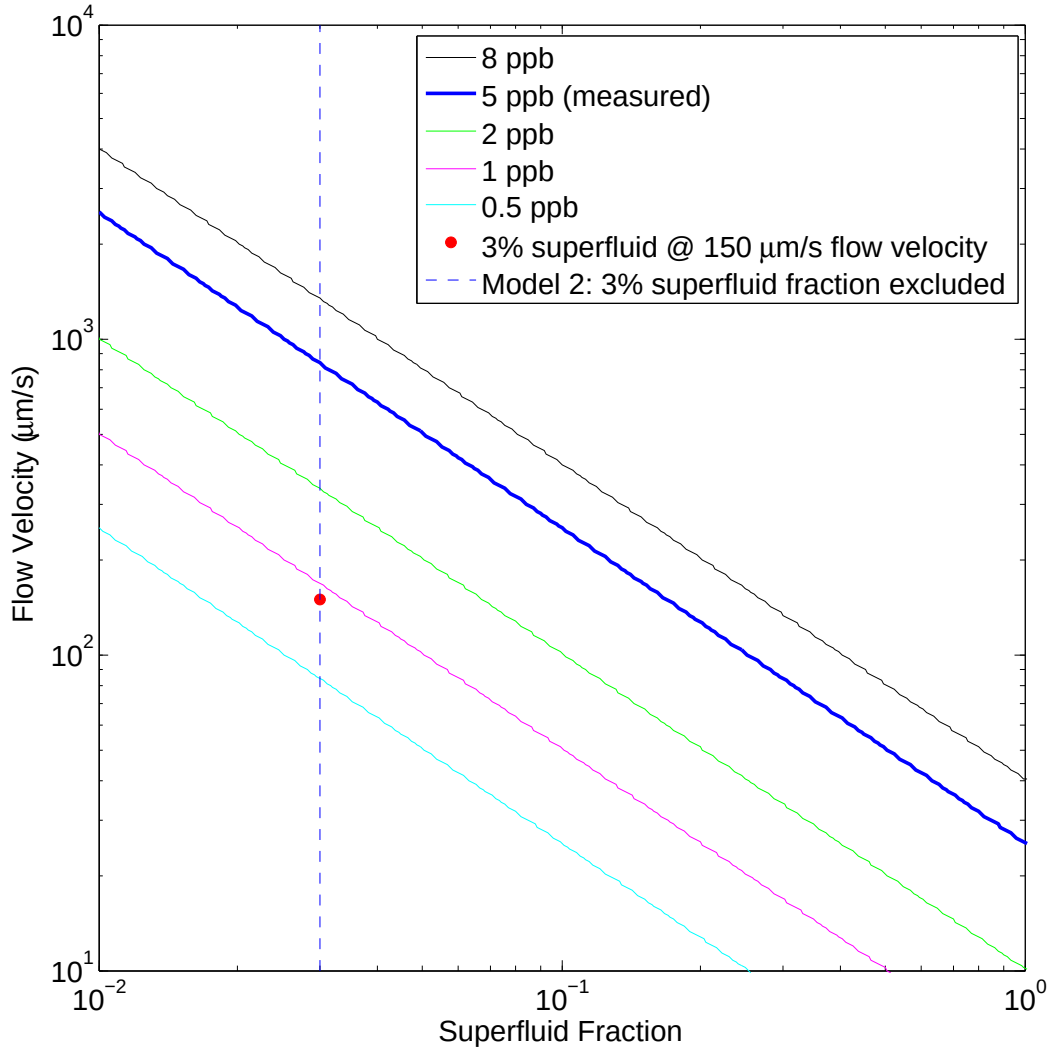

Figure 3.12: The acoustic peak vanishes when the reservoirs are filled with solid ^{4}He. This could be because the superfluid fraction in the solid is lower or because the maximum flow velocity in the solid is lower. Using Equation 6, we can see that the noise floor in the fractional change in capacitance can be used to put a limit on the superfluid fraction if the flow velocity is known. Since the flow velocity is not known, however, we can construct a plot in which the flow velocity and the superfluid fraction are the two independent axes and the measured noise floor is shown as a contour. The contour splits the parameter space into two parts, excluding the region above the line. Several contours corresponding to different noise floors are shown including the measured contour (thick blue line). The red dot corresponds to 3% superfluid fraction and 150 μm/s flow velocity. The dotted line indicates that 3% superfluid fraction is excluded in the second supersolid model discussed in text.

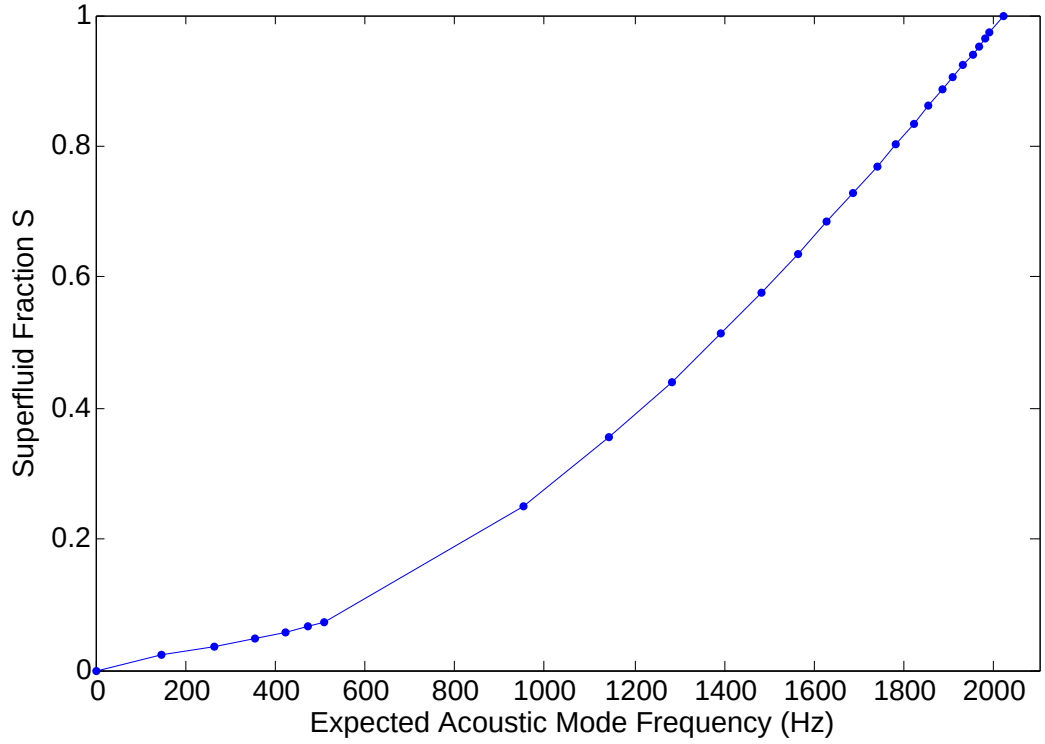

Figure 3.13: Dependence of expected acoustic mode frequency on the superfluid fraction S in the homogeneous supersolid of model 2. Given that the acoustic peak occurred at 2022 Hz in the superfluid ($S = 1$), we can predict the peak frequency as a function of superfluid fraction by noting that its dependence is the same as that of fourth sound velocity for a superfluid. Data for the fourth sound velocity as a function of superfluid fraction obtained from Ref. [30]

0 to 1, and on the Y-axis is plotted the hypothetical critical velocity v_{flow} ranging from 0 to 69 mm/s. The observed noise floor in the solid case for $\Delta C/C$ is $\sim$ 5 ppb which gives the ratio to be 2726. Such an exclusion plot is shown in Figure 3.12. The observed noise floor is now a contour on this plot (dark blue line) which splits the parameter space into two regions - the excluded region is above the line.

We now consider the second model of supersolidity in which the solid is assumed to contain a homogeneously interpenetrating superfluid component. This is very much like the two-fluid model of liquid ^{4}He in which the liquid is though of as composed of a normal fluid component and a superfluid component, except that the normal fluid is now

replaced with a solid. In contrast to the previous model, we do expect the frequency of the acoustic resonance to decrease (as a result of the decrease in sound velocity) as the superfluid fraction is lowered. This is analogous to the observed decrease in fourth sound velocity when the superfluid fraction of liquid helium is decreased, as happens with increasing temperature.

Figure 3.13 shows the dependence of the expected acoustic mode frequency on superfluid fraction S (given that the acoustic mode occurred at 2022 Hz for $S = 1$). This plot was constructed by scaling the acoustic mode frequency with normalized fourth sound velocity as a function of superfluid fraction (data from Ref. [30]). We have shown that no acoustic peaks exist with a noise floor of 5 ppb down to 200 Hz. From Figure 3.13, we see that 200 Hz corresponds to 3% superfluid fraction. Hence, we cannot exclude superfluid fractions below 3% within this second model of supersolidity. This is indicated by a dashed line in Figure 3.12, which is the complete exclusion plot for both simplified models of supersolidity considered here.

3.6 Conclusions and Suggestions for Improvement of the Design

Day and Beamish [27] and Rittner *et al.* [73] found no mass flow when they used a piezoelectrically driven diaphragm to press on solid ^{4}He. In their experiments, the pressure was applied by changing the boundary conditions of a bulk slab of solid ^{4}He, attempting to squeeze out liquid by pressing on the lattice. Here we report a new apparatus for detecting mass flow where the pressure is applied electrostatically throughout the sample by enclosing a reservoir of helium between two plates of a capacitor. Mass flow can be detected by monitoring the capacitance of a second reservoir connected to the first by a set of tubes. We first establish a mass flow detection scheme by measur-

ing acoustic resonances when the apparatus is filled with superfluid ^{4}He. This acoustic resonance technique provides an opportunity to search for AC mass flow in the kilohertz range, which is comparable to torsional oscillator frequencies. We find that when the apparatus is filled with solid ^{4}He, the acoustic peaks, and hence mass flow, can no longer be observed. This allows us to construct a a plot of flow velocity versus superfluid fraction and exclude a region on it based on our signal to noise.

We now suggest some improvements to the design of the mass flow chip that will enable more stringent limits to be set:

1. Pore size: The pores were probably too big to support superfluid at reasonable overpressures ($\sim$ 1 bar). The ceramic tape needs to be fired at temperatures higher than 1000 C and tested.
2. Bulk gaps: The gold electrodes on the center macor plate was pressed against but not sealed to the porous reservoirs. This could lead to bulk gaps existing between the porous reservoirs and the center plate electrodes.
3. Cross talk: We had to develop a scheme to deal with significant cross talk between the source and drain capacitors and also the two drain capacitors. This cross talk adversely affected our signal to noise ratio. The capacitors need to be better shielded to eliminate or substantially reduce cross talk.
4. Macor: We found that working with macor was not easy and led to problems with electrode deposition and ceramic tape lamination. We recommend using silicon (Si) wafers instead.

CHAPTER 4

A DISLOCATION MODEL FOR THE ORIGIN OF THE INERTIAL ANOMALY

We[1] argue in chapters 2 and 3 that the Kim and Chan effect [44, 45] is unlikely to be caused by solid ^{4}He entering a supersolid state. If it is not supersolidity, then what is the mechanism underlying the observed phenomena? In this chapter, we develop a model based on dislocation dynamics to explain the observed frequency shift and dissipation in torsional oscillator experiments.

4.1 Introduction

As discussed in Chapter 1, the Kim and Chan effect [44, 45] was originally interpreted as evidence for a supersolid state. This was primarily because the increase in resonant frequency of a torsional oscillator (TO) at low temperature was thought to be due to a decrease in the moment of inertia caused by mass decoupling. Indeed, The strongest evidence for this view came from the blocked annulus experiment [44] where the Kim and Chan signal was almost completely eliminated when the continuity of the annulus was blocked. However, a host of subsequently discovered phenomena (see Section 2.1), all seemed inconsistent with this view.

One of the most important clues to the problem was discovered by Day and Beamish [28] when they demonstrated that solid ^{4}He becomes stiffer (the shear modulus μ increases) as the temperature is lowered (see Section 1.4.3). This was unexpected in the supersolid picture because one would expect a supersolid (which is more like a liquid) to be easier to shear, not harder. The dependence of μ on temperature exactly matched

[1] The work described in this chapter was done in collaboration with E. Kassner, E. J. Pratt, J. P. Sethna, and J. C. Davis.

that of the non-classical rotational inertia (NCRI), a measure of the fraction of mass thought to be decoupled from the torsional oscillator reported by Kim and Chan (see Figure 1.8). Furthermore, the shear modulus experiments showed the same dissipation peak, dependence on ^{3}He concentration and frequency dependence [28]. It was apparent that the increase in shear modulus and the Kim and Chan effect were intimately related.

We demonstrate in Chapter 2 that there is no evidence for a superfluid-like transition in the microscopic relaxation time anywhere in the temperature or velocity range of interest for the Kim and Chan effect. In addition, we further expose the connection between the shear modulus stiffening and the TO frequency shift (see Figure 2.7). Specifically, we show that the combined temperature-velocity dependence of the TO response mirrors quantitatively the combined temperature-strain dependence of the shear modulus. These observations imply strongly that the rotational dynamics of solid ^{4}He are closely associated with the generation (presumably by inertial shearing) of the same type of microscopic excitations which are generated by direct shear strain ε.

What, then is the microscopic explanation for the shear stiffening effect? Day and Beamish [28] immediately realized that the observed increase in the shear modulus is consistent with the dynamics of dislocations within solid ^{4}He. Dislocations are one dimensional defects that can form a network in solid ^{4}He. Dislocation segments can be thought of as strings that can move under applies stress and contribute to the strain. In this way, their motion can result in a decrease in the shear modulus. ^{3}He atoms can pin dislocations and prevent their motion. Interestingly ^{3}He impurity atoms can be unpinned from dislocation segments by increasing the temperature as well as by applying stress. Furthermore, the motion of dislocation segments through the atmosphere of ^{3}He atoms can cause dissipation. It appears that dislocation dynamics have several of the elements that are required to explain the shear stiffening result. Can they be used to explain the

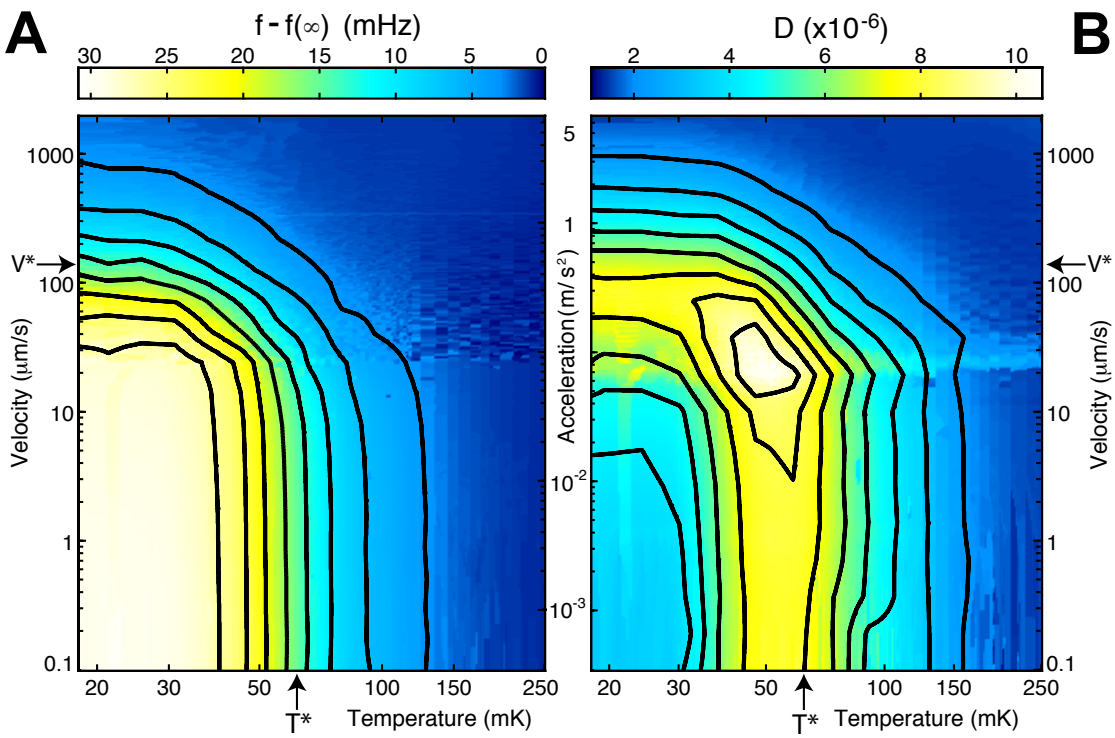

Figure 4.1: (A) TO resonant frequency shift $f - f_\infty$ and **(B)** dissipation D data mapped throughout the $V - T$ plane (Figure 2.4 reproduced here for convenience). Can a model based on dislocation dynamics explain these data?

torsional oscillator results as well?

Iwasa [40, 41] has proposed a dislocation-vibration model to explain both the shear modulus and torsional oscillator results. The goal of this chapter is to extend Iwasa's model in an attempt to explain the observed frequency shift and dissipation over the entire velocity-temperature plane (Figure 4.1). In section 4.2, we introduce dislocations and Iwasa's model for the temperature dependence of the frequency shift and dissipation. In section 4.3, we deviate from Iwasa's treatment for the amplitude dependence and extend his model to capture the velocity or acceleration dependence (the Y-axis in Figure 4.1). Finally, we examine how well the model agrees with the data in section 4.4.

4.2 Iwasa's Dislocation-Vibration Model

The following discussion is based on Iwasa's dislocation vibration model [40, 41]. We first introduce dislocations and present Iwasa's main results for the temperature dependence of the torsional oscillator period shift and dissipation. We then provide the key steps in the derivation of some of his equations.

4.2.1 Dislocations and Iwasa's Principal Results

Dislocations are linear lattice defects characterized by the direction vector l and Burgers vector b. Figure 4.2 shows a schematic of an edge dislocation which can be thought of as being formed due to a missing a half-plane of atoms. It has been known since the 1970s that solid ^{4}He contains dislocations [85, 86] and furthermore that basal dislocations (whose slip plane is the basal plane of the hexagonal crystal) in hcp ^{4}He can vibrate in the megahertz range [92, 38].

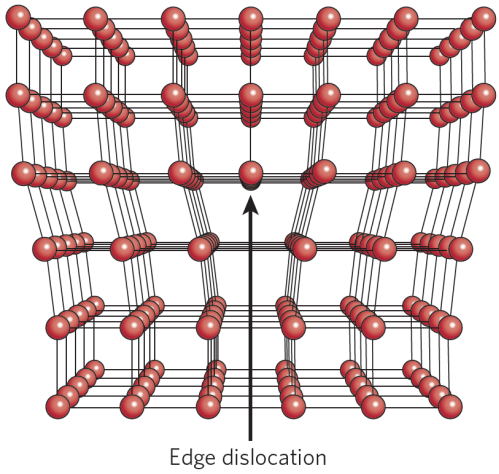

Figure 4.2: Schematic showing an edge dislocation, caused by a missing half-plane of atoms. Image adapted from [12].

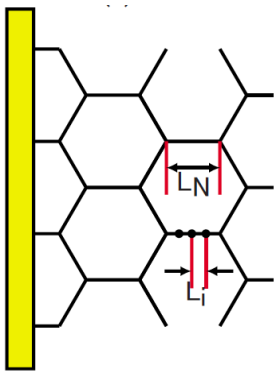

Figure 4.3: Marked on a schematic of a dislocation network are the network pinning length L_N and the impurity pinning length L_i. The nodes of the network are considered strong pinning points that always remain pinned while the ^{3}He atoms pin the dislocation segments at weak pinning points and can be unpinned with increasing temperature. Image adapted from [40].

Dislocation lines in a crystal can intersect to form a three-dimensional network (Figure 4.3). These points of intersection, or nodes of the network, are strong pinning points and are separated by L_N, the average network pinning length. In addition, dislocation segments can be weakly pinned by ^{3}He atoms with the average impurity pinning length L_i. The average pinning length between any two pinning point is thus given by

$$L = \frac{L_N L_i}{L_N + L_i}. \tag{4.1}$$

Iwasa [40] relates the period shift of a torsional oscillator containing solid ^{4}He to the length of the dislocation segments within the solid. The proposed mechanism is that the vibration of dislocation segments increases the wave number of the shear wave inside the solid, which in turn causes the apparent moment of inertia of the TO to increase. Iwasa's result for the period shift can be written as

$$\frac{p_2}{p_1} = \frac{(1-\nu)\Omega\Lambda}{2\pi} L^2 \tag{4.2}$$

where p_2 is the period change due to dislocation motion, p_1 is the period change due to mass loading, ν is Poisson's ratio, Ω is an orientation factor, Λ is the dislocation density, and L is the length of a dislocation segment.

The temperature dependence of the period shift arises from the temperature dependence of the impurity pinning length, given by

$$L_i = g x_3^{-2/3} e^{-2W_0/3T} \tag{4.3}$$

where g is an experimentally determined constant, x_3 is the ^{3}He concentration, and W_0 is the binding energy for a ^{3}He atom to bind to a dislocation segment.

Iwasa [40] also relates the dissipation observed in torsional oscillator studies to the length of dislocation segments. The damping is attributed to the interaction of vibrating dislocation segments with the atmosphere of ^{3}He atoms formed around them. The dissipation due to dislocation motion is given by

$$Q^{-1} = \frac{16\Lambda\Omega\mu_{el}}{\pi^2\rho}\frac{\omega d}{\omega_0(L)^4} \tag{4.4}$$

where μ_{el} is the elastic shear modulus and ρ is the density of solid ^{4}He, ω is the resonance frequency of the torsional oscillator, $\omega_0(L)$ is the resonance frequency of a dislocation segment of length L, and d is a damping parameter. The temperature dependence of the dissipation arises from the length dependence of ω_0,

$$\omega_0(L) = \frac{1}{L}\sqrt{\frac{2\mu_{el}}{(1-\nu)\rho}} \tag{4.5}$$

and the temperature dependence of the d,

$$d = d_0 e^{2W_0/3T} \tag{4.6}$$

where d_0 is a constant.

Iwasa's dislocation-vibration model [40] is able to explain the temperature dependence of the frequency shift and the dissipation at low velocity (or acceleration). To capture the velocity (or acceleration) dependence, Iwasa introduces the idea of a critical dislocation segment length and a distribution of network pinning lengths [41]. This

approach does not explain the velocity (or acceleration) dependence of the dissipation. In the following section, we take a different approach in an attempt to explain our data shown in Figure 4.1.

4.2.2 Derivation of Iwasa's Result for the Period Shift

We now present the key steps in the derivation of Iwasa's result [41] for the period shift of an annular torsional oscillator (TO) containing solid ^{4}He (Equation 4.2). We treat the TO as a rigid body and the solid ^{4}He as an elastic body occupying an annulus of outer radius R_0, inner radius R_1, and height H. We assume that the gap $R_0 - R_1 = 2a$ is much smaller than the average radius $R = (R_0 + R_1)/2$ and the height. We can therefore neglect the torque on the top and bottom plates. In terms of the average radius, we now have $R_0 = R + a$ and $R_1 = R - a$ and the radial position can be written with respect to R as $r = R + x$. The moment of inertia of solid ^{4}He can thus be written as

$$I_{He} = \frac{\pi}{2}(R_0^2 + R_1^2)(R_0^2 - R_1^2)H\rho = 4\pi(R^2 + a^2)RaH\rho \tag{4.7}$$

where ρ is the density of solid ^{4}He. Let ω be the angular frequency of the TO and u_0 its amplitude. When the TO is so driven, the solid ^{4}He sample oscillates in phase with the TO but overshoots causing a back-action torque to be applied to the TO. The TO equation of motion is

$$I_{TO}\frac{d^2\phi}{dt^2} = -\kappa\phi + \tau \tag{4.8}$$

where the angle of rotation is given by

$$\phi = \frac{u_0}{R_0}e^{-i\omega t}, \tag{4.9}$$

the torsional spring constant by κ and the torque by

$$\tau = -2\pi R_0^2 H\sigma(R_0) + 2\pi R_1^2 H\sigma(R_1) \tag{4.10}$$

where σ is stress in solid ^{4}He. The displacement of the TO can be written as

$$u_1(r) = r\phi = (R + x)\phi. \tag{4.11}$$

Elastic shear waves or frequency ω and wave number k are produced by the oscillations. The displacement in solid ^{4}He can be written as a sum of two displacements, $u_1(r)$ and

$$u_2(r) = u_2(x) = \frac{u_0 k^2}{2}(a^2 - x^2)e^{-i\omega t}. \tag{4.12}$$

The total displacement, therefore, is

$$u(x) = u_1(x) + u_2(x) = \left[\frac{u_0(R + x)}{R_0} + \frac{u_0 k^2}{2}(a^2 - x^2)\right]e^{-i\omega t} \tag{4.13}$$

with boundary conditions given by

$$u(a) = u_0 e^{-i\omega t} \tag{4.14a}$$

$$u(-a) = \frac{u_0 R_1}{R_0}e^{-i\omega t}. \tag{4.14b}$$

The stress originates not from $u_1(x)$ (rigid body rotation), but from $u_2(x)$ and is

$$\sigma(x) = \mu\frac{d}{dx}u_2(x) = -\mu u_0 k^2 x e^{-i\omega t}. \tag{4.15}$$

This means that $\sigma(a) = -\mu u_0 k^2 a e^{-i\omega t}$ and $\sigma(-a) = \mu u_0 k^2 a e^{-i\omega t}$ and therefore

$$\tau = 4\pi(R^2 + a^2)H\mu u_0 k^2 a e^{-i\omega t} \approx \frac{\mu k^2}{\rho} I_{He}\phi. \tag{4.16}$$

The equation of motion for an elastic material (with shear stress σ and shear strain ϵ) is

$$\rho\frac{\partial^2 \epsilon}{\partial t^2} = \frac{\partial^2 \sigma}{\partial x^2}. \tag{4.17}$$

By definition we have $\sigma = \mu\epsilon$. Thus, for an elastic wave $\sigma = \sigma_0 e^{i(kx-\omega t)}$, the $\omega - k$ relation can be written as

$$\rho\omega^2 = \mu k^2. \tag{4.18}$$

Combining Equations 4.8, 4.9, 4.16, and 4.18, the period can be written as

$$p = \frac{2\pi}{\omega} = 2\pi\sqrt{\frac{I_{TO} + I_{He}}{\kappa}} \tag{4.19}$$

which is the same result we would have obtained if we had written the total moment of inertia as

$$I_{tot} = I_{TO} + I_{He}. \tag{4.20}$$

How do dislocations affect the above analysis? In the presence of dislocations, the total strain can be written as a sum of the elastic strain and the dislocation strain

$$\epsilon = \epsilon_{el} + \epsilon_{dis} \tag{4.21}$$

where the elastic part can be related to the shear stress

$$\epsilon_{el} = \frac{\sigma}{\mu_{el}} \tag{4.22}$$

if μ_{el} is the elastic shear modulus (without the effect of dislocations). Let the shear wave created in solid ^{4}He with dislocations have frequency ω and wave number k'. The dislocation part of the strain can be written as

$$\epsilon_{dis} = \frac{\Omega\Lambda\sigma}{\pi\rho\omega_0^2} \tag{4.23}$$

where Ω is an orientation factor, Λ is the dislocation density. ω_0 is the resonance frequency of a dislocation segment of length L, given by

$$\omega_0 = \frac{1}{L}\sqrt{\frac{2\mu_{el}}{(1-\nu)\rho}} \tag{4.24}$$

where ν is Poisson's ratio. Equation 4.23 can now be written as

$$\epsilon_{dis} = \frac{(1-\nu)\Omega\Lambda L^2}{2\pi}\epsilon_{el}. \tag{4.25}$$

With dislocations, the equation of motion is modified to

$$\rho\frac{\partial^2}{\partial t^2}(\epsilon_{el} + \epsilon_{dis}) = \frac{\partial^2\sigma}{\partial x^2} \tag{4.26}$$

and the $\omega - k'$ relation becomes

$$\rho\omega^2\left(1 + \frac{(1-\nu)\Omega\Lambda L^2}{2\pi}\right) = \mu_{el}k'^2. \tag{4.27}$$

Like the strain, the displacement can also be considered a sum of two parts (elastic and dislocation)

$$u(x) = u_{el}(x) + u_{dis}(x). \tag{4.28}$$

Pinning of dislocations at the TO walls gives us

$$u_{dis}(a) = u_{dis}(-a) = 0 \tag{4.29}$$

and so we have

$$u_{el}(x) = \left[\frac{u_0(R+x)}{R_0} + \frac{u_0 k'^2}{2}(a^2 - x^2)\right] e^{-i\omega t} \tag{4.30}$$

and

$$u_{dis}(x) = \frac{(1-\nu)\Omega\Lambda L^2}{2\pi}\frac{u_0 k'^2}{2}(a^2 - x^2)e^{-i\omega t}. \tag{4.31}$$

Since the force exerted by the dislocations on the walls is small, the stress due to the elastic part of the strain is

$$\sigma(x) = -\mu_{el} u_0 k'^2 x e^{-i\omega t} \tag{4.32}$$

while the torque due to solid ^{4}He is

$$\tau = 4\pi(R^2 + a^2)H\mu_{el}u_0 k'^2 a e^{-i\omega t} \approx \frac{\mu k'^2}{\rho} I_{He}\phi. \tag{4.33}$$

Equation 4.27 in Equation 4.33 gives us

$$\tau = \omega^2\left(1 + \frac{(1-\nu)\Omega\Lambda L^2}{2\pi}\right) I_{He}\phi \tag{4.34}$$

which when substituted in Equation 4.8 produces

$$p = 2\pi\sqrt{\frac{I_{TO} + I_{He}\left(1 + \frac{(1-\nu)\Omega\Lambda L^2}{2\pi}\right)}{\kappa}} \approx p_0 + p_1 + p_2 \tag{4.35}$$

where $p_0 = 2\pi\sqrt{I_{TO}/K}$ represents the period of the empty TO, $p_1 = (I_{He}/2I_{TO})p_0$ is the change in period when ^{4}He is added to the cell (mass loading), and p_2 is the period shift caused by dislocations. We may now finally arrive at Equation 4.2

$$\frac{p_2}{p_1} = \frac{(1-\nu)\Omega\Lambda L^2}{2\pi} \tag{4.36}$$

4.2.3 Derivation of Temperature Dependence of the Pinning Length

We now derive [41] the temperature dependence of the impurity pinning length L_i (Equation 4.3).

Since ^{3}He impurity atoms move in an hcp ^{4}He crystal without thermal excitation due to quantum tunneling, the pinning rate for the impurity atoms on a dislocation segment of length L_N is assumed to be independent of temperature and given by

$$R_1 = L_N x_3^n A \tag{4.37}$$

where A is a temperature-independent constant. $n = 1$ for straight dislocations and $n = 2/3$ for zigzag configurations. The unpinning rate, however, is considered to due to thermal activation and is given by

$$R_2 = \frac{N}{\alpha_0} e^{-W/T} \tag{4.38}$$

where N is the number of ^{3}He atoms pinning the dislocation segment, and α_0 and W are temperature-independent constants. The rate equation for the number of impurities pinning a dislocation segment is therefore given by

$$\frac{dN}{dt} = R_1 - R_2 = L_N x_3^n A - \frac{N}{\alpha_0} e^{-W/T} \tag{4.39}$$

with the equilibrium value ($dN/dt = 0$) given by

$$N_0 = L_N x_3^n A \alpha_0 e^{W/T} = L_N x_3^n A \alpha, \tag{4.40}$$

where the time constant is given by α

$$\alpha = \alpha_0 e^{W/T}. \tag{4.41}$$

Equation 4.39 has the solution

$$N = L_N x_3^n A \alpha (1 - e^{-t/\alpha}). \tag{4.42}$$

The average impurity pinning length can now be written as

$$L_i = \frac{L_N}{N_0} = \frac{1}{x_3^n A \alpha_0} e^{-W/T}, \tag{4.43}$$

which can be written as displayed before (Equation 4.3)

$$L_i = g x_3^{-2/3} e^{-2W_0/3T}. \tag{4.44}$$

4.3 Capturing the Acceleration (or Velocity) Dependence

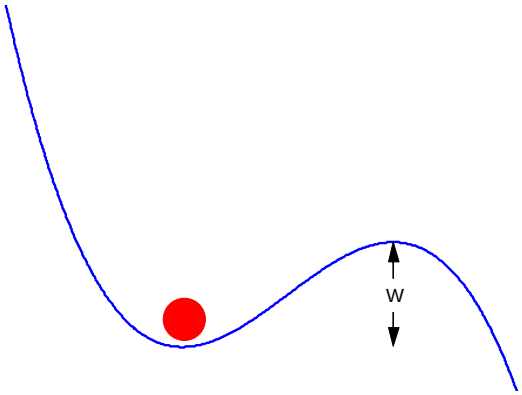

Figure 4.4: Modeling the binding energy with which a ^{3}He atom (red ball) is bound to a dislocation line. The potential (blue line) is assumed to be quadratic with a cubic drop off. If a constant force is applied to the ^{3}He atom, a linear term is introduced to the potential (see text).

To capture the acceleration (or velocity) dependence of the period shift and dissipation, we make the ansatz that the binding energy of ^{3}He atoms on dislocation lines, W depends on acceleration (or velocity). This idea is motivated in Figure 4.4. Consider a ^{3}He atom (depicted by a red ball) in a finite potential well with binding energy W. For simplicity, we assume a quadratic potential well with a cubic cut off. If a constant force F is applied on the ^{3}He atom, the binding energy decreases, given by

$$W = W_0(1 - \gamma F)^{3/2} \tag{4.45}$$

where γ is a constant and W_0 is the binding energy when $F = 0$. Such a force is indeed applied on the ^{3}He atoms when the solid ^{4}He sample is stressed (during the oscillation cycle of a torsional oscillator). If a dislocation segment of length L is subjected to a shear stress σ, the force on a pinning point [41] is given by

$$F = Lb\sigma \tag{4.46}$$

where b is the Burgers vector. Since the shear stress is proportional to the acceleration of the torsional oscillator [41], we can write

$$W = W_0(1 - caL)^{3/2} \tag{4.47}$$

where c is a constant and a is the acceleration of the torsional oscillator.

What is the consequence of making the binding energy dependent on the acceleration (or velocity) and the length of the dislocation segments? The binding energy appears in two places in Iwasa's equations - in the impurity pinning length L_i (Equation 4.3) and the damping parameter d (Equation 4.49). The impurity pinning length now becomes

$$L_i = g x_3^{-2/3} e^{-\frac{2W_0}{3T}\left(1 - ca\frac{L_N L_i}{L_N + L_i}\right)} \tag{4.48}$$

and needs to be solved self-consistently since L_i depends on itself. The damping parameter also changes to

$$d = d_0 e^{\frac{2W_0}{3T}\left(1 - ca\frac{L_N L_i}{L_N + L_i}\right)}. \tag{4.49}$$

Owing to the nature of the equations, varying acceleration (or velocity) now has a similar effect to varying temperature. However, the variation of L as a function of acceleration is very sharp (especially at low temperatures). To capture the gradual change in L, we need to introduce the concept of a distribution of network pinning lengths. There is no reason to assume that every dislocation segment in the network is of the same

length L_N [41]. For simplicity, we assume that the network pinning lengths follow an exponential distribution function, give by

$$N(l) = \frac{\Lambda}{L_A^2} \exp\left[-\frac{l}{L_A}\right] \tag{4.50}$$

where $N(l)dl$ is the number of dislocation segments (per unit volume) that have network pinning lengths between l and $l + dl$ and L_A the average network pinning length. The period shift and dissipation can now be written as

$$\frac{p_2}{p_1} = \frac{(1-\nu)\Omega}{2\pi} \int_0^\infty L^2 l N(l) dl \tag{4.51}$$

and

$$Q^{-1} = \frac{16\Omega\mu_{el}}{\pi^2\rho} \int_0^\infty \frac{\omega d \cdot l}{\omega_0 (L)^4} N(l) dl \tag{4.52}$$

We are almost ready to fit the model to our data. We first note that since the orientation factor Ω cannot be independently determined, we group it with the dislocation density Λ and write the effective density as Λ_e. Secondly, since the equations are in terms of period shift and our data is presented in terms of frequency shift, we note that the conversion between the two is given by

$$f - f_\infty = f_0 - f_1 \frac{p_2}{p_1} \tag{4.53}$$

where f is the frequency, f_∞ is the frequency at high temperature, f_0 is the frequency at low temperature or low acceleration (or velocity), and f_1 is the frequency change due to mass loading. In the following section, we present the fits and discuss how well the model does in explaining our data.

4.4 Fitting the New Model to Data

Equations 4.50 and 4.52 are now fit to our data shown in Figure 4.1. The fitting strategy followed was to first determine the fit parameters from combined fits of $f(T)|_{a\to 0}$ (Fig-

ure 4.5), $f(a)|_{T\to 0}$ (Figure 4.6), $D(T)|_{a\to 0}$ (Figure 4.7), and $D(a)|_{50\,\mathrm{mK}}$ (Figure 4.8). The contour plots (Figures 4.9 and 4.10) were then generated using these fit parameters.

The four fit parameters (with the fit values given in brackets) are the (1) effective dislocation density Λ_e [1.8×10^{12} m^{-2}], (2) the average network pinning length L_A [2×10^{-7} m], (3) the constant relating the force on a ^{3}He atom to the acceleration and segment length c [1.54×10^6 kg/m], and (4) the damping constant d_0 [3.6×10^8 s^{-1}]. The rest of the parameters are either experimental parameters or are taken from published data [41]. The values of these parameters used in this study are: $\nu = 0.3$, $\mu_{el} = 1.5 \times 10^7$ Pa, $x_3 = 300 \times 10^{-9}$ (300 ppb), $\rho = 200$ kg/m^3, $W_0 = 0.3$ K, $\omega = 2\pi \times 574.433$ rad/s, $g = 3.4 \times 10^{-9}$ m, $f_1 = 585$ mHz, and $f_0 = 27.8$ mHz.

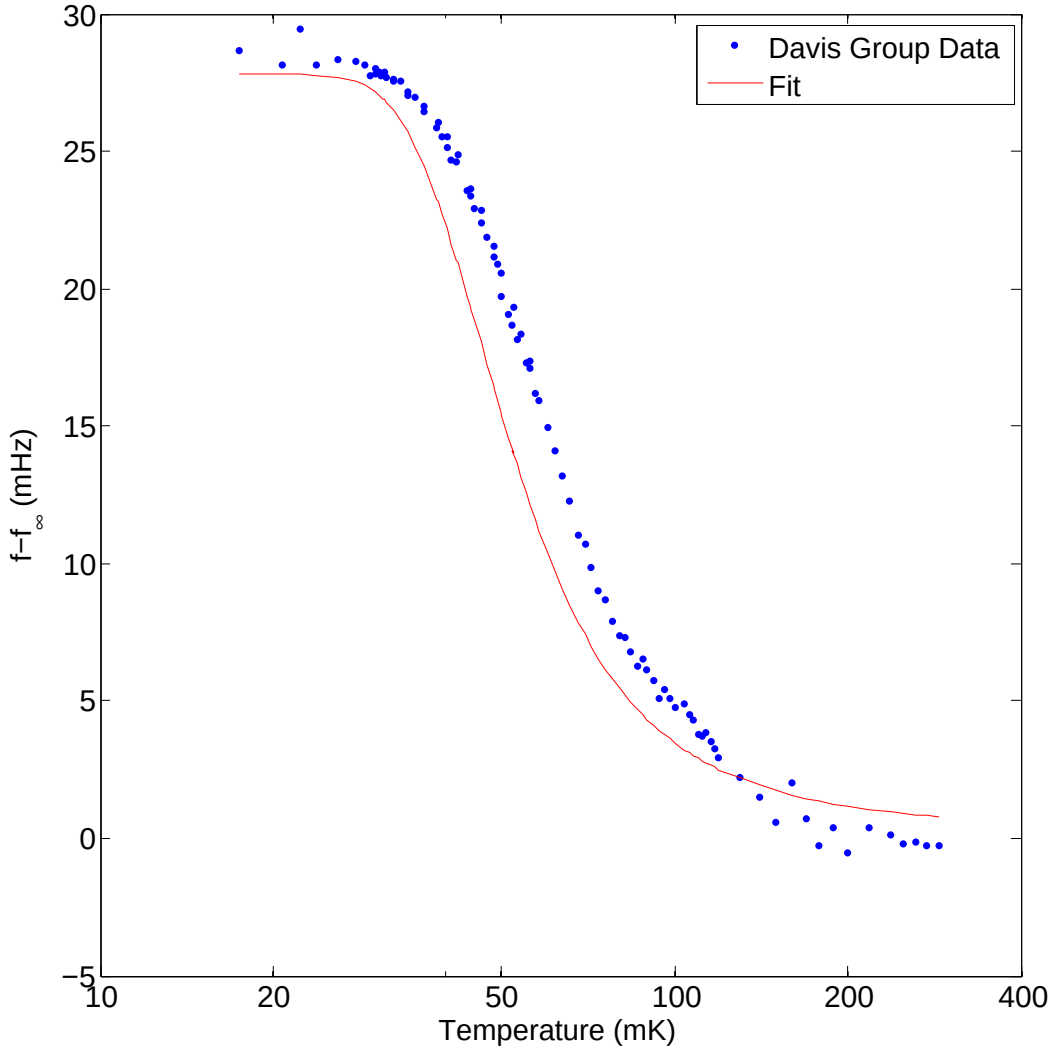

Figure 4.5: Frequency shift as a function of temperature at low acceleration ($a \sim 3.7 \times 10^{-4}$ ms^{-2}).

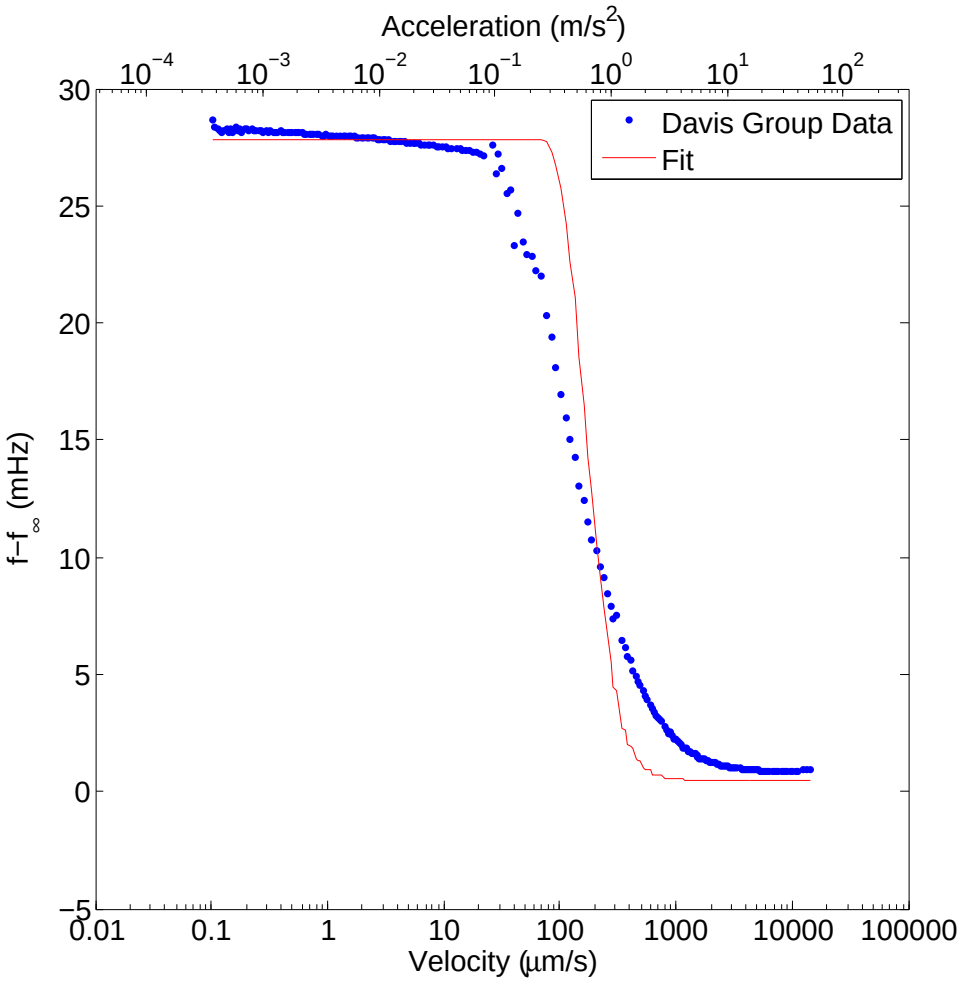

Figure 4.6: Frequency shift as a function of acceleration at low temperature ($T \sim 17.5$ mK).

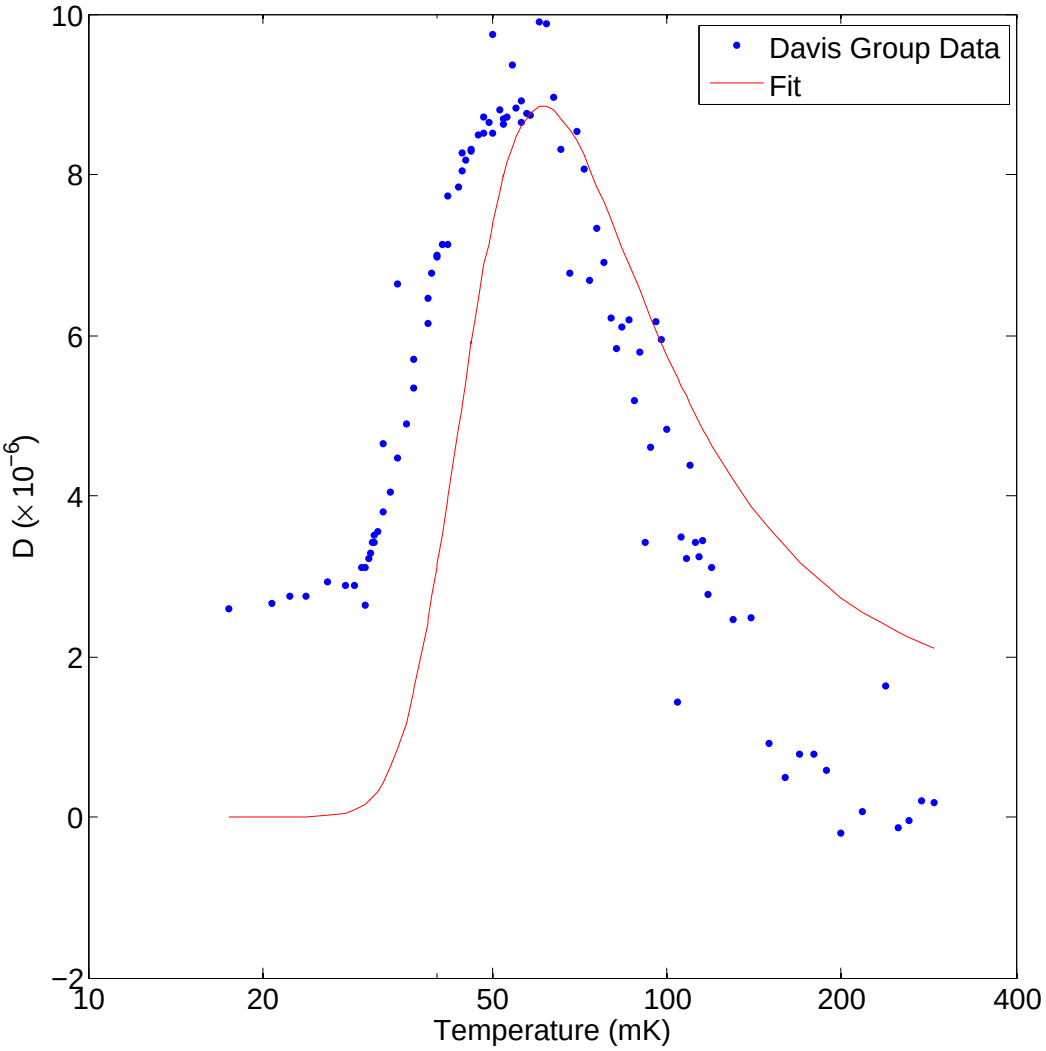

Figure 4.7: Dissipation as a function of temperature at low acceleration ($a \sim 3.7 \times 10^{-4}$ ms^{-2}).

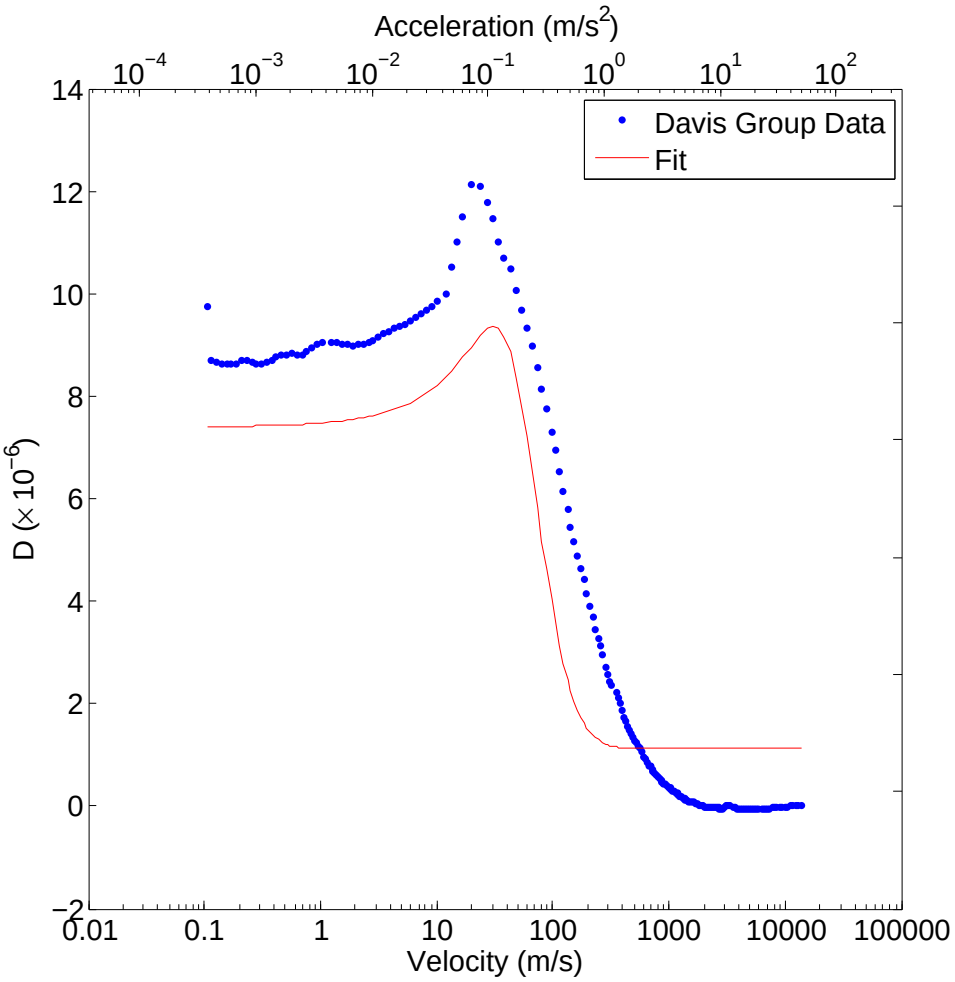

Figure 4.8: Dissipation as a function of acceleration at 50 mK.

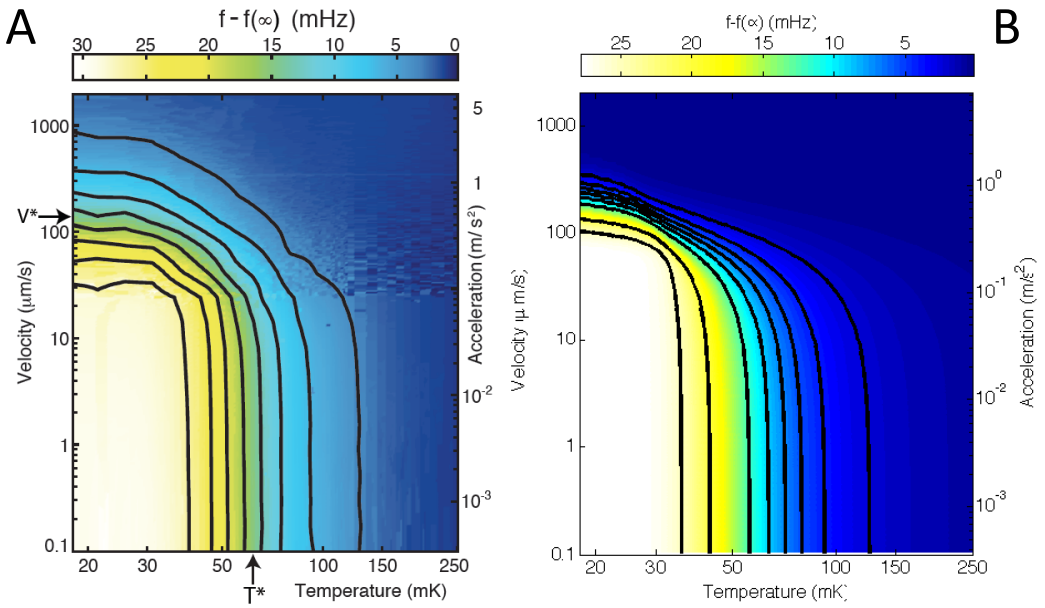

Figure 4.9: Data **(A)** and model fit **(B)** of the TO resonant frequency shift $f - f_\infty$ throughout the $a - T$ plane.

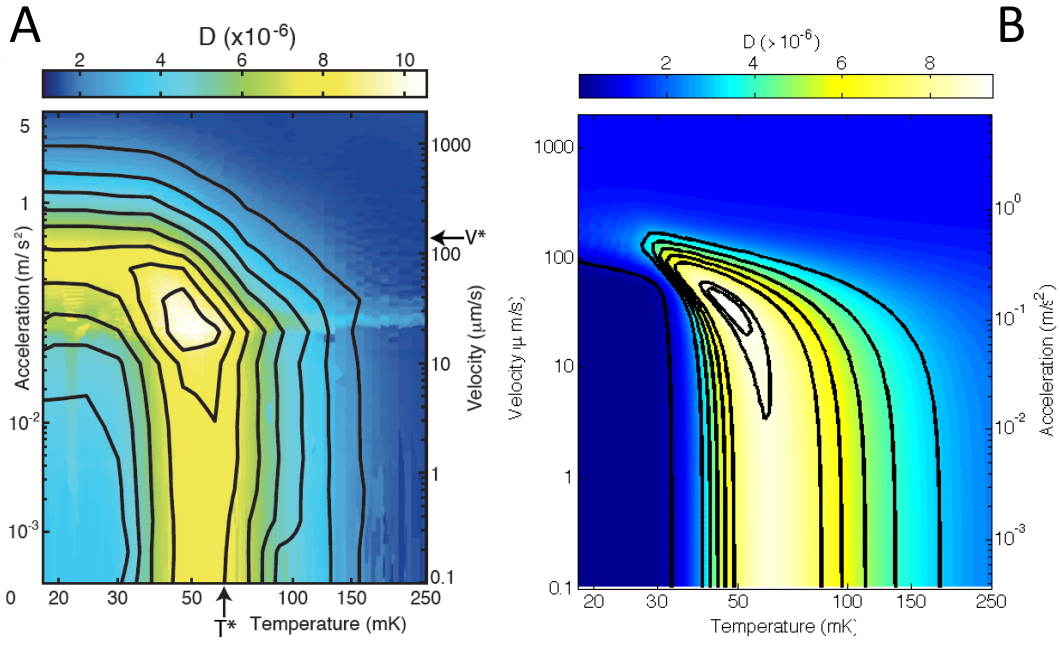

Figure 4.10: Data **(A)** and model fit **(B)** of the TO dissipation D throughout the $a - T$ plane.

Figure 4.5 shows data and the model fit for the frequency shift as a function of temperature for low acceleration ($a \sim 3.7 \times 10^{-4}$ ms^{-2}). The fit looks good except that is slightly shifted to lower temperatures. The fit for the dissipation as a function of temperature at low acceleration (Figure 4.7) is similarly good but is slightly shifted to higher temperatures. In other words, in the low acceleration data, the dissipation peak and the maximum rate of change of frequency shift occur at the same temperature but are slightly shifted in the model. The other feature immediately obvious in Figure 4.7 is that the dissipation goes to zero at low T in the model but not so in the data. We will return to the issue of low temperature dissipation below.

Figure 4.6 shows data and the model fit for the frequency shift versus acceleration at low temperature ($T \sim 17.5$ mK). While the model captures the overall trend of the data, it predicts a sharper change in the frequency shift than what is observed. This sharpness is controlled by the distribution function of the network pinning lengths. In other words, the overly sharp transition from high frequency to low frequency can be thought of as a shortcoming of the exponential distribution function, which was chosen for its simplicity. We have preliminary evidence that a power law distribution function is better able to capture the slope of the data and will be fully explored in a future iteration of this work.

Figure 4.8 shows the dissipation as a function of acceleration at 50 mK. The model is able to capture most of the gross features of the data. One difference is that the dissipation does not go to zero at high acceleration in the model while it does in the data. The other is that the model predicts a smaller magnitude of dissipation than observed. In fact, the reason we do not fit $D(a)$ at low T is because the model predicts much smaller dissipation at low temperatures than the data.

Figure 4.9 shows the data **(A)** and model fit **(B)** for the frequency shift over the entire

acceleration-temperature plane. The model fits the temperature dependence very well and captures all the gross features of the data. The only limitation is the sharpness of the frequency change along the acceleration axis. As discussed above, this aspect of the fit is likely to be vastly improved with a better choice of distribution function (such as a power law).

Finally, Figure 4.10 shows the data **(A)** and model fit **(B)** for the dissipation over the entire acceleration-temperature plane. Once again the model fits the temperature dependence very well except at lowest temperatures. The acceleration dependence is sharper than the data, once again due to the exponential distribution function. Most importantly, the model is able to capture the closed contours in the middle of the plot. The model predicts a much sharper fall off at low temperatures than what is observed. The binding energy at zero acceleration W_0 controls the rate of decrease of dissipation as a function of temperature. We have so far kept W_0 fixed at the value obtained by Iwasa [39]. However, there is a range of experimentally determined published values of W_0 [57] and a lower W_0 would give a better fit. On the whole, the dissipation is explained well for most of the $a - T$ plane except a small sliver at the lowest temperatures (note the log scale on the axes).

4.5 Conclusions

Starting with Iwasa's dislocation-vibration model [40, 41], we have developed a new dislocation model to obtain both the temperature and acceleration (or velocity) dependence of the frequency shift and dissipation observed in torsional oscillator experiments on solid ^{4}He. We provide a physical basis for the initially surprising result that temperature and acceleration have similar effects on the frequency shift and dissipation. The

model captures almost all the essential features of the frequency shift and dissipation over the entire acceleration-temperature plane. This result, along with the argument of Chapter 2 that there is no evidence for a superfluid-like transition in the microscopic relaxation times provides strong support for dislocation dynamics being the cause of the inertial anomaly first reported by Kim and Chan [44, 45].

APPENDIX A

BACKGROUND SUBTRACTION FOR THE FREE INERTIAL DECAY EXPERIMENT

To extract the dynamical quantities $f(V,T)$ and $D(V,T)$ from the free inertial decay (FID) experiments, the background observations due to non-solid-helium dynamics must be subtracted. To accomplish this, we acquired empty-cell ringdown data which captured the spurious effects of high-amplitude nonlinearity and low-amplitude electronic aliasing in the measured oscillator dissipation and frequency; these data are shown as the black diamonds in Figures A.1 and A.2. The oscillator dissipation (Figure A.2B) is acquired by curve-fitting a sliding exponential window 28 seconds wide across the measured amplitude decay (Figure A.1).

A smooth polynomial curve that captured the shape of the spurious nonlinearities for each dynamical quantity was fitted to these data and offset to correspond at high temperature with the solid helium data; the offsets f_∞ and D_∞ are indicated by the black arrows in Figure A.2A and B. The smoothed curves are indicated by the dashed black lines. After subtraction of these curves, the resultant dynamical quantities $f(V,T)$ and $D(V,T)$ are revealed as reported in the main text. For reference, the 47 mK FID - which was also used for illustration in Figure 2.2B - is shown here in Figure A.1 before background subtraction.

There remains a small, mostly constant (as a function of velocity and temperature) fraction of the total dissipation in the helium - which is visible as the difference between low-velocity empty cell and low-velocity 323 mK solid helium data in Figure A.2B - whose dynamical origin remains unexplained. However, at all temperatures and velocities, the component of the dissipation which we associate with the solid helium dynamics after subtraction of the dashed black line remains by far the dominant observed

feature of the oscillator dynamics.

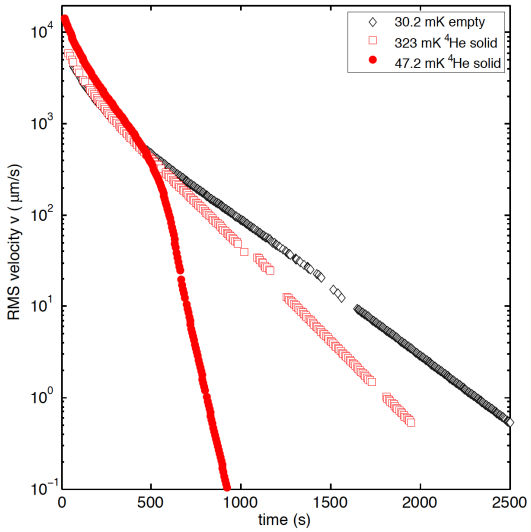

Figure A.1: Torsional oscillator amplitudes during FID ringdowns.

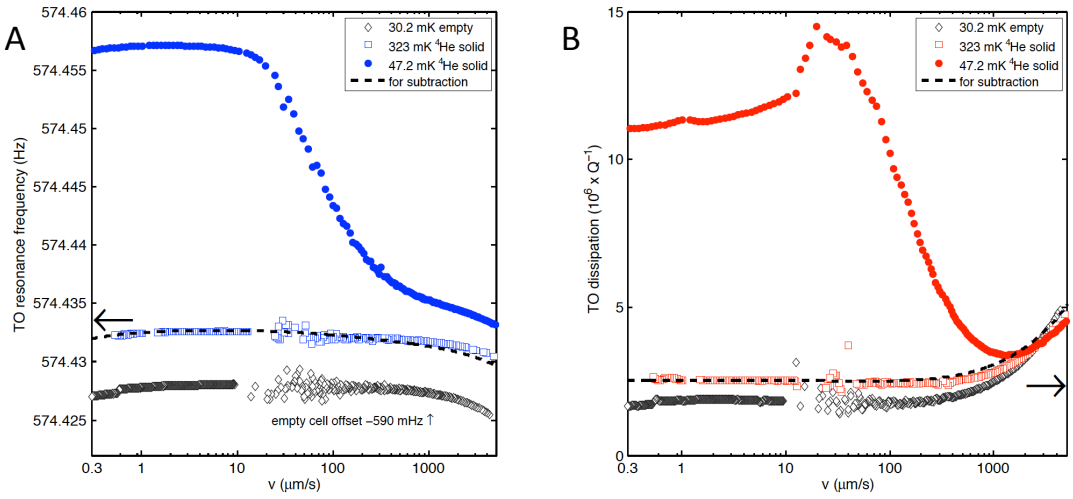

Figure A.2: **(A)** Torsional oscillator resonance frequency. f_∞ is indicated by a black arrow. The empty cell frequency is offset for clarity. **(B)** Torsional oscillator dissipation. D_∞ is indicated by a black arrow.

APPENDIX B

MACHINE DRAWINGS FOR THE MASS FLOW CHIP

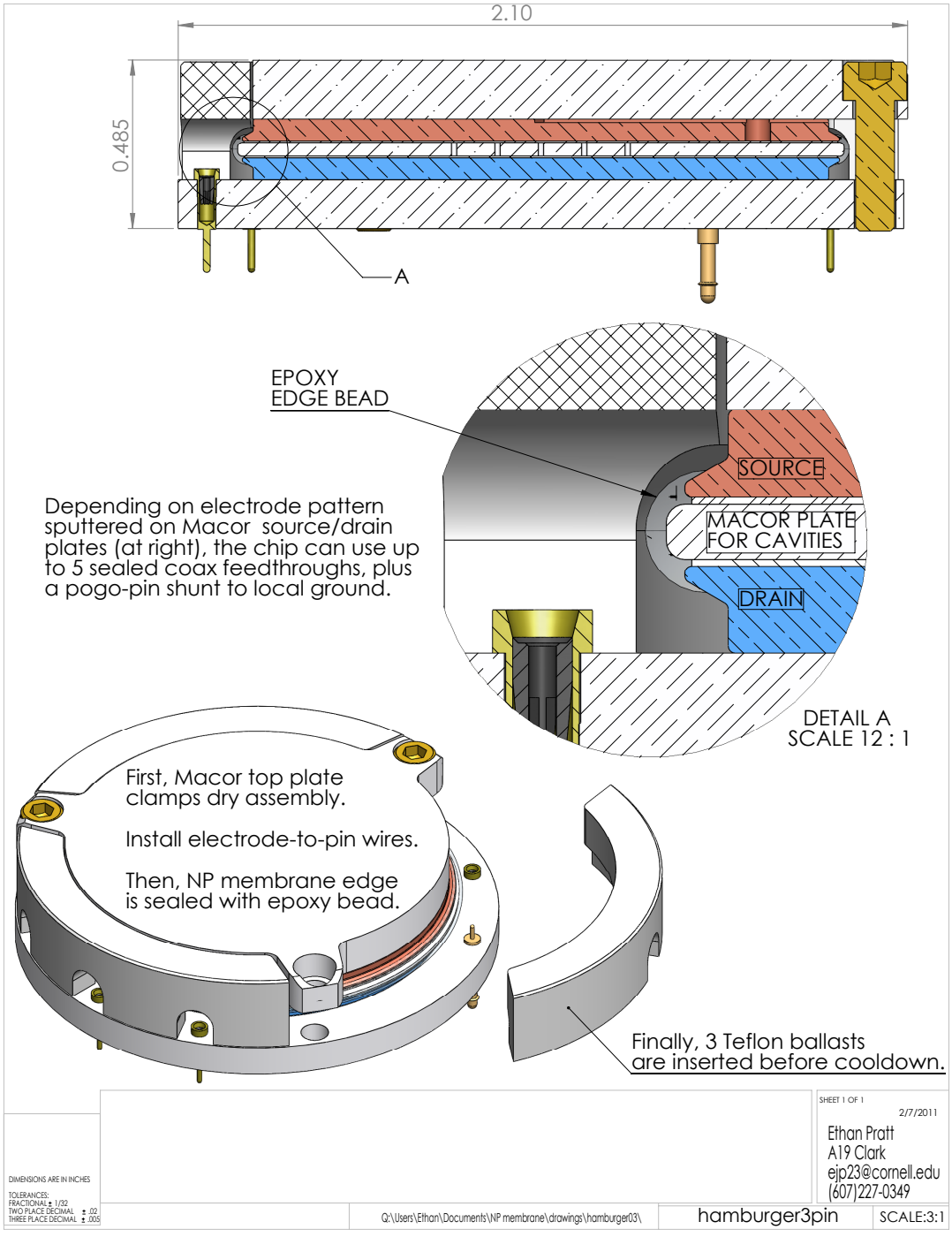

Figure B.1: Overview and design features of the mass flow chip.

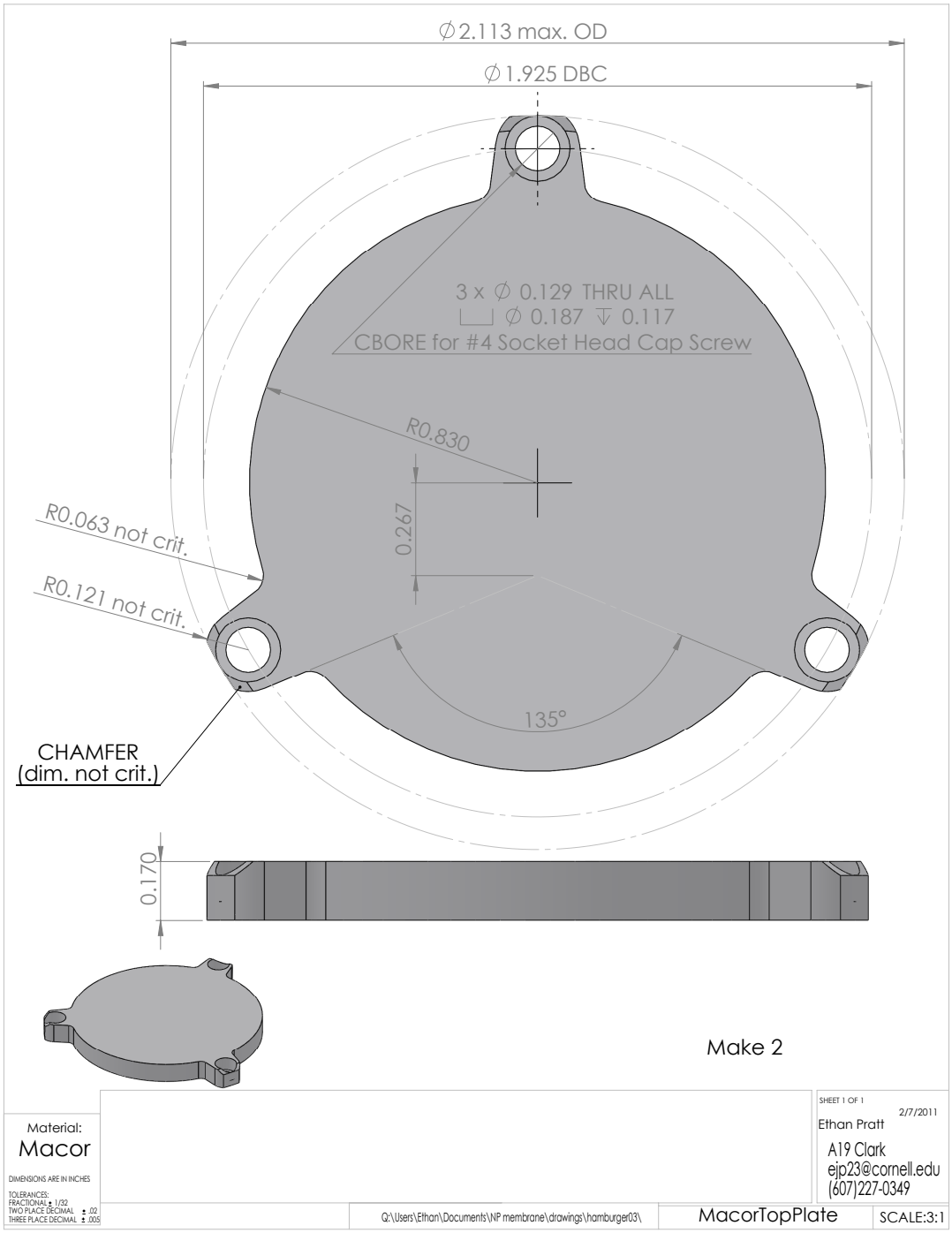

Figure B.2: The Macor top plate.

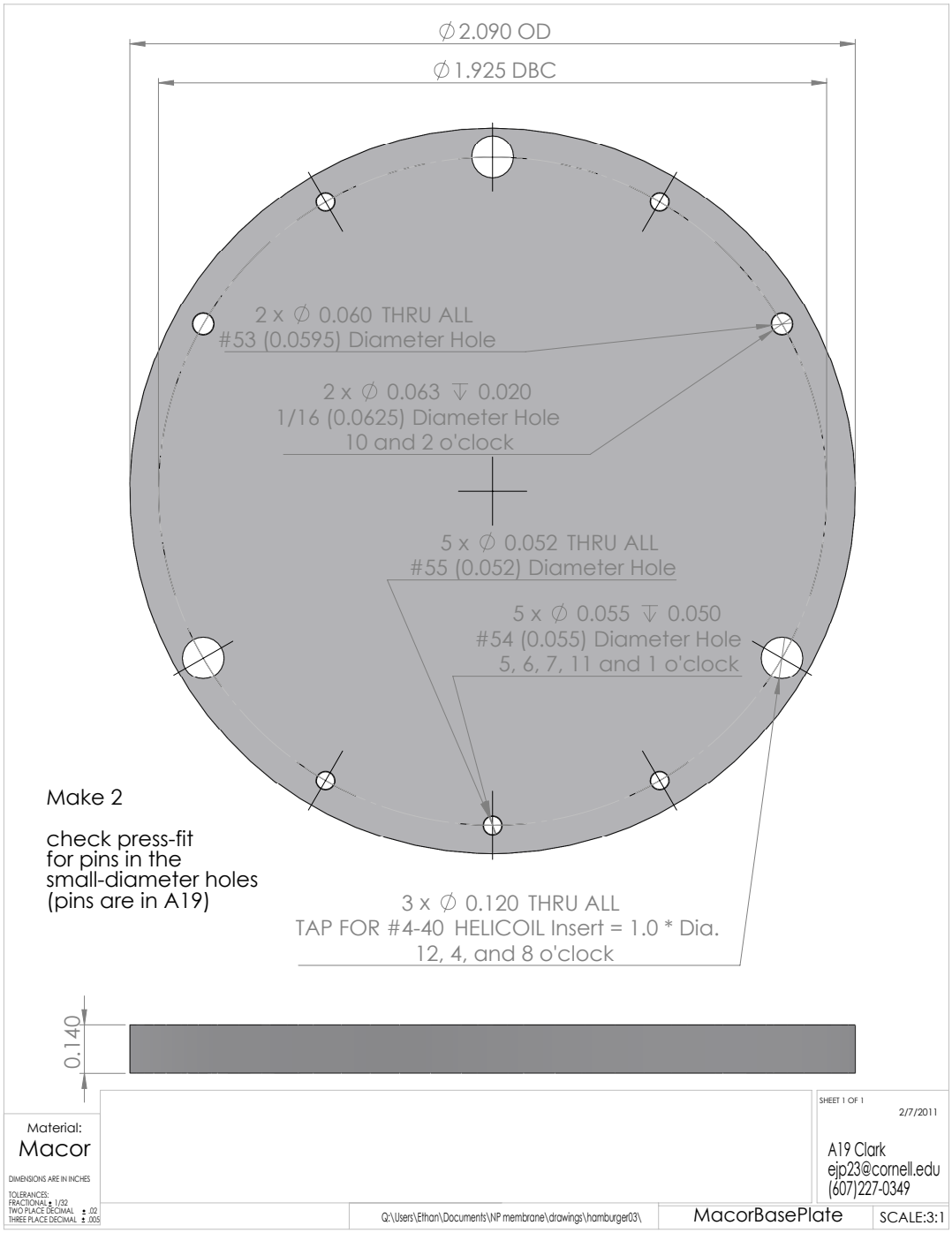

Figure B.3: The Macor base plate.

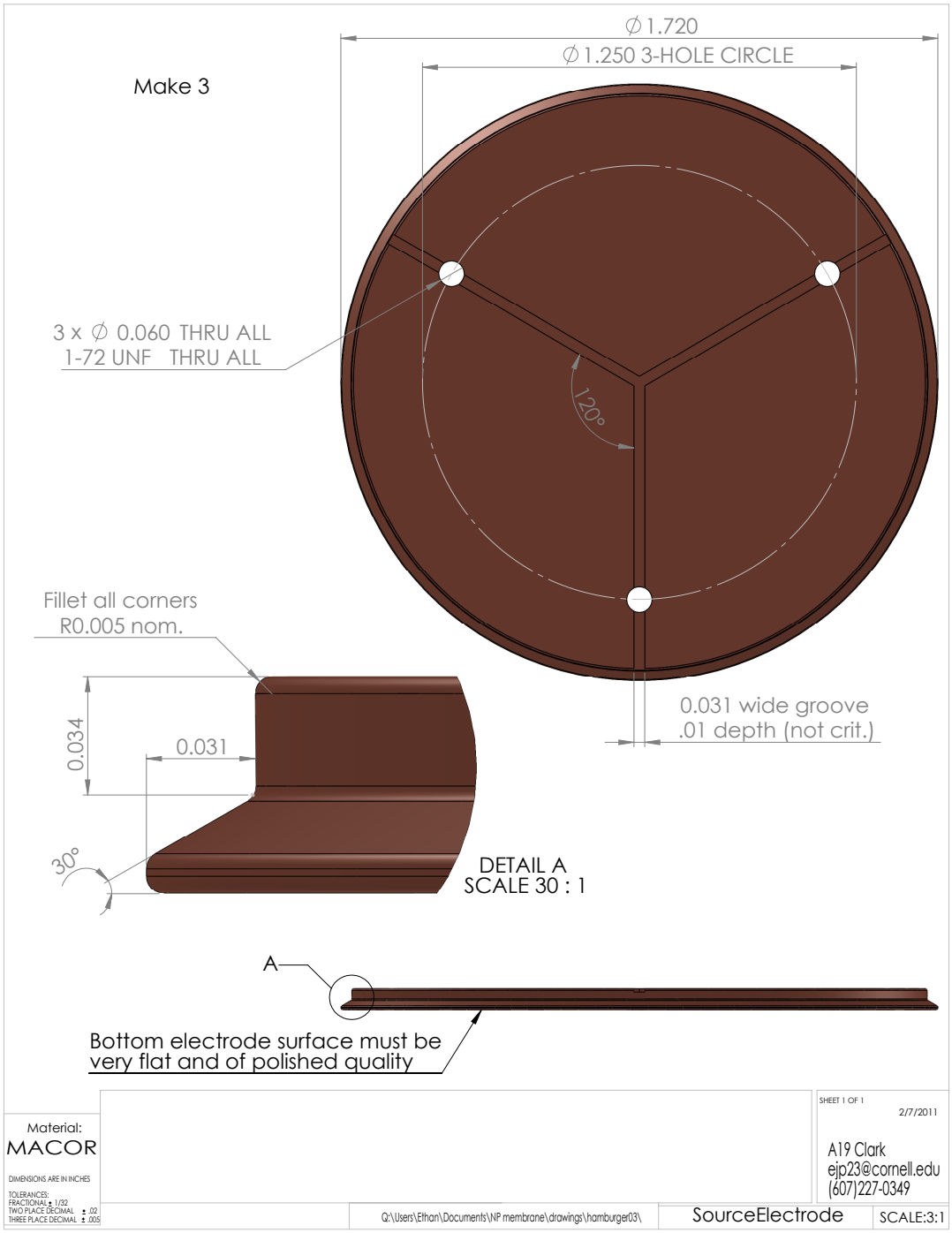

Figure B.4: The source electrode.

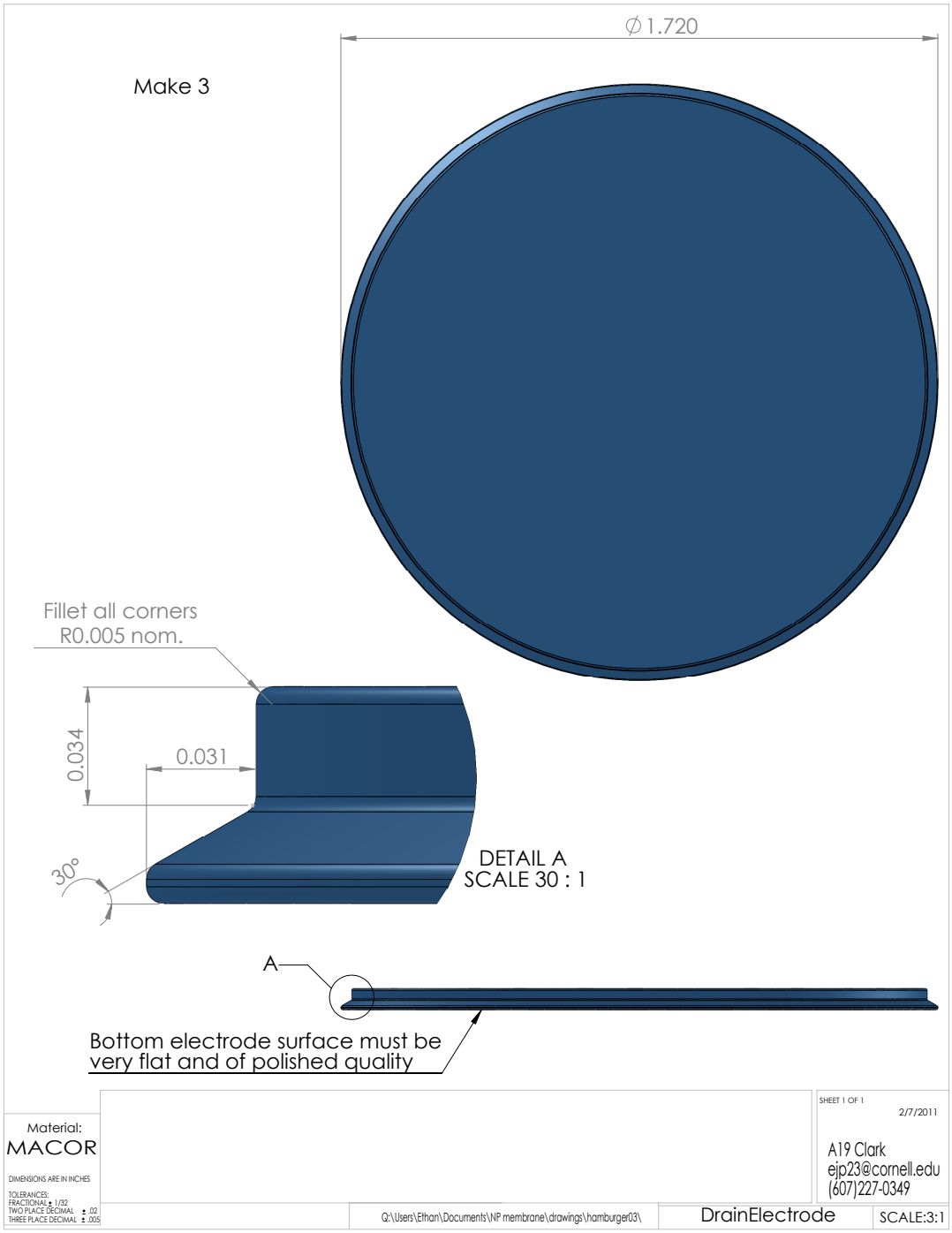

Figure B.5: The drain electrode.

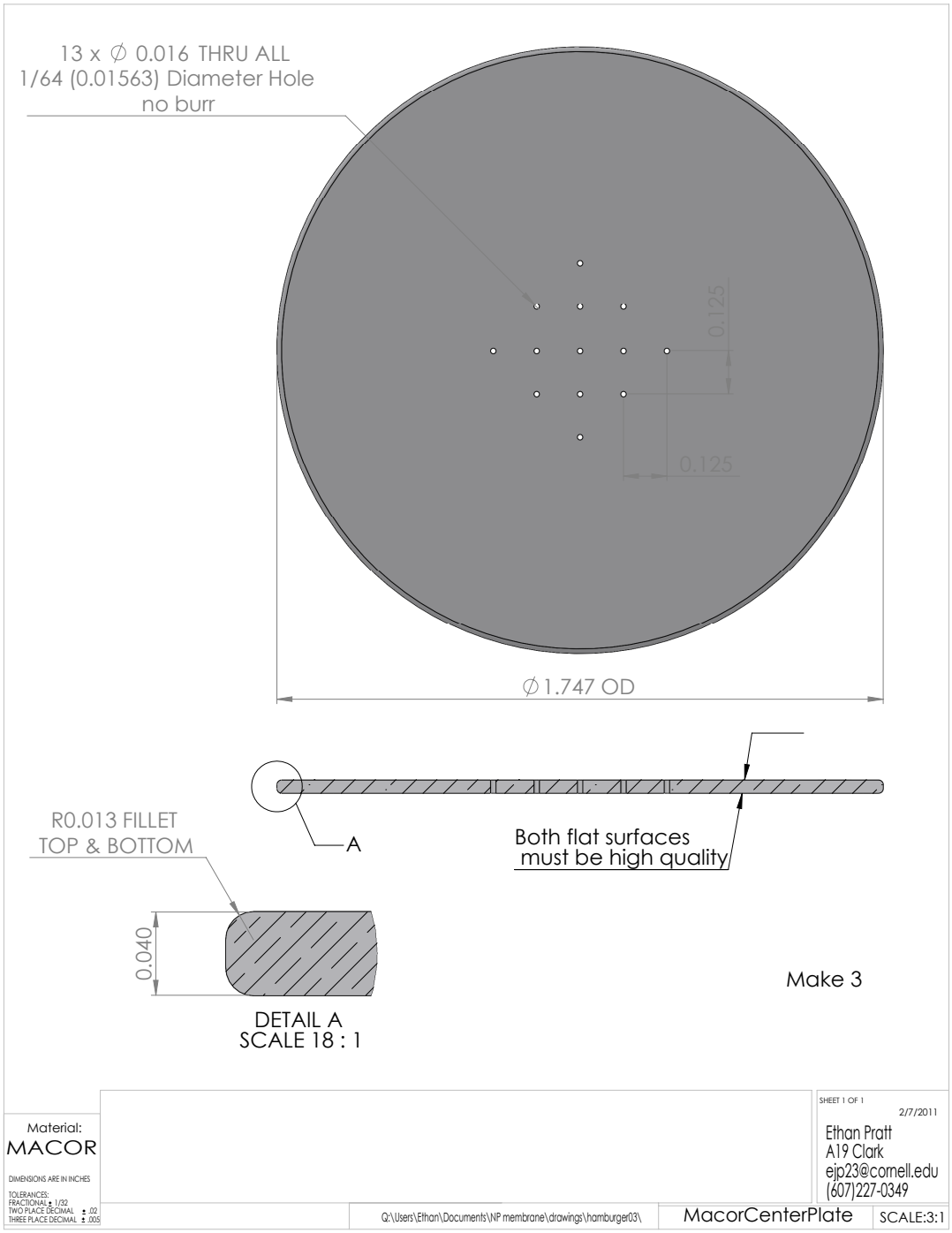

Figure B.6: The Macor center plate.

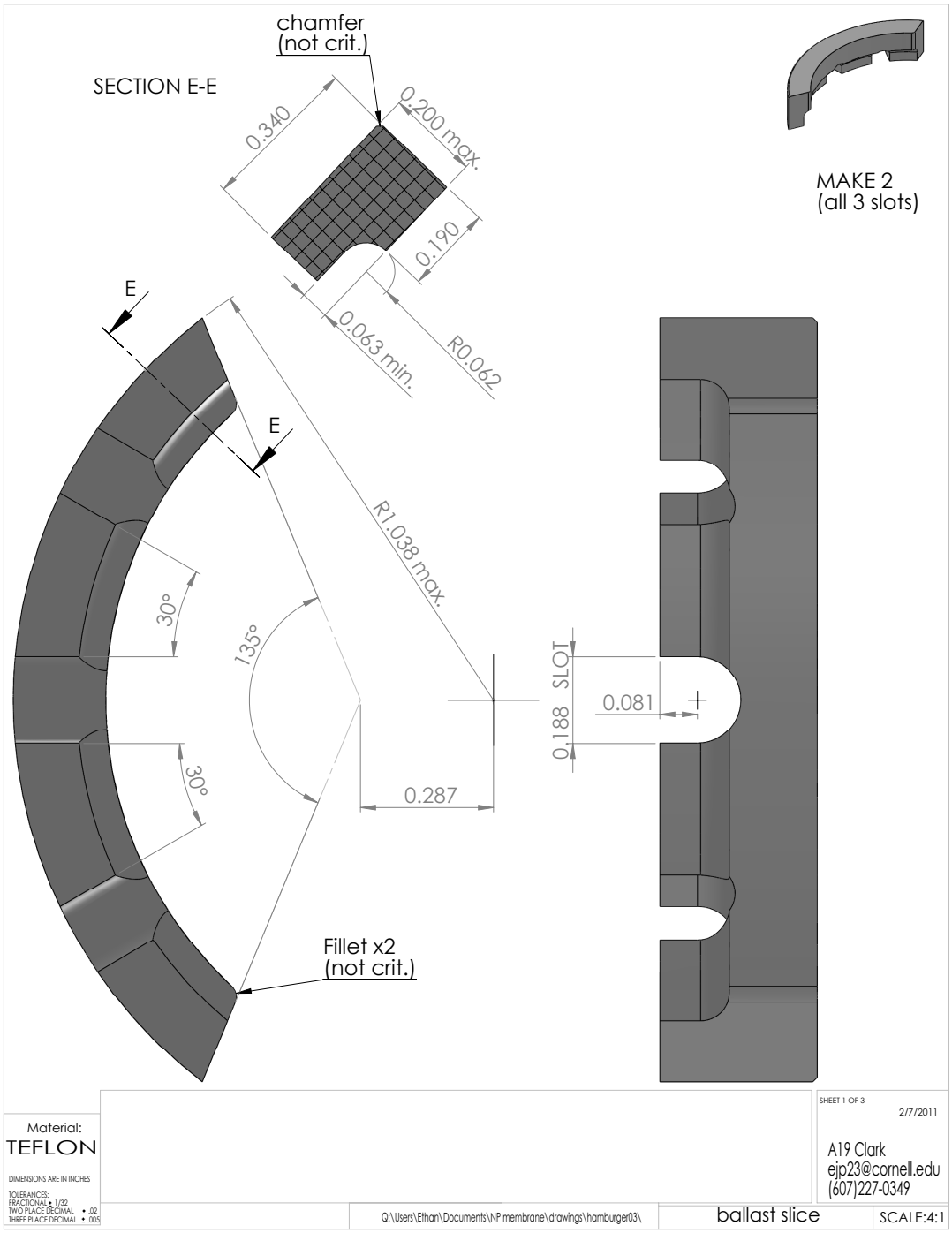

Figure B.7: The ballast slice with all three slots.

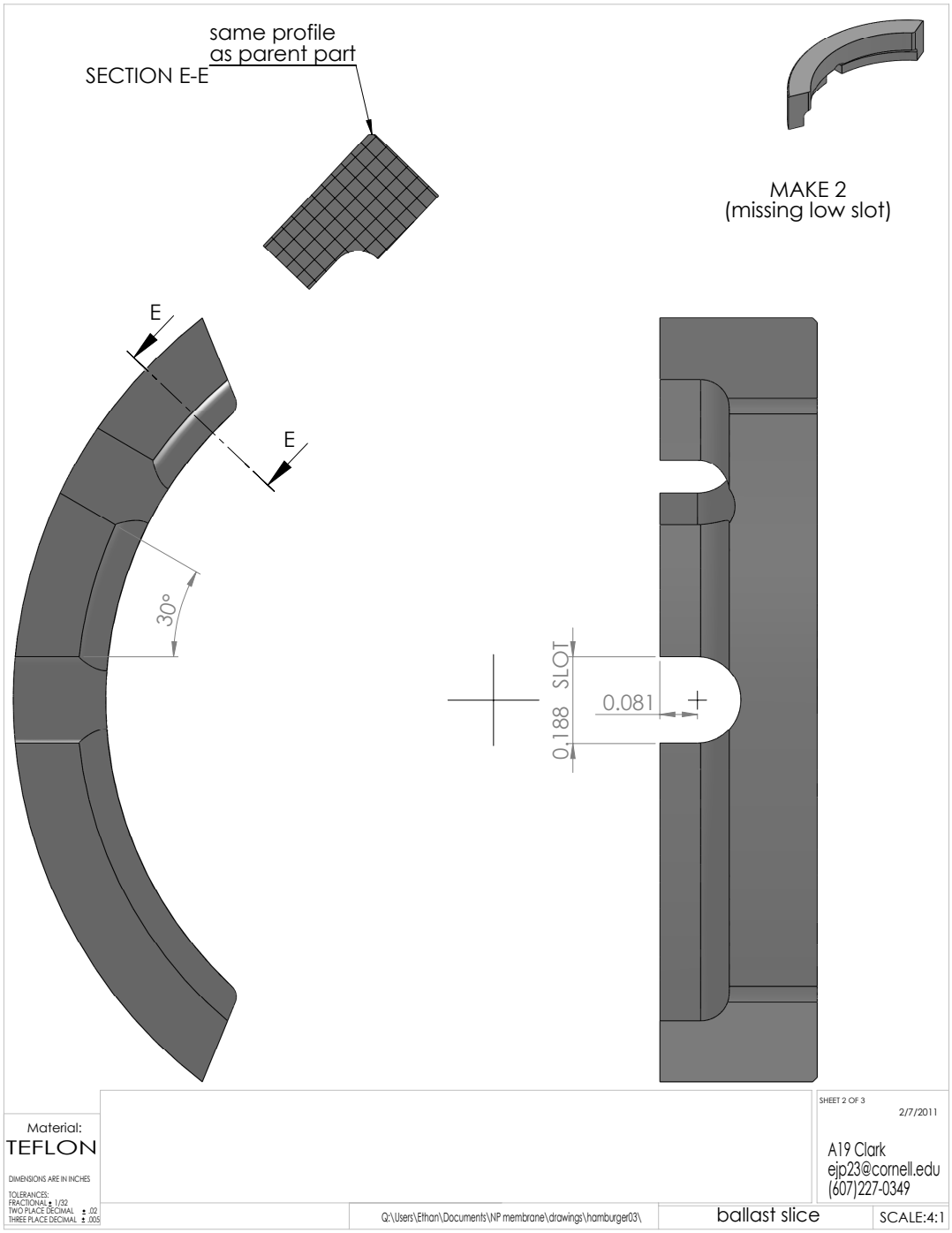

Figure B.8: The ballast slice with missing low slot.

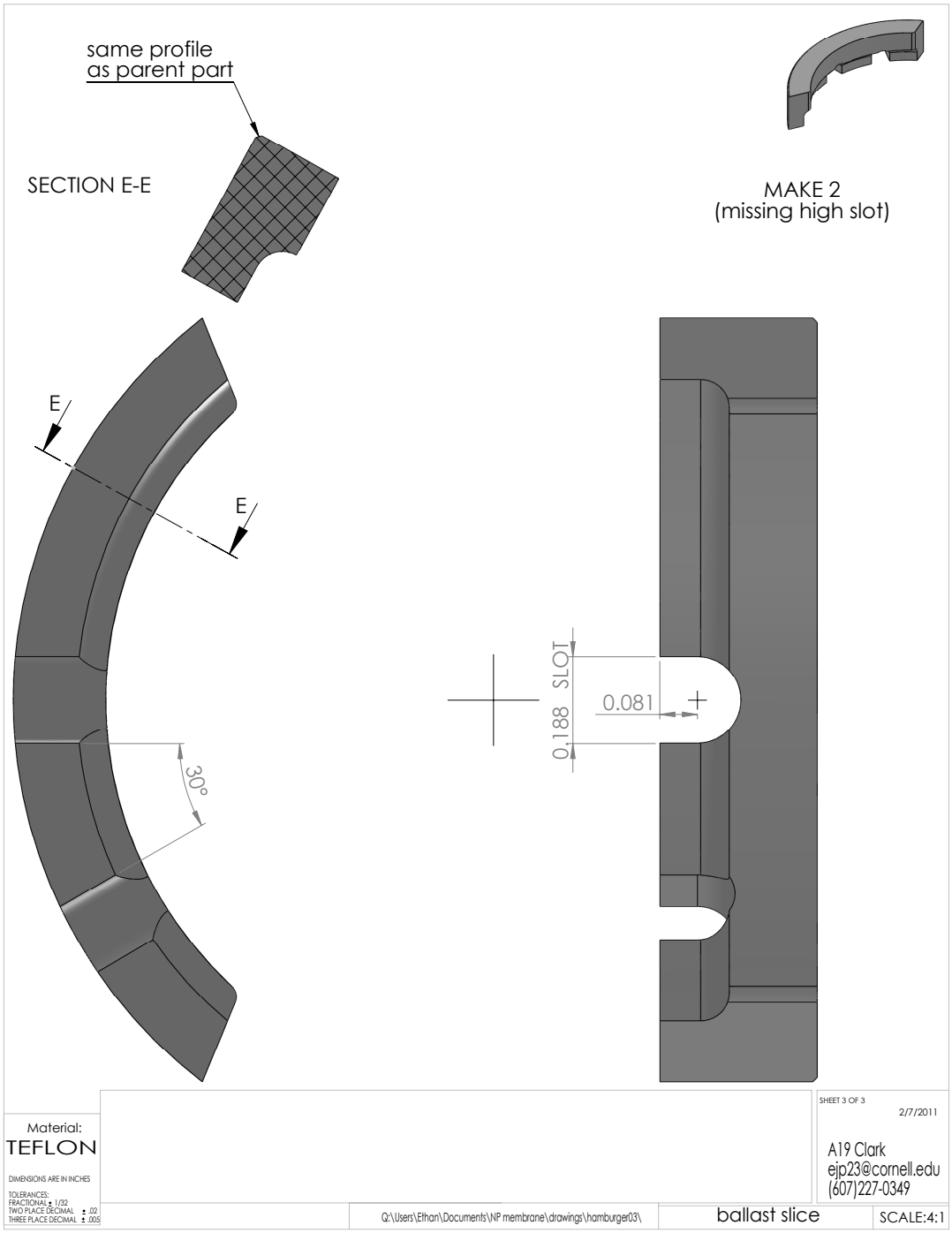

Figure B.9: The ballast slice with missing high slot.

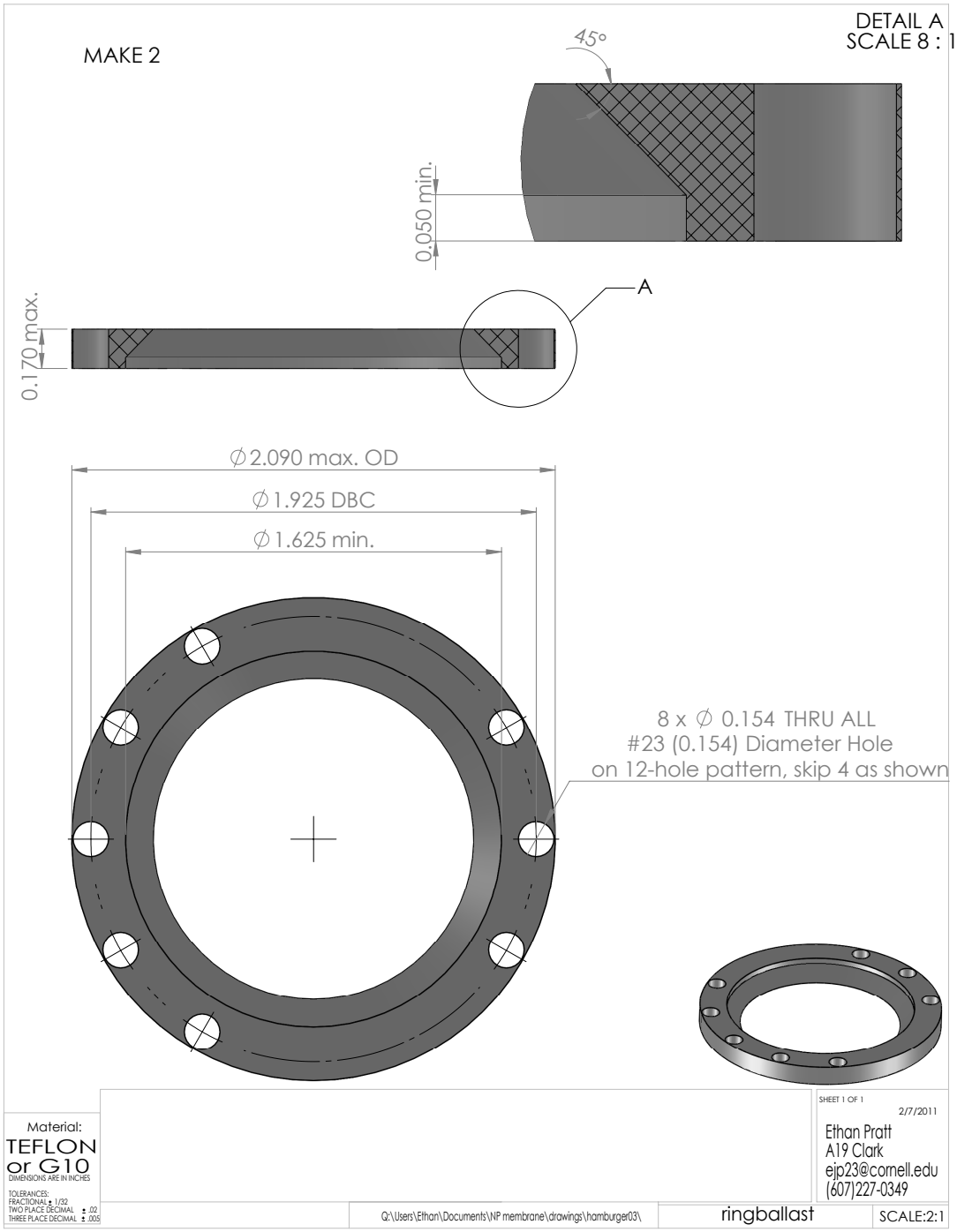

Figure B.10: The ring ballast.

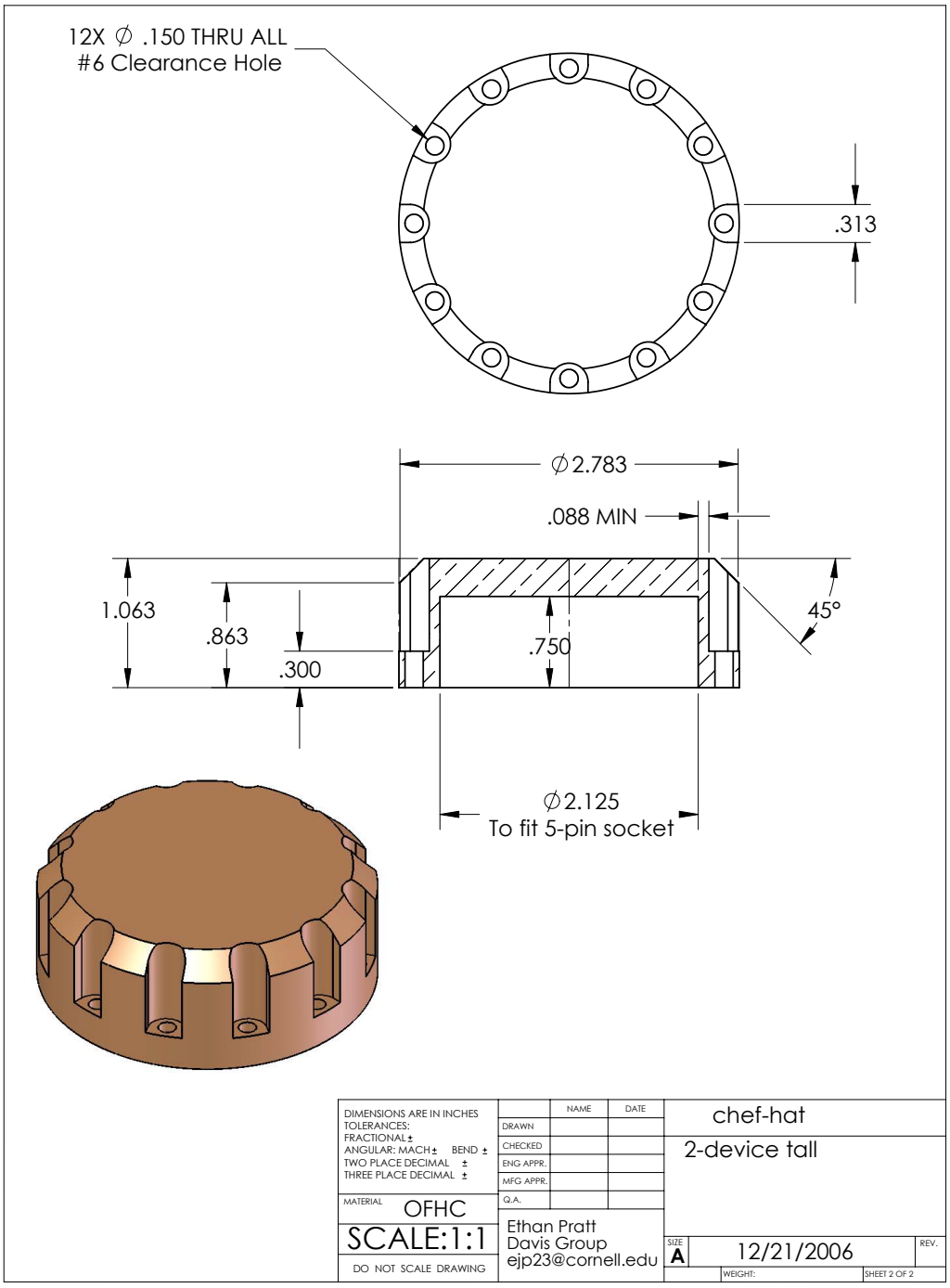

Figure B.11: The cell top to house the mass flow chip.

APPENDIX C

CONSTRUCTION AND ASSEMBLY OF A SEGMENTED TORSIONAL OSCILLATOR

In this appendix, we first propose an experiment to detect superfluid mass flow through solid ^{4}He using a torsional oscillator (TO) containing a C-shaped piece of nanoporous Vycor glass. We then present a few notes on construction, assembly, and testing of such an oscillator followed by the complete set of machine drawings.

C.1 The Proposal

Is the frequency shift seen in the Kim and Chan (KC) effect due to mass decoupling and superfluid flow or does it have a completely non superfluid origin like the vibrations of dislocations? How does one distinguish between these two possibilities? Consider a torsional oscillator in which helium occupies an annular region. Imagine, however, that most of the annular region is occupied by superfluid helium and only a tiny sliver is occupied by the solid state. If the KC effect is due to dislocation vibration, then we should not expect to observe any change in the frequency of the TO in the temperature range of the KC effects. This is because the fraction of the annular surface in contact with the solid would be extremely small. On the other hand, if the KC effects are indeed due to superfluid flow through the solid and if we further assume it is possible for superfluid to enter and exit the solid from an external reservoir, then we should see a strong KC type signal at the relevant temperatures.

The first technical challenge for the proposed experiment, however, is figuring out how to have superfluid in part of the annulus and solid in a different part of the annulus coexisting at the same temperature and pressure. For this, we turn to the properties of

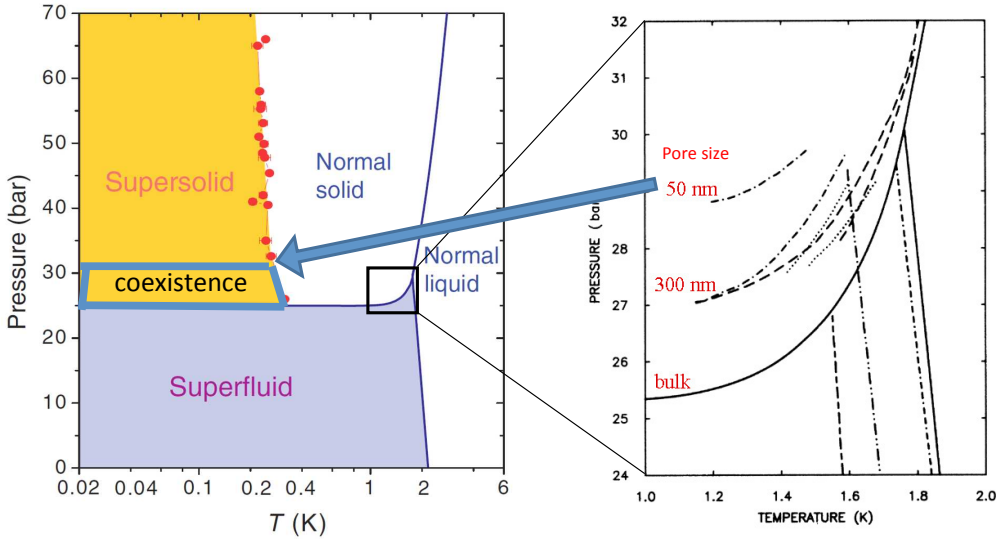

Figure C.1: Confinement of ^{4}He in nanometer-sized pores raises the pressure required for solidification. This property allows the fabrication of a new class of device in which solid and superfluid ^{4}He can coexist next to each other at the same temperature and pressure if a bulk region is present adjacent to a porous material. Figure adapted from [44] and [49].

^{4}He in confined geometries. The phase diagram of ^{4}He confined to nanometer sized pores is modified in two major respects [49]. Firstly, the superfluid transition temperature is lowered and more importantly for the present proposal, the pressure required for solidification is increased. The right panel of Figure C.1 shows the relevant parts of the phase diagram for a number of different pore sizes. This immediately suggest a coexistence region on the phase diagram (see left panel of Figure C.1) in which, at the same temperature and pressure, we have stable solid in bulk regions and stable superfluid in porous regions. The smaller the pores, the larger is the coexistence region.

Figure C.2 is a schematic cross section of a TO illustrating the implementation of this idea. The body of the TO is made of Stycast 1266 and the annulus is segmented into two regions. One region is occupied by a C-shaped piece of nanoporous (pore size $\sim$ 10 nm) Vycor glass. The glass almost completely fills the annular region leaving only a tiny sliver unoccupied. This sliver constitutes the second region - the bulk region. The

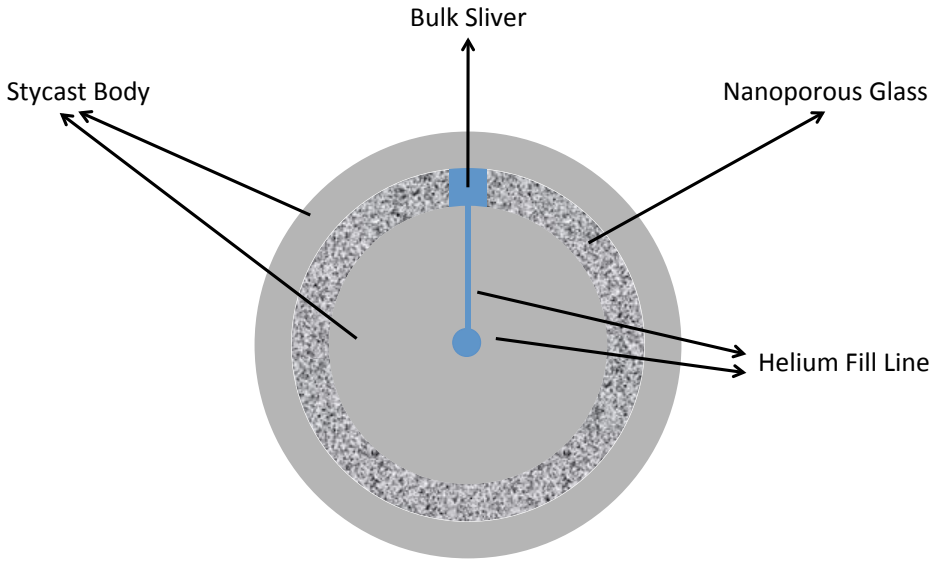

Figure C.2: Schematic cross-section of the segmented torsional oscillator. The annulus occupied by helium is segmented into two regions, a bulk region and a nanoporous region. By maintaining the temperature and pressure appropriately (see Figure C.1), three regimes can be accessed: superfluid in both regions, solid in both regions, or superfluid in the nanoporous region coexisting with solid in the bulk region.

fill line used to fill the cell with helium is also shown. As can be seen from Figure C.1, control of the temperature and pressure of the helium in the cell allows us to access three distinct regimes. When the temperature is sufficiently low and the pressure is below $\sim$ 25 bar (the bulk melting pressure), both regions are occupied by superfluid. On the other extreme, if the pressure is higher than the solidification pressure in the pores, then both regions are occupied by the solid state. The third regime, one of coexistence, is when the pressure is somewhere within the coexistence region. In this regime, the pores contain superfluid and the bulk sliver contains the solid.

How will such an oscillator help us distinguish between the competing hypotheses of superflow within the solid versus no superflow. Let us consider some predictions for the frequency shift in the temperature range of the observed KC effects. Before we begin to make these prediction, however, we need to consider carefully the issue of whether

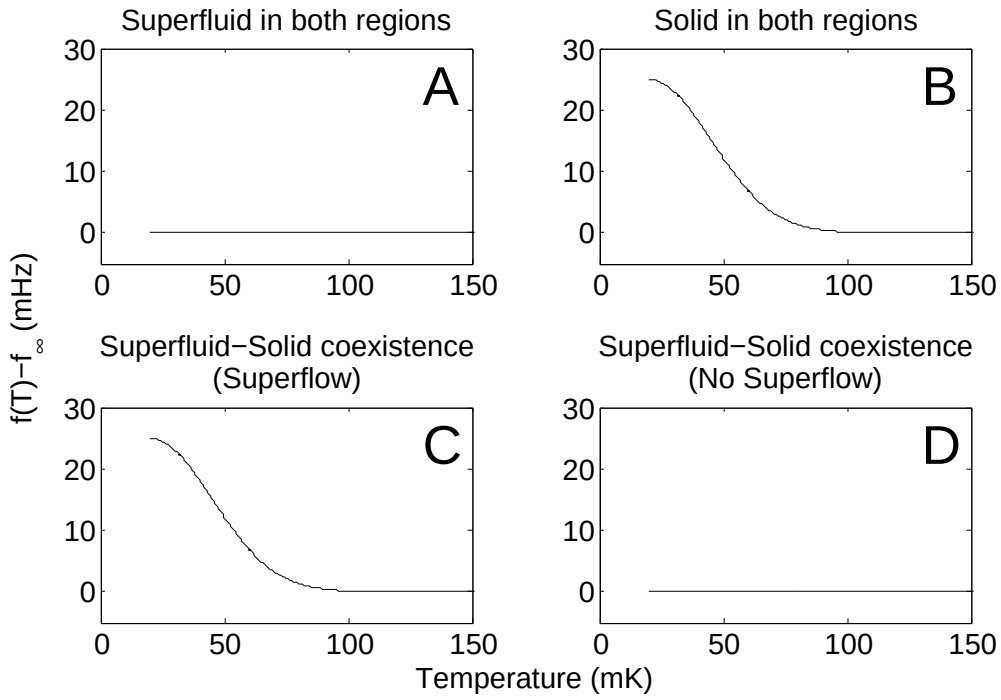

Figure C.3: Predictions for the temperature dependence of the frequency shift of the oscillator in the three regimes assuming that the Kim and Chan signal exists in nanoporous Vycor glass as originally reported in 2004 [45]. f_∞ is the frequency of the TO at high temperatures, away from the range of the KC effects. **(A)** Superfluid in both bulk and nanoporous regions, **(B)** solid in both regions, **(C)** coexistence regime in the superflow hypothesis and **(D)** in the no-superflow hypothesis. In this simple model, we ignore the possible contributions to the signal that may arise due to the solid in the torsion rod, solid in small bulk regions outside of the annulus, or due to non-rigidity of the oscillator body.

we expect to observe the KC effects in solid ^{4}He confined entirely in nanoporous Vycor. Kim and Chan's original paper [45], published in 2006, reported the observation of these KC effects in solid ^{4}He confined in Vycor. However, in 2012, Chan's group repeated this experiment, this time making absolutely sure that there were no bulk regions within the TO unoccupied by Vycor that the helium could fill. They now found no evidence for the KC effects in such a cell [43]. We thus make separate predictions for the two cases, first assuming that the KC effects can be observed for solid ^{4}He in Vycor and then

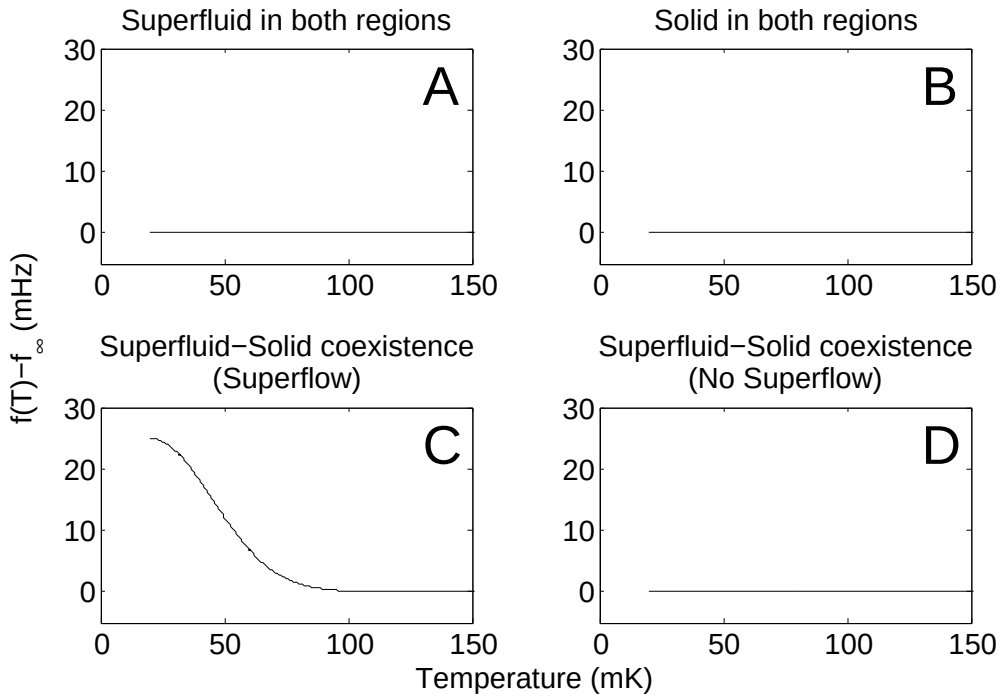

Figure C.4: Predictions for the temperature dependence of the frequency shift of the oscillator in the three regimes assuming that the Kim and Chan signal does not exist in nanoporous Vycor glass as recently reported in 2012 [43]. f_∞ is the frequency of the TO at high temperatures, away from the range of the KC effects. **(A)** Superfluid in both bulk and nanoporous regions, **(B)** solid in both regions, **(C)** coexistence regime in the superflow hypothesis and **(D)** in the no-superflow hypothesis. In this simple model, we ignore the possible contributions to the signal that may arise due to the solid in the torsion rod, solid in small bulk regions outside of the annulus, or due to non-rigidity of the oscillator body.

assuming that they cannot.

Figure C.3 presents predictions for the frequency shift as a function of temperature (in the range of the observed KC effects) assuming that that KC effects can be observed in solid ^{4}He present in nanoporous materials like Vycor. We don't expect to see any change in the frequency when the entire annulus is occupied by superfluid (A). If both regions contain solid, then the situation should be very similar to the original KC experiment and so we expect to see a prominent frequency shift (B). The interesting and

distinguishing prediction clearly, is in the coexistence regime. If the superflow hypothesis is correct and solid ^{4}He enters a supersolid state which can support superflow, we should expect to see a KC type signal for the frequency shift (C). On the other hand, if there is no superflow allowed through the solid, then we expect a flat response (D) since we don't expect the elastic or dislocation effects of the tiny solid sliver on the TO to be significant.

We now turn to Figure C.4 which presents the predictions for the frequency shifts we expect if the KC effects cannot be observed in nanoporous materials like Vyvor. Once again, as in the previous case, we don't expect to see any change in the frequency when both regions are filled with superfluid (A). Unlike the previous case however, when both regions are filled with solid, we now expect the frequency response to be flat (B) since the annulus is mostly filled with Vycor in which KC effects cannot be supported. The coexistence regime once again presents us with two possibilities, a KC like response (C) if solid ^{4}He supports superflow and a flat response if it does not (D).

Figures C.3 and C.4 thus demonstrate how the superflow versus no superflow hypotheses might be distinguished. In addition, depending on the results of the (B) panels, it might also be possible to tell whether or not solid ^{4}He in Vycor can support KC effects. It is important to note, however, that the predictions presented in these figures are based on a model of the TO which makes several simplifying assumptions. The first assumption is that the solid helium present within the torsion rod does not contribute to the KC effects [13]. The second assumption is that there are no bulk spaces that the helium can occupy within the body of the TO [43]. The third assumption is that the TO is sufficiently rigid and we can neglect various kinds of elasticity effects that can contribute to the change in frequency [54, 71, 53].

C.2 Assembly and Testing

The complete set of machine drawings can be found in Section C.3. In this section, we present a few notes on the assembly and testing of the torsional oscillator.

A key component of the TO is the Vycor annulus. Vycor is porous glass made by Corning. It has a porosity of $\sim 28\%$. The Vycor used in this experiment was purchased from Advanced Glass and Ceramics in the form of tubes (OD $\sim$ 10.5 mm and wall thickness $\sim$ 1.2 mm). The tube was then cut to the desired height ($\sim$ 6 mm) using a diamond saw and then polished using fine sand paper. To confirm that the Vycor glass had pores of the right size, we took a scanning electron microscope (SEM) image of a cleaved surface of the glass. Pores of size $\sim$ 10 nm can clearly be seen in Figure C.5.

Figure C.17 shows the Stycast cell top. This piece is made of Stycast and has in it an annular slot designed to hold the Vycor annulus. Since we needed to avoid any gaps between the Stycast walls and the Vycor piece after assembly (unwanted bulk spaces), the assembly plan involved coating the Vycor annulus with fresh Stycast and then inserting it into the Stycast cell top. For this plan to work, it is essential that fresh Stycast does not penetrate the pores of Vycor. We confirmed that this is indeed the case by immersing a piece of Vycor in fresh Stycast and letting the Stycast set. Figure C.6 shows such a piece. A hole was then drilled though the Stycast such that it passed through the wall of the Vycor annulus along its height. Black ink was then poured into the hole and allowed to diffuse. As can be seen from the figure, the ink was able to diffuse through the pores of Vycor proving that the fresh Stycast does not significantly penetrate the pores of Vycor.

The body of the TO was made of Stycast 1266. Stycast 1266 was first prepared and allowed to set in vials which were later machined. The following is a brief description of

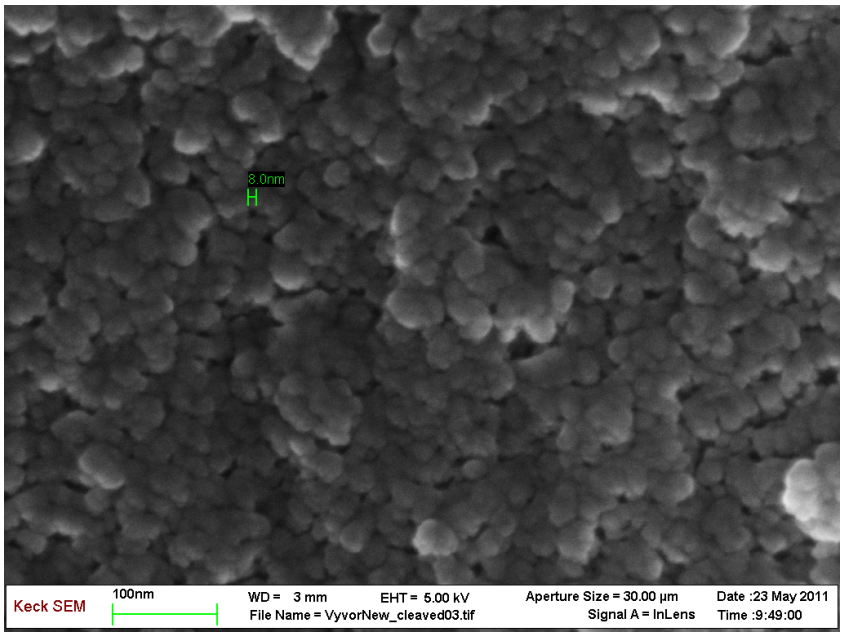

Figure C.5: A scanning electron microscope (SEM) image of a cleaved surface of the Vycor glass used in the segmented torsional oscillator. Pores of ~10 nanometers can easily be seen.

how the Stycast was prepared. A clean glass beaker was placed on an accurate weighing scale and tared. About 10 grams of Stycast 1266 Part A was poured into the beaker using a clean spatula. 28 parts per hundred by weight of Stycast 1266 Part B was then poured into the beaker using a clean dropper. The beaker was removed from the scale and the two parts were mixed slowly but thoroughly for 10 min. The beaker was then placed into a desiccator connected to a diaphragm pump and pumped on for 10 min to deair it. The Stycast was observed to initially foam and froth and then settle down. The pressure inside the desiccator was slowly returned to 1 atm and the beaker was removed. The deaired Stycast was carefully transferred from the beaker to a vial. The Stycast in the vial was similarly deaired for 10 min in the desiccator. The vial was then taken out of the desiccator and placed on a shelf and the Stycast was allowed to set at room temperature and pressure undisturbed.

Figure C.16 shows the Beryllium Copper (BeCu) torsion rod. After machining, the torsion rod was cleaned by sonicating it with acetone followed by isopropanol. It was

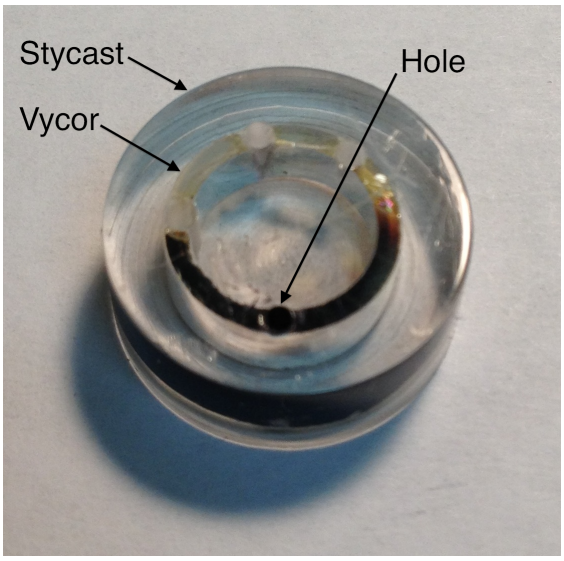

Figure C.6: A porosity test of Vycor embedded in Stycast 1266. An annulus of Vycor was submerged in freshly prepared Stycast. After the Stycast had set, a hole was drilled through the Stycast and the entire height of the Vycor annulus. A drop of black ink poured into the hole diffused through the Vycor demonstrating that fresh Stycast does not penetrate significantly into the pores of Vycor.

then annealed at 316 C for 8 hours in a vacuum furnace.

The procedure followed to assemble the TO once all the parts had been machined is briefly described here. Please refer to the machine drawings of the various parts in Section C.3. The captions to these figures also contain useful information about how various parts were put together.

1. The Vycor annulus was coated with fresh Stycast and then inserted into the Stycast cell top (Figure C.17). This piece was then deaired in the desiccator to remove any air bubbles that might have gotten trapped between the Vycor and Stycast cell top. After deairing, the Stycast was allowed to set.

2. A fine drill bit (diameter slightly bigger than the wall thickness of the Vycor annulus) was used to drill a hole through height of the Vycor annulus to create the bulk region. The hole was aligned with the helium fill slot on the Stycast cell top.

3. The BeCu torsion rod (Figure C.16) was then screwed into the Stycast cell top using fresh Stycast as glue. The torsion rod was initially screwed in all the way and then retracted just enough so that the tabs on the stycast cell top alligned with the screw holed in the torsion rod. The Stycast was then allowed to set.

4. The Stycast cell bottom (Figure C.18) was then glued on to the torsion rod-Stycast cell top-Stycast cell bottom assembly using fresh Stycast and the Stycast was allowed to set. A useful trick at this stage is to coat the outside of the Stycast cell bottom with a very thin layer of fresh Stycast. This has the effect of making the Stycast cell bottom transparent and it is thus very easy to ensure that the fill line is not blocked by excess glue.

5. The magnesium capacitor electrode plate (Figure C.19) is then glued on to the tabs on the Stycast cell top using fresh Stycast and allowed to set.

6. The BeCu magnet holders (Figure C.20) are clipped on to the body of the oscillator, aligned and glued in place by a small amount of fresh Stycast and allowed to set.

Figure C.7 is a photograph of a partially assembled TO, depicting the TO after step 4 in the list above. At this stage, the TO was pressure tested and did not explode up to 100 bar at 4 K.

Figure C.8 is a photograph of the fully assembled TO mounted on the cryostat. The electrode holders and electrodes were assembled as shown in Figure C.10.

The TO was assembled and mounted on our dilution cryostat as described above. The cryostat was then cooled to 20 mK and the resonance frequency and Q of the oscillator were determined. The resonance frequency was found to be ~ 401.1 Hz. To obtain a rough estimate of the Q, the TO was rung up using the capacitor electrodes close to the

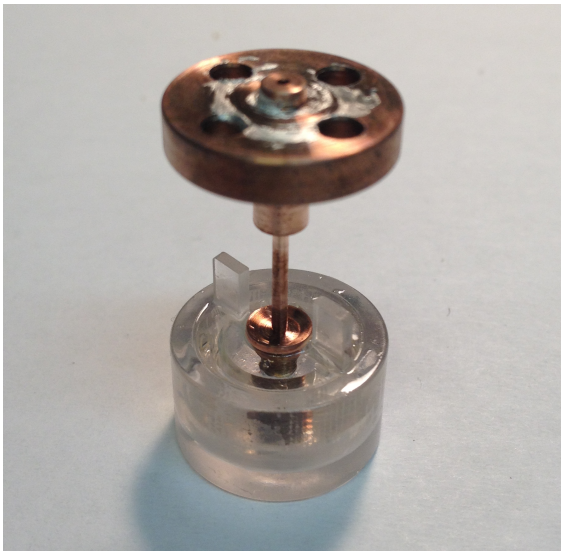

Figure C.7: Photograph of a partially assembled segmented torsional oscillator. The BeCu torsion rod, the Vycor annulus, and the Stycast body are shown. To be assembled are BeCu magnet holders and the Mg capacitor electrode plate.

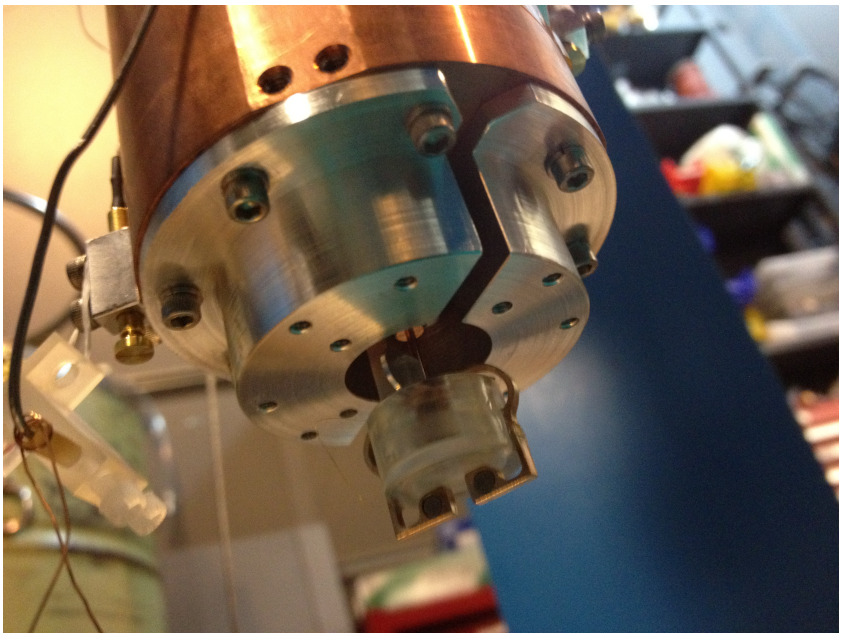

Figure C.8: Photograph of the fully assembled segmented torsional oscillator mounted on the copper inertial isolation block of the dilution fridge. The Al electrode holder platform can also be seen. The electrode holders are not yet in place. Figure C.10 depicts what the electrode assembly would look like.

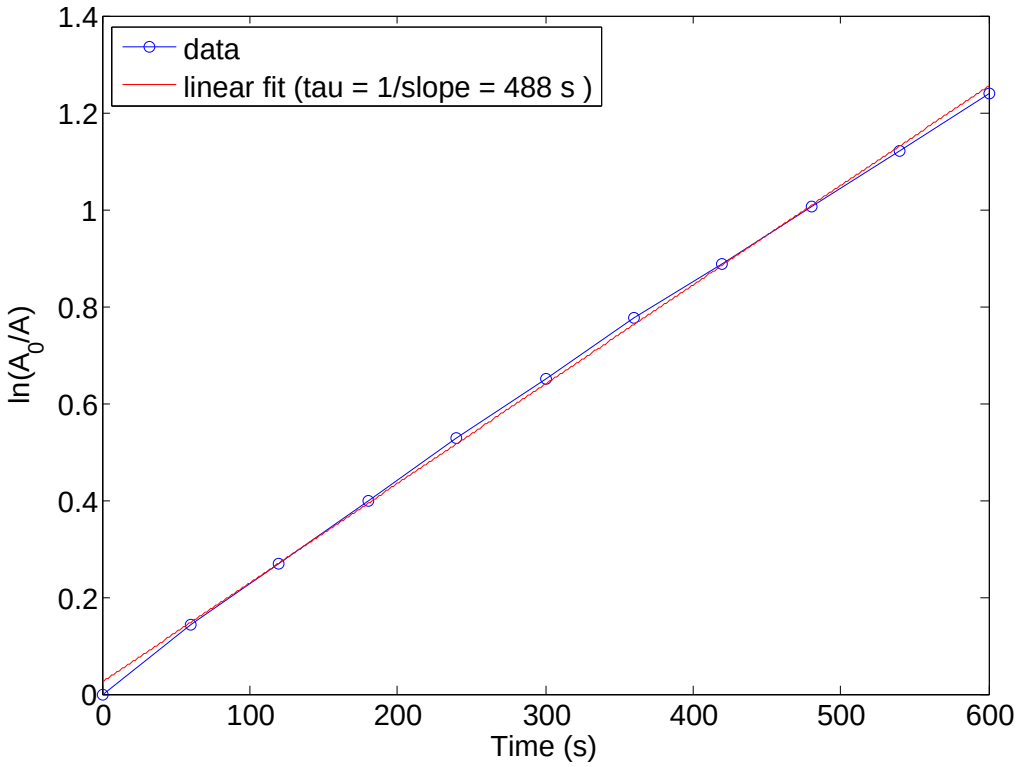

Figure C.9: Calculation of the Q of the segmented torsional oscillator at 20 mK. The oscillator was rung up and then allowed to decay. The decay time constant can be used to calculate Q since $Q = \omega_0\tau/2$. The value of Q was determined to be 6×10^5.

resonance frequency and the waveform was obtained on an oscilloscope. The TO was rung up till the amplitude was $\sim$ 1 V RMS and the drive was turned off. The waveform could be seen decaying on the oscilloscope and the amplitude was recorded at several times. The amplitude is given by $A(t) = A_0\exp(-t/\tau) = A_0\exp(-\omega_0 t/2Q)$ and hence $Q = \omega_0\tau/t$. Figure C.9 shows the plot used to determine the decay constant τ from which the Q was estimated to be $\sim 6 \times 10^5$.

C.3 Machine Drawings

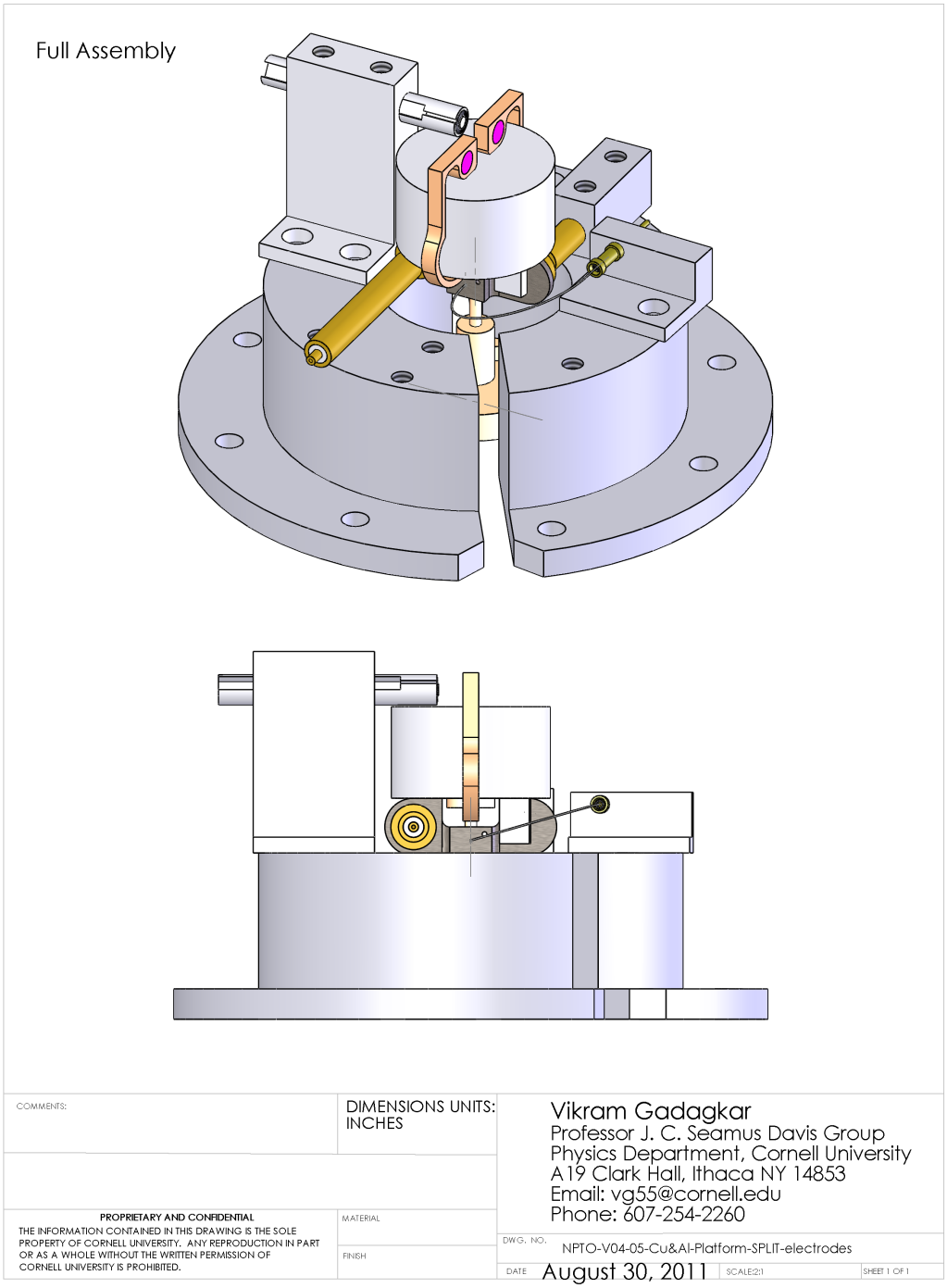

Figure C.10: The full torsional oscillator assembly with all electrodes. This assembly gets mounted on the massive copper isolation block which is thermally linked to the mixing chamber.

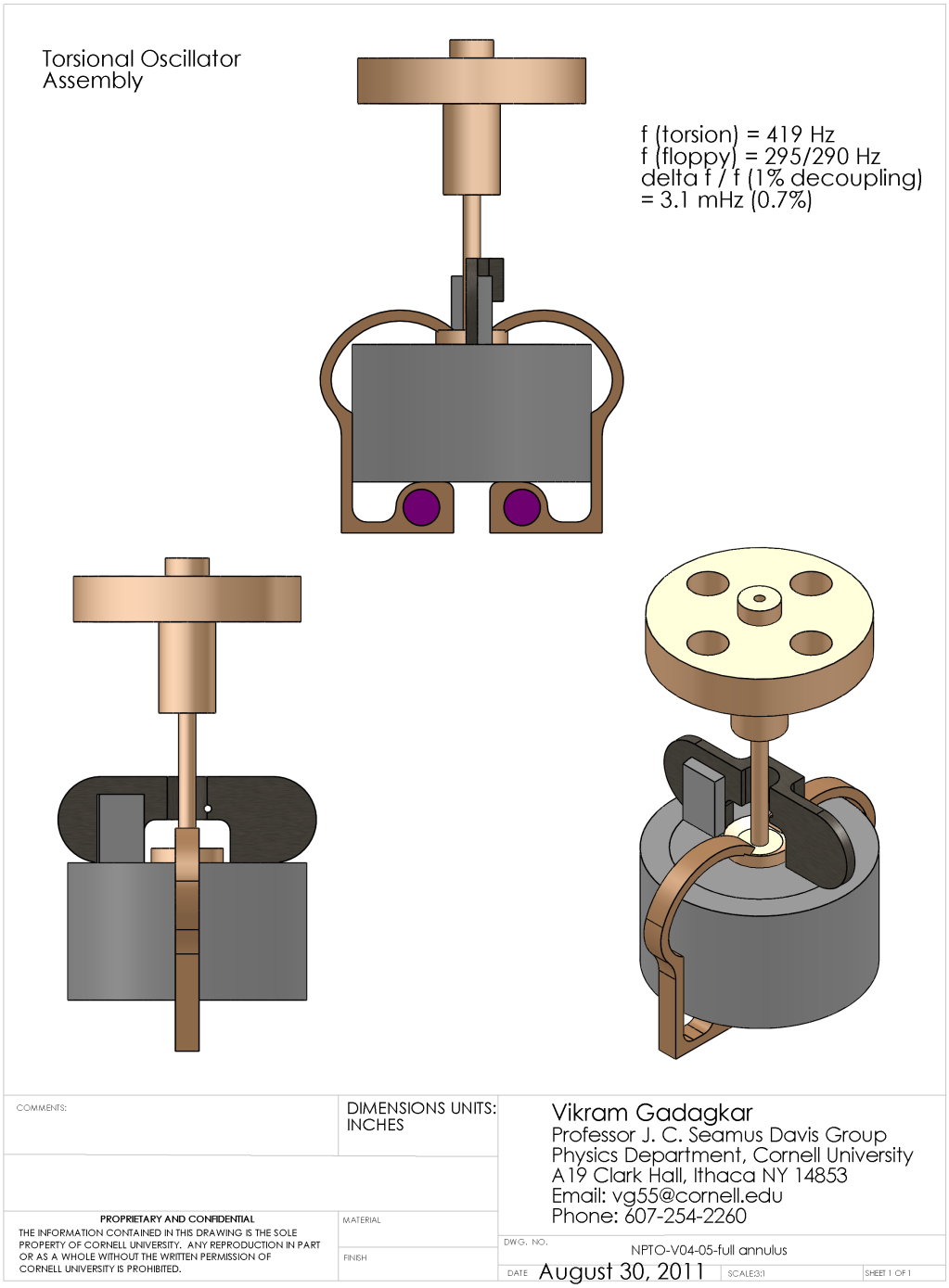

Figure C.11: The torsional oscillator assembly. Also shown are the predictions for the frequencies of the torsion and floppy modes and the fractional change in frequency for a hypothetical '1% mass decoupling'.

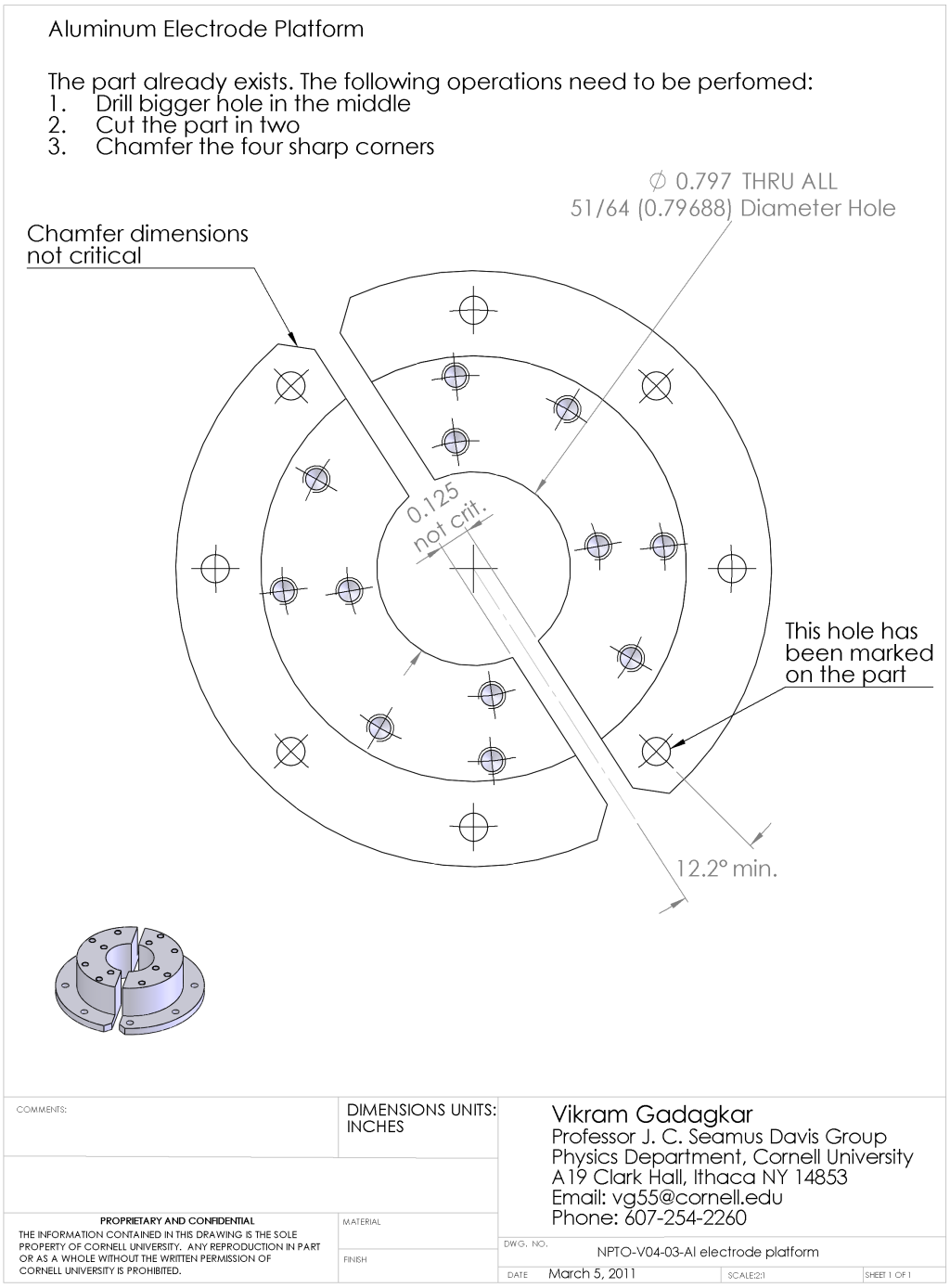

Figure C.12: The aluminum electrode platform on which the drive and detect capacitor electrode, the squid electrode, and the protected ground electrode holders are mounted. The platform is in two parts which enables swinging one hemisphere out on a single screw to provide access to the torsional oscillator.

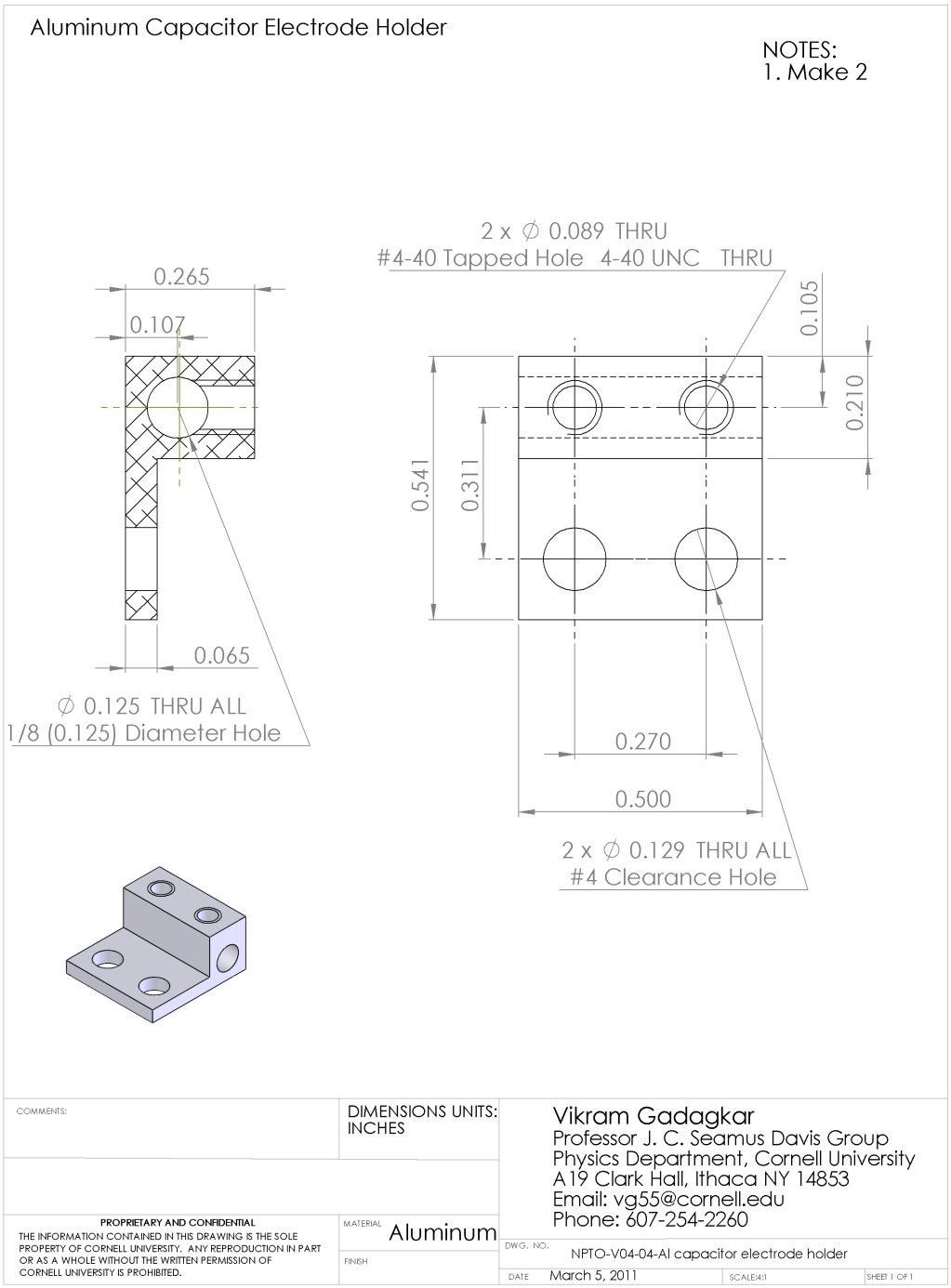

Figure C.13: Aluminum capacitor electrode holder. Two of these holders (for the drive and detect electrodes) are mounted on the aluminum platform. They contain the capacitor electrodes and keep the electrodes form moving with two screws.

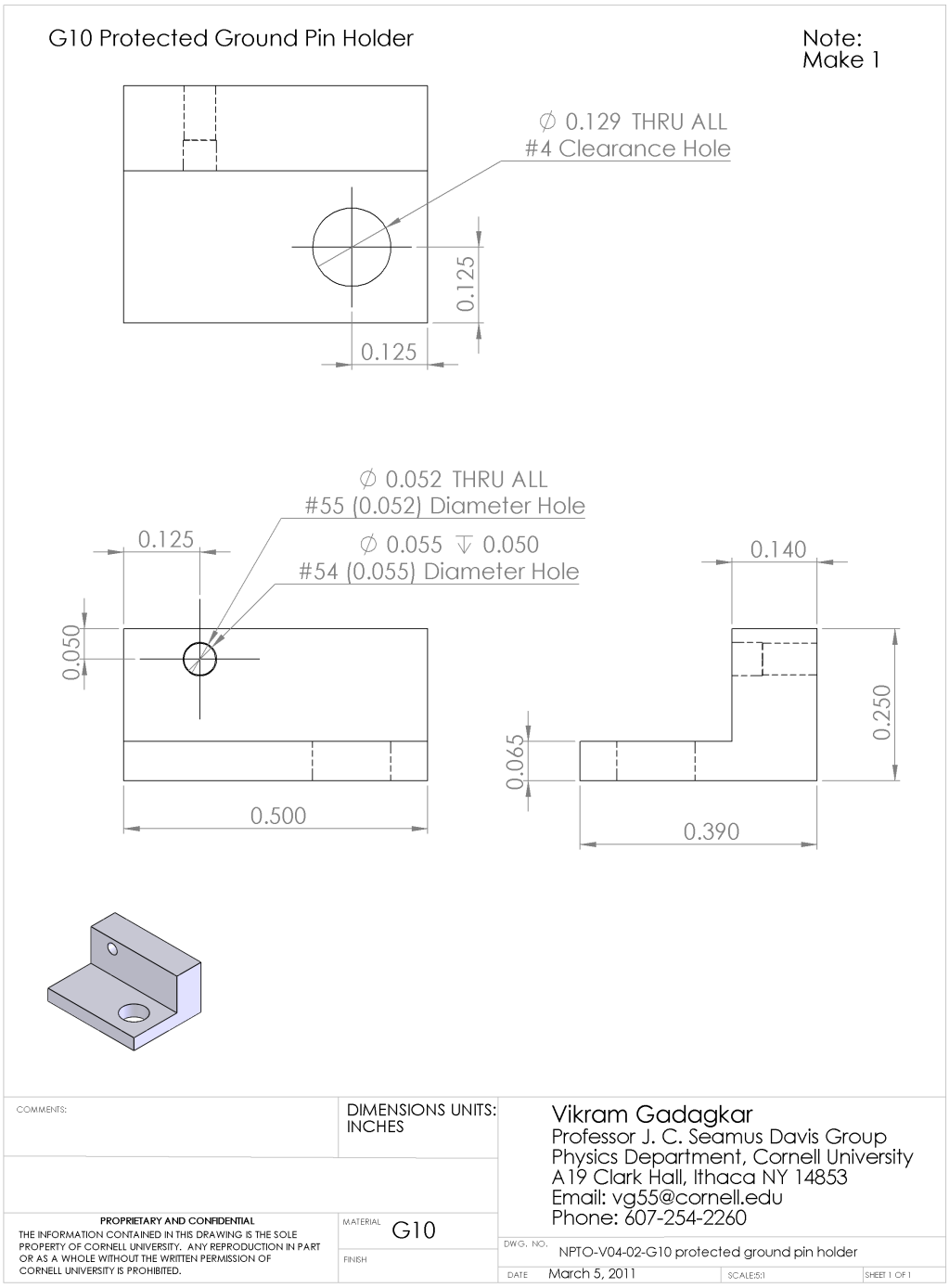

Figure C.14: G10 protected ground pin holder. This holder gets mounted on the aluminum electrode platform and holds a receptacle that accepts a pin to which one end of a thin gold wire is attached using silver epoxy. The other end of the wire is attached to the magnesium capacitor electrode plate on the torsional oscillator.

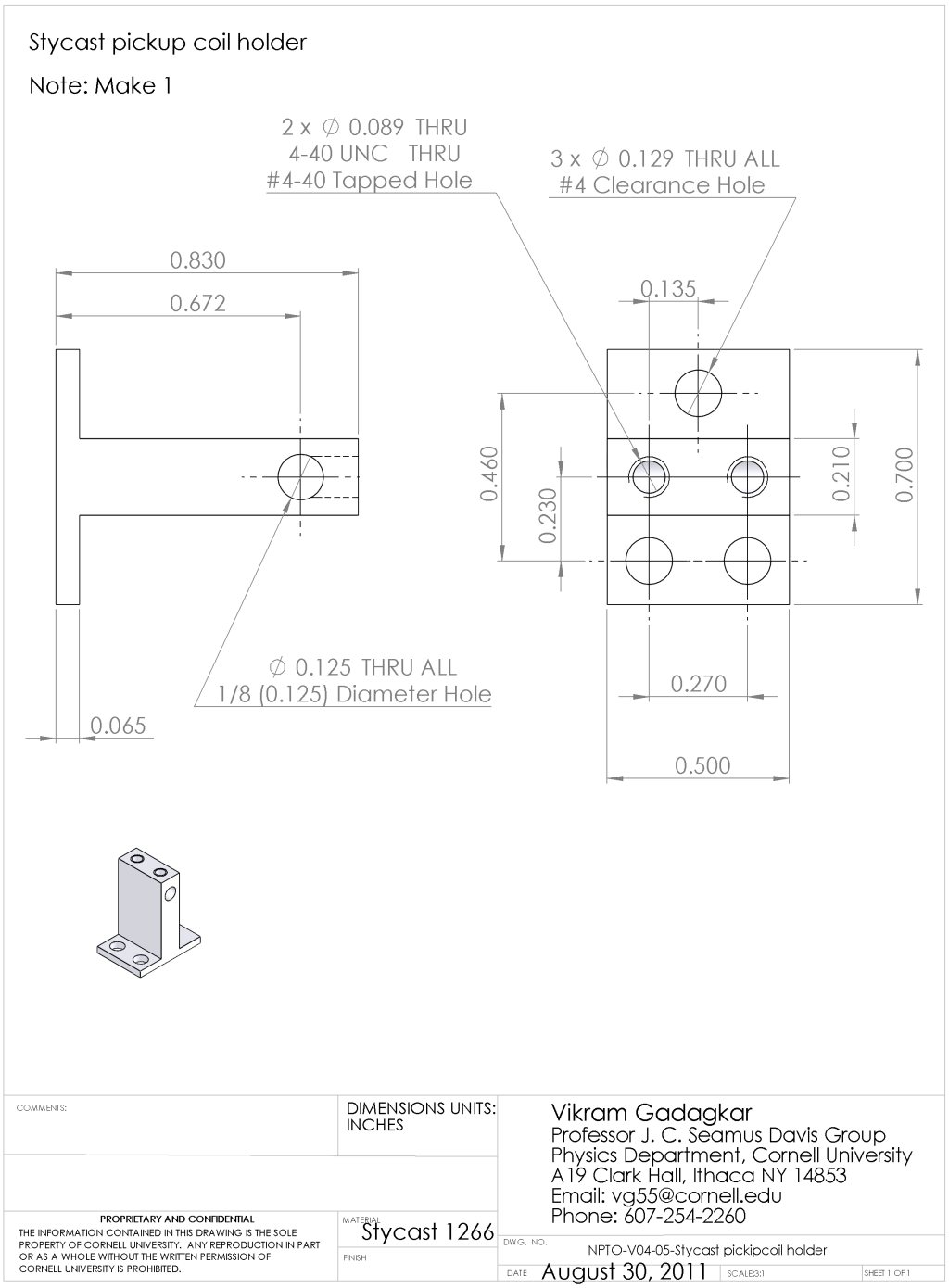

Figure C.15: Stycast SQUID pickup coil holder. This holder is mounted on the aluminum platform and holds the SQUID pickup coil used to detect changes in magnetic flux produced by the motion of the samarium cobalt magnet on the torsional oscillator.

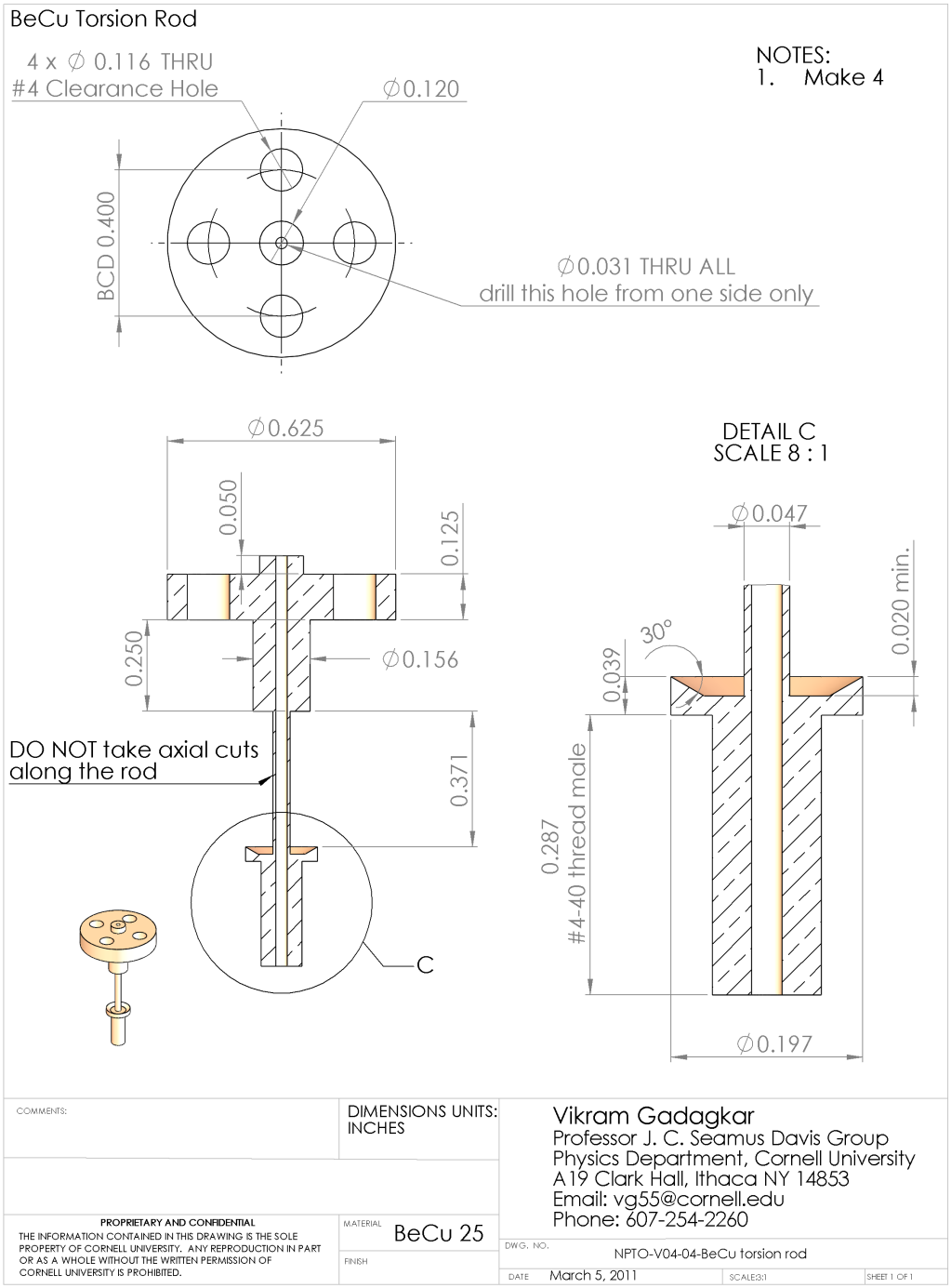

Figure C.16: Berrylium Copper torsion rod. The torsion rod provides the spring constant for the torsional oscillator. By being hollow, it also serves as the fill line for helium to enter the cell. The torsion rod needs to be carefully machined and subsequently annealed to have a high quality factor needed for our sensitive measurements.

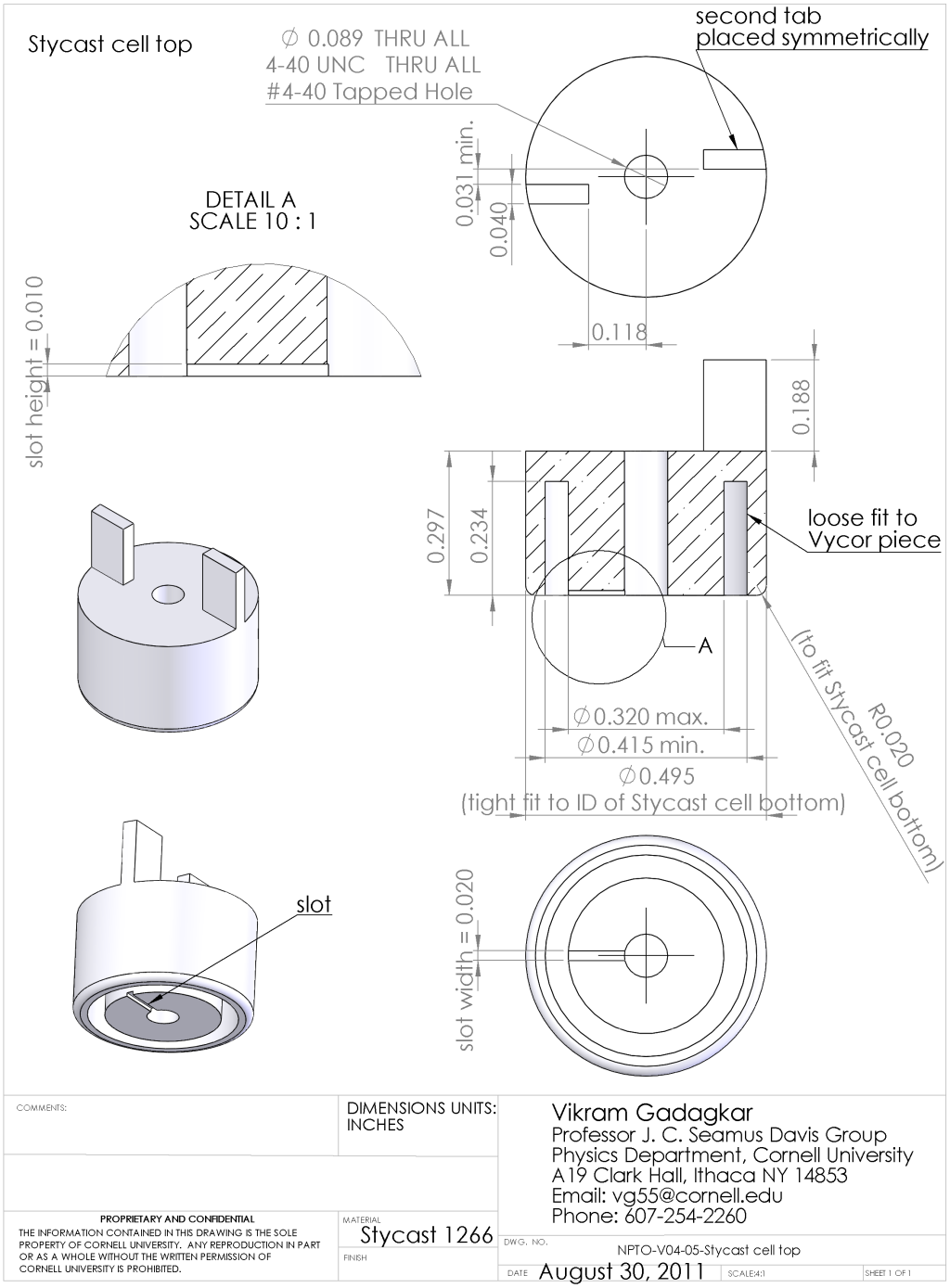

Figure C.17: Stycast cell top. This is top part of the cell. It has a hollow annular region in which the Vycor annulus sits. Note the two tabs on which the magnesium electrode place is glued and the slot through which helium enters the annular region.

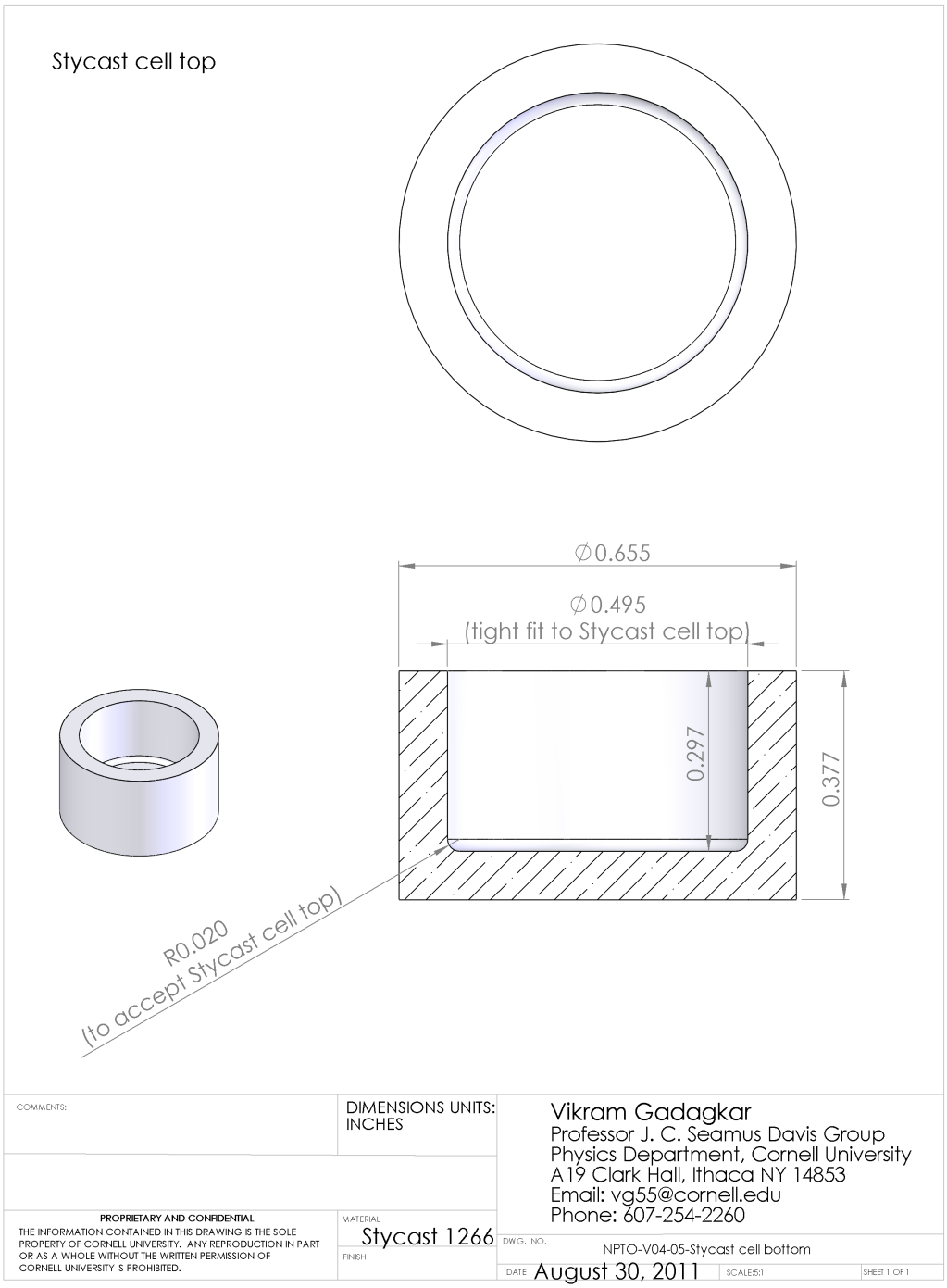

Figure C.18: Stycast cell bottom. This piece accepts the Stycast cell top. The two pieces are glued together with fresh Stycast.

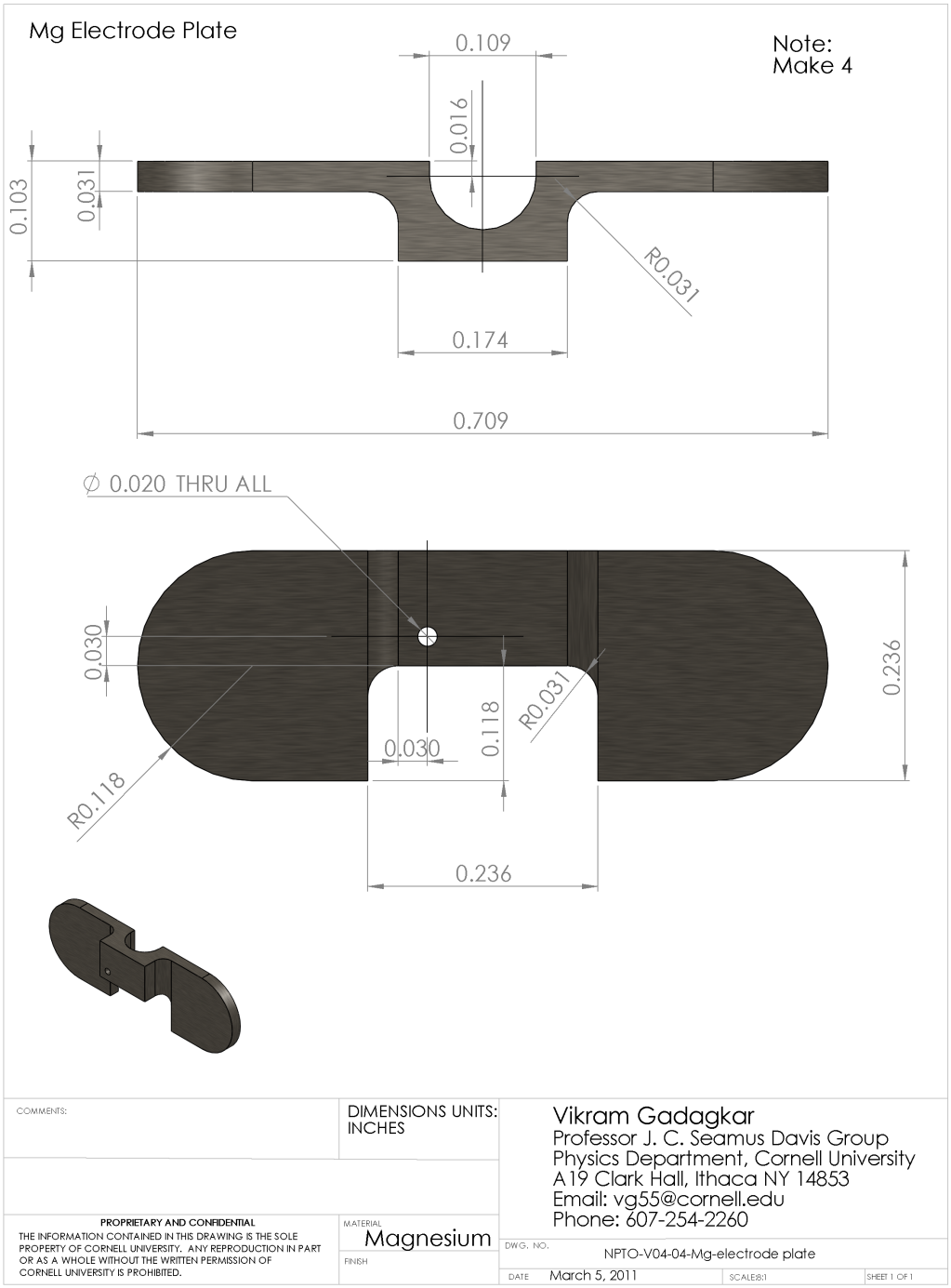

Figure C.19: Magnesium capacitor electrode plate. This piece acts as both the capacitive drive and detect electrodes. Magnesium was chosen for it's light weight and machinability. A thin gold wire is attached to the plate using silver epoxy. The wire then connect to a low temperature coax making the magnesium place the protected ground.

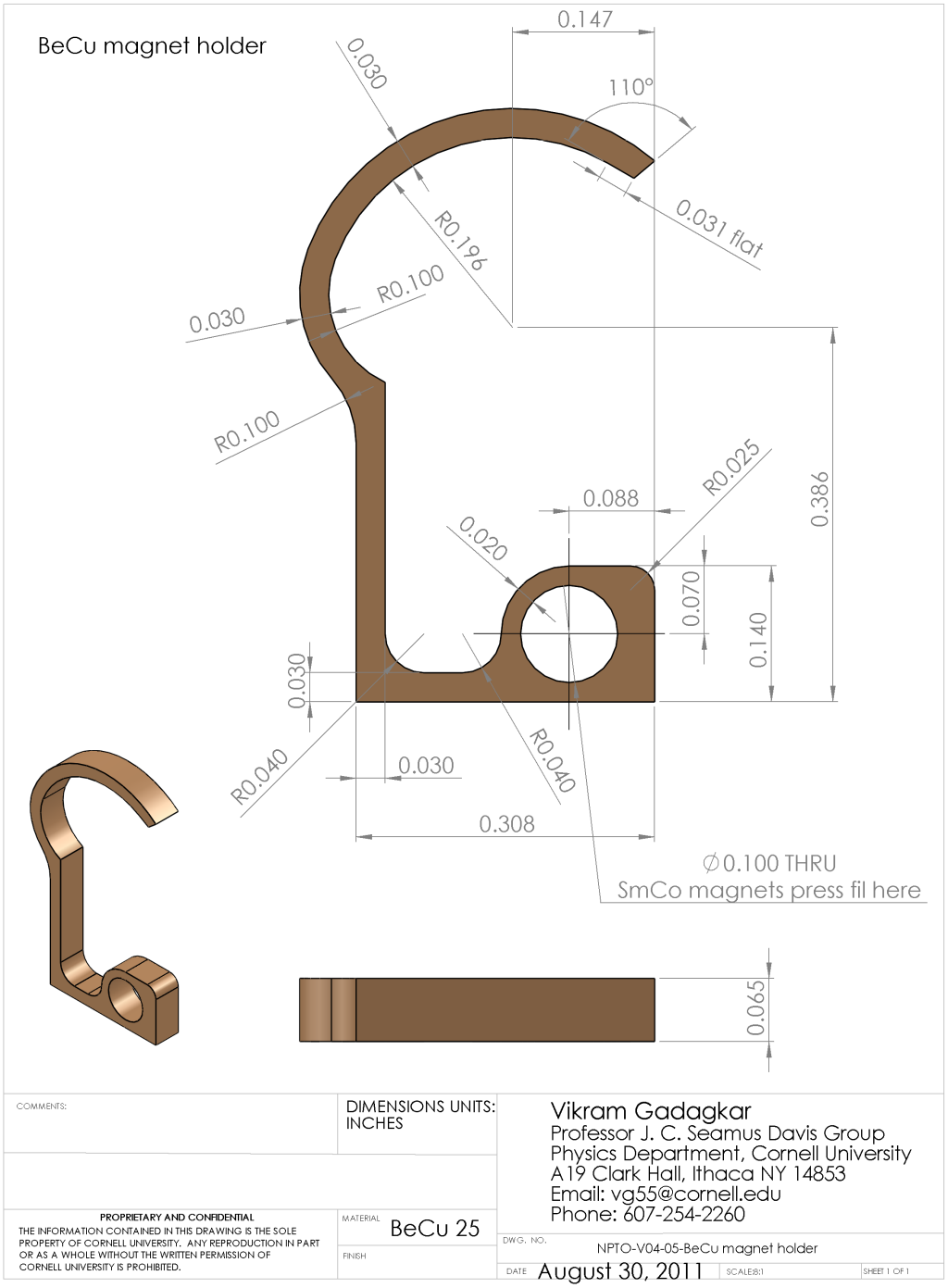

Figure C.20: Beryllium Copper magnet holder. This piece holds a samarium cobalt magnet used in the SQUID detection scheme. The holder is designed so that it can be clipped on to the torsional oscillator body and then glued in place by a drop of fresh Stycast. BeCu was chosen to that good thermal contact is maintained between the magnet and the torsion rod at all times.

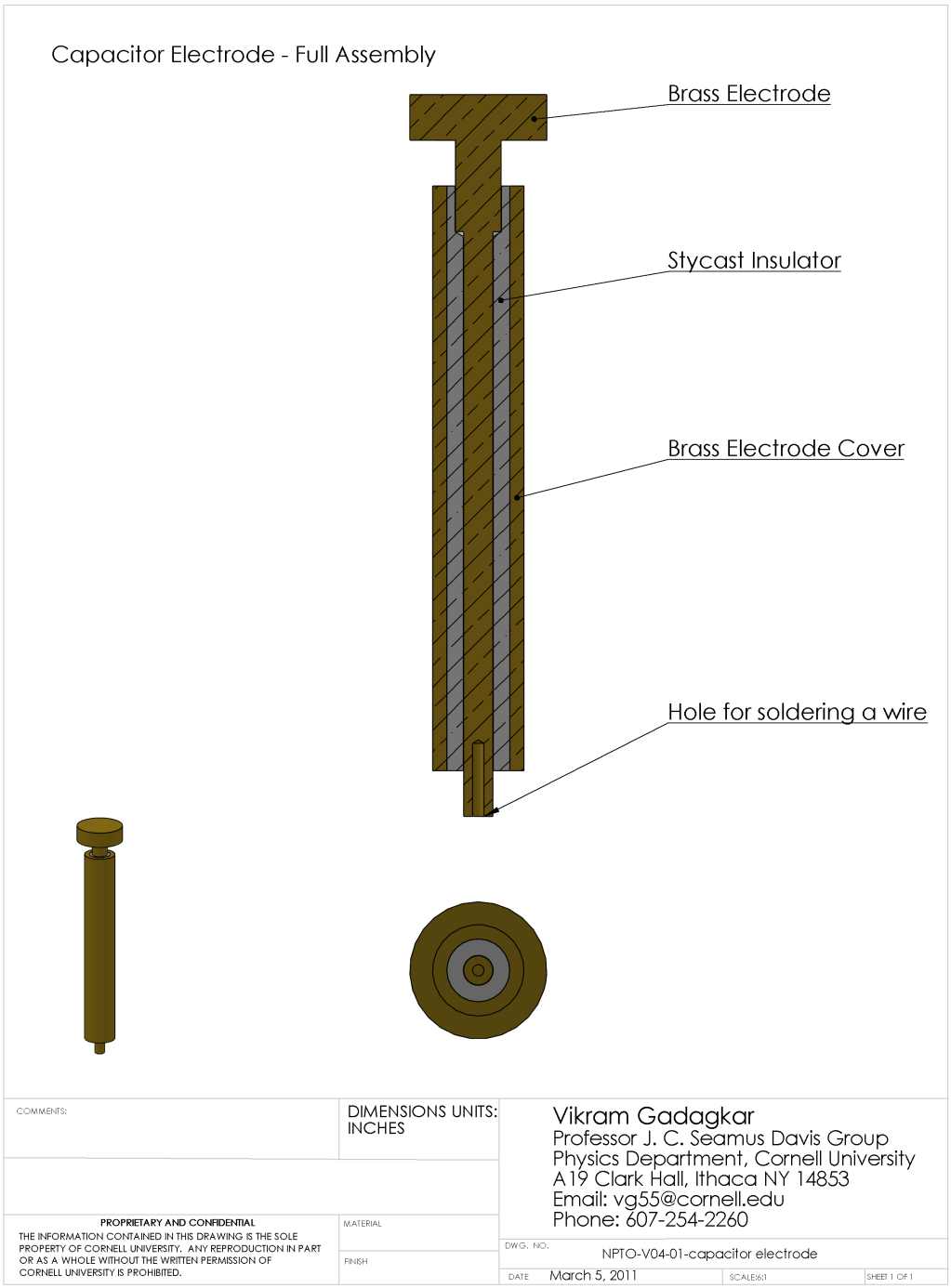

Figure C.21: The full assembly of the capacitor electrode. These electrodes, used for capacitively driving and detecting the motion of the torsional oscillator are held in place by the capacitor electrode holders.

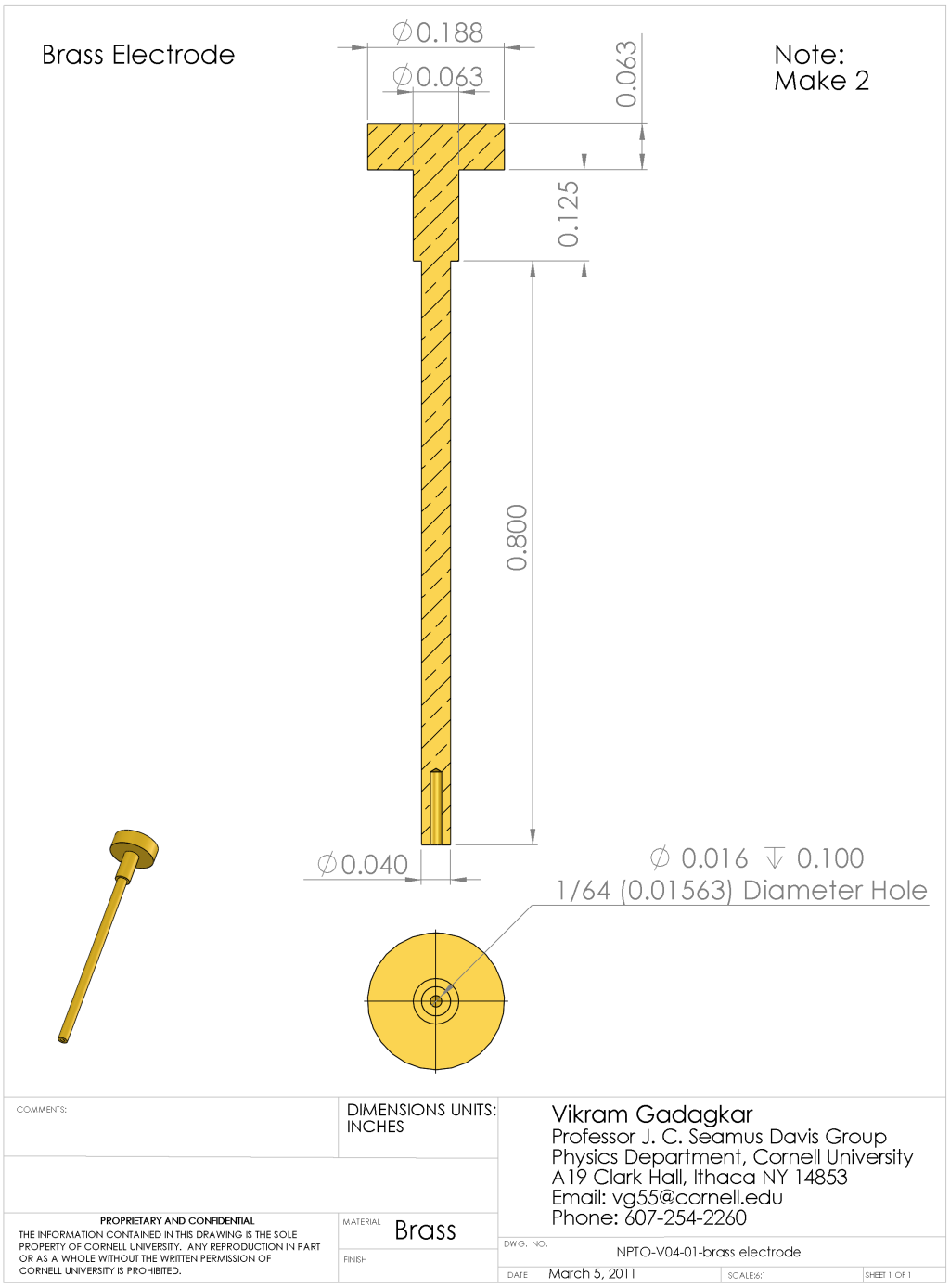

Figure C.22: Brass capacitor electrode. These electrodes are used for capacitively driving and detecting the torsional oscillator motion.

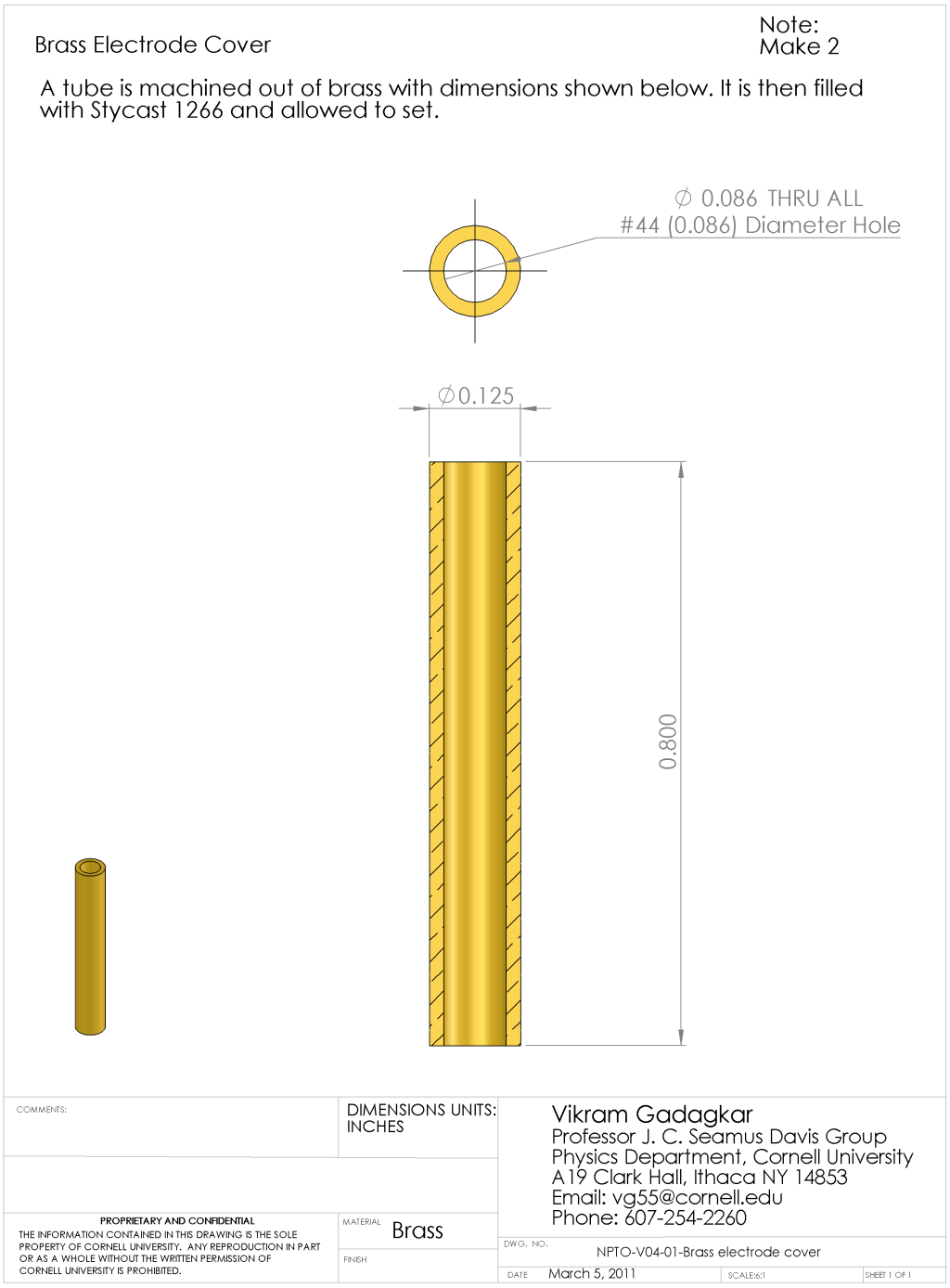

Figure C.23: Brass electrode shield. These tubes serve as shields for the capacitor electrodes.

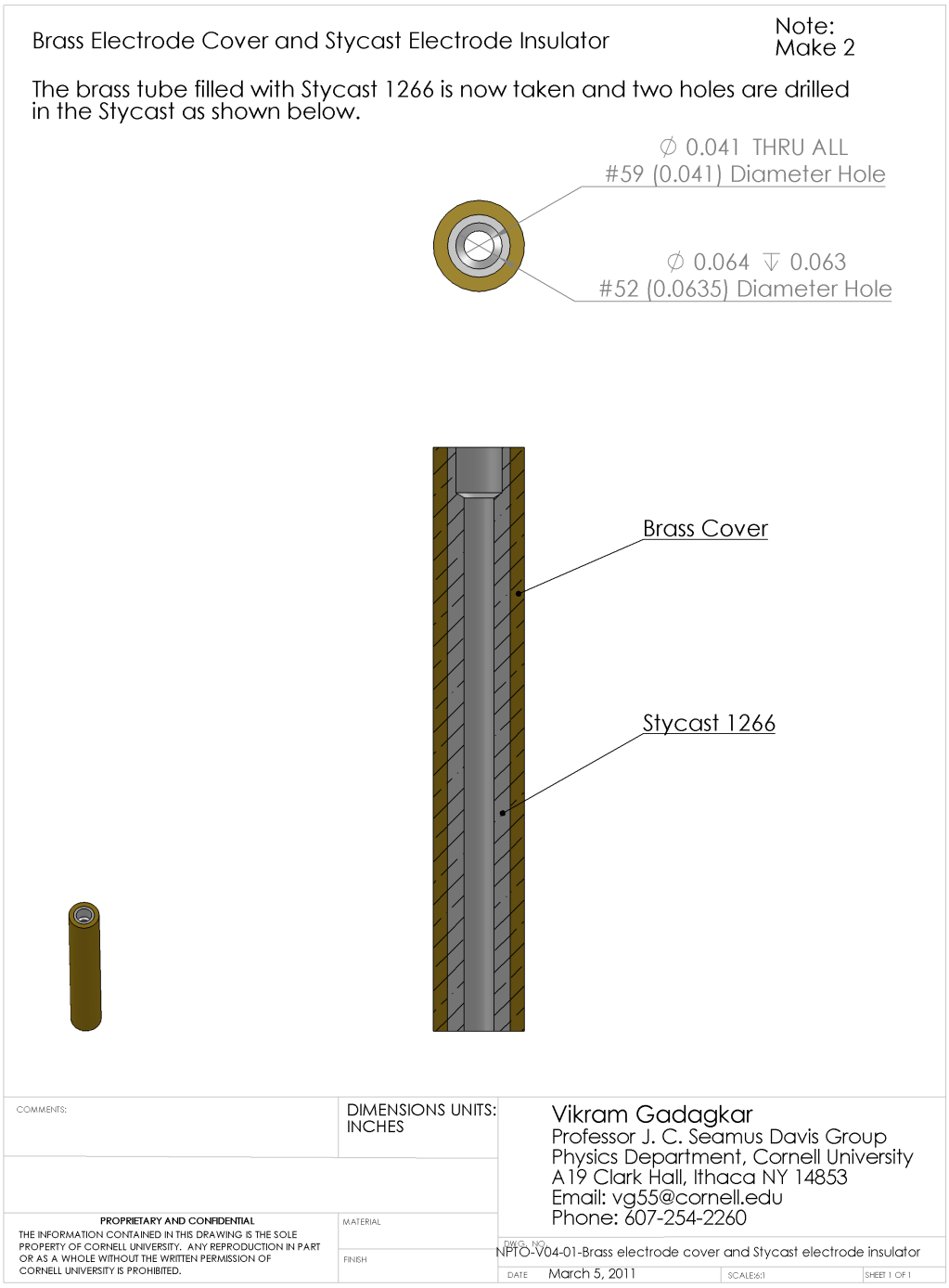

Figure C.24: The brass electrode shields shown in Figure C.23 are filled with Stycast 1266 and allowed to set. The Stycast 1266 is then machined to accept the brass capacitor electrodes shown in Figure C.22. The brass electrodes are glued in place with a thin layer of fresh Stycast 1266 to get the full assembly shown in Figure C.21.

APPENDIX D

VARIABLE-FREQUENCY TORSIONAL OSCILLATOR: A PROPOSAL

In this section, we briefly introduce the idea of the rotational susceptibility measured in a torsional oscillator and how changing the resonance frequency of a torsional oscillator would help test physical models for the underlying physics of solid helium. We then discuss the proposed mechanism to accomplish this followed by a study of some properties of such an oscillator and finally present the proposed design.

D.1 Linear Response and Rotational Susceptibility

The following discussion is based, in part, on Refs. [56, 63, 36]. In a rigorous sense, a torsional oscillator (TO) measures the rotational susceptibility to an external torque Γ_{ext}. The equation of motion for a TO can be written in the time domain as

$$\left(I_{TO}\frac{d^2}{dt^2} + \gamma_{TO}\frac{d}{dt} + K\right)\theta(t) = \Gamma_{ext}(t) + M(t) \tag{D.1}$$

where

$$M(t) \equiv \int g(t-t')\theta(t')dt' \tag{D.2}$$

for a linear system invariant under time translation. I_{TO} is the moment of inertia, γ_{TO} is the dissipation, and K is the torsion constant of the empty TO (all assumed to be temperature independent). Equation D.2 is called the back-action of the helium on the TO chassis (due to its finite shear modulus, the helium exerts a moment on the TO). The entire temperature dependence of the susceptibility is encapsulated in $g(t, T)$. The Fourier transform of Equation D.1 gives us

$$\theta(\omega) = \Gamma_{ext}(\omega)\chi(\omega) \tag{D.3}$$

where, the inverse susceptibility is

$$\chi^{-1}(\omega, T) = \chi_0^{-1}(\omega) - g(\omega, T) \tag{D.4}$$

and

$$\chi_0^{-1}(\omega) = -I_{TO}\omega^2 - \gamma_{TO}\omega + K \tag{D.5}$$

is the susceptibility (inverse) of the empty TO (assumed to be temperature independent). The helium's contribution to the susceptibility $g(\omega, T)$ can be further divided into a temperature-independent part $I_{He}\omega^2$ and a temperature-dependent part $\chi_g^{-1}(\omega, T)$, so that

$$g(\omega, T) = I_{He}\omega^2 + \chi_g^{-1}(\omega, T) \tag{D.6}$$

is model-dependent with different models trying to explain the physics of low-temperature solid helium predicting different $\chi_g^{-1}(\omega, T)$. The resonant frequency of the system at the lowest temperature is given by $\omega_0 = \sqrt{K/I}$, which is the resonance frequency of a perfectly rigid rotor with moment of inertia $I = I_0 + I_{He}$. The susceptibility of the bare oscillator, as given by Equation D.5, can easily be measured. Figure D.1 shows the modulus of such a measurement along with a $Q \sim 4 \times 10^6$ Lorentzian curve for reference. Also note that we neglect $\gamma_{TO} = I\omega_0 Q_\infty^{-1} = I\omega_0 D_\infty$ in the following discussion as its contribution to the resonance frequency is proportional to D_∞^2 which is of the order of 10^{-11}. The next step is to express the model-dependent susceptibility in terms of the measured properties of the oscillator. We will discuss only the case where the TO is operated on resonance.

D.2 Physical Models for the Inertial Transition

Since the discovery of the inertial anomaly by Kim and Chan in 2004 [45, 44], several classes of explanations for the solid helium rotational dynamics have been proposed. See section 2.1 for a discussion of these various models. Chapter 2 presents strong evidence that the physics of low-temperature solid helium is controlled, not by a superfluid T_c and V_c but by $\omega_0\tau = 1$ type phenomenology [64].

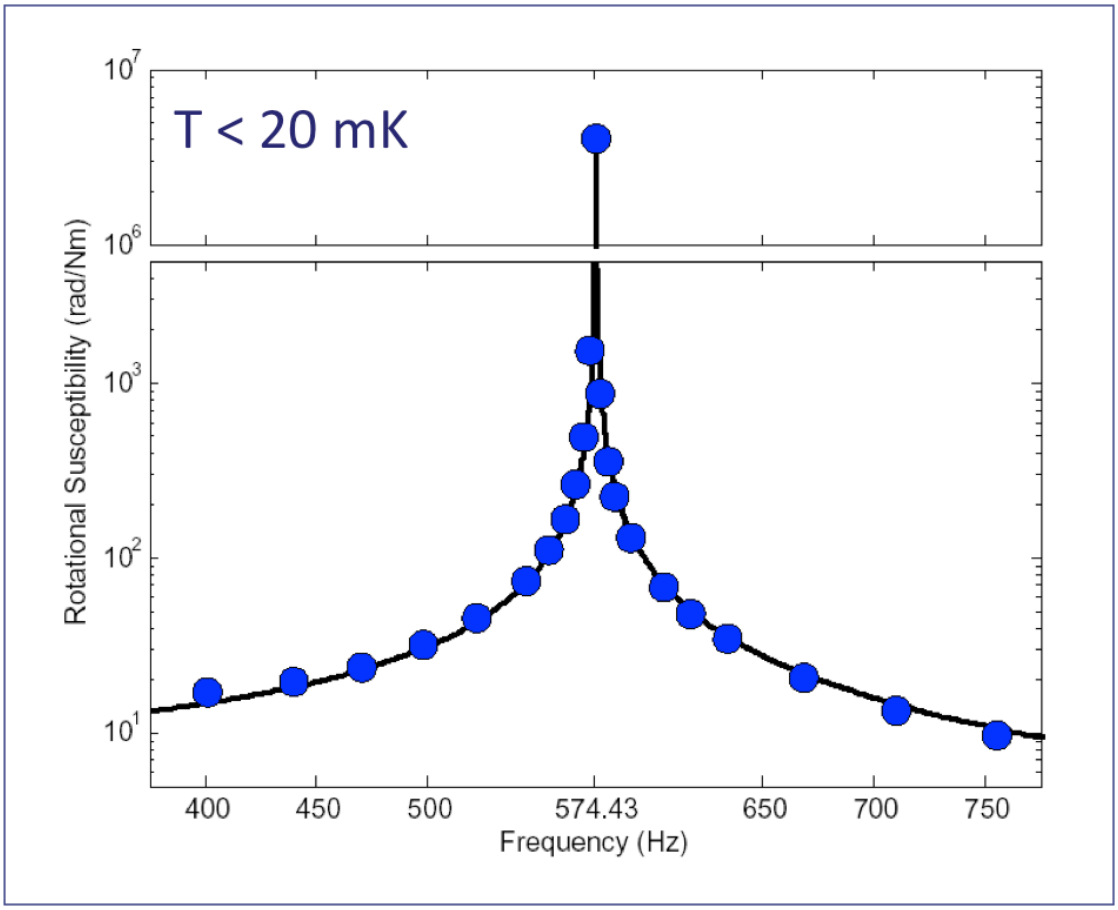

Figure D.1: Rotational susceptibility $\chi(\omega)$ of the TO-^{4}He system (blue dots). Error bars and temperature-dependent helium physics are smaller than the symbol size. The solid curve is the theoretical susceptibility of a $Q \sim 4 \times 10^6$ damped simple harmonic oscillator. Notice the high dynamic range of the measurement.

To further distinguish between the various models which fall within the broad category of $\omega_0\tau = 1$ phenomenology, we note that these models make different predictions for the frequency-dependent coupling of these modes to the oscillator. In addition, the frequency dependence of the transition itself is not understood. Therefore, we take the following approach. We leave the coupling as a measured parameter, to be determined by measuring the frequency-dependent rotational susceptibility.

Consider the following generalized form for the model-dependent back-action:

$$\chi_g^{-1}(T) = \frac{C_p \omega^p}{1 - i\omega\tau(T)} \tag{D.7}$$

Reference	Nussinov *et al.* [56]	Yoo and Dorsey [94]
Model	Debye Freeze-Out	Viscoelastic
p	0	4
$C_p\omega^p$	$\frac{g_0}{I_{eff}}$	$\frac{\rho_n}{\rho}R^2\left(\frac{I_{He}}{I_{osc}}\right)F\left(\frac{h}{R}\right)\omega^4$

Table D.1: Frequency-dependent models of the back-action (effect of helium on a TO).

where p is the undetermined parameter (frequency coupling to the oscillator). The total susceptibility can thus be written as

$$\frac{\chi^{-1}(T)}{I_{osc}} = \omega_0^2 - \omega^2 - i\frac{\omega_0\omega}{Q} - \frac{C_p\omega^p}{1 - i\omega\tau(T)} \tag{D.8}$$

For example, this form can be made consistent with the phenomenology of a Debye freeze-out ($p = 0$) transition [56] or a viscoelastic ($p = 4$) model [94]. Table D.1 shows p and $C_p\omega^p$ (in the notation of the references) for these two models. One can now also include (by hand, so to speak) the effect of a simple superfluid decoupling in addition to the effects of the overdamped internal dissipative degrees of freedom. A simple superfluid cannot account for a dissipation peak. Thus, the effect of adding a superfluid would be an additional contribution to the frequency shift. Choosing the superfluid term to be zero at low temperature (by convention), we may write

$$\frac{\chi^{-1}(T)}{I_{osc}(1 - \delta_{T\to 0})} = \omega_0^2 - [1 + \delta(T)]\omega^2 - i\frac{\omega_0\omega}{Q} - \frac{C_p\omega^p}{1 - i\omega\tau(T)} \tag{D.9}$$

where

$$\delta(T) = \frac{\rho_s(T)}{\rho}\frac{I_{He}}{I_{osc}} \tag{D.10}$$

Without knowing the detailed temperature-dependence of the model of interest, we may, however, expect the following temperature-dependent limits:

$$\delta(T) = \begin{cases} 0 & \text{for } T \to 0 \\ \frac{\rho_s^0}{rho}\frac{I_{He}}{I_{osc}} & \text{for } T \to \infty \end{cases} \qquad \omega\tau(T) \begin{cases} \gg 1 & \text{for } T \to 0 \\ = 1 & \text{for } T \to T^* \\ \ll 1 & \text{for } T \to \infty \end{cases} \tag{D.11}$$

Physically, this means is that at high temperatures, the superfluid saturates, increasing the oscillators inertia. Further, the dissipative relaxation times decrease, resulting in an

inertial transition at T^* (defined as the temperature at which the probe frequency is equal to the dissipation rate).

D.3 Frequency-Dependent Predictions

One way to study the frequency dependent properties is to measure the rotational susceptibility of the TO-helium system directly by operating the TO off-resonance. Unfortunately, however, we found that even with our highly sensitive SQUID-based TO, the change in χ due to the supersolid could not be resolved more than 50 Hz away from the resonant frequency ($\sim$ 574.475 Hz). This puts severe limits on the bandwidth (100 Hz) and consequently on the conclusions that can be drawn.

This forces us to always drive the oscillator at its resonance frequency. This method vastly increases the signal to noise ratio compared to direct measurement methods. The only way to study frequency-dependent effects, in that case, is to change the resonance frequency itself. This calls for a variable-frequency torsional oscillator (VFTO), a TO whose resonance frequency can be varied. Two important considerations for such an oscillator are that 1) the frequency needs to be changeable at low temperature (< 1 K) so that the process of changing the frequency does not irreversibly alter the helium crystal and 2) the range of frequencies needs to be sufficiently large, without compromising on the large Q, so we can make meaningful deductions.

In the next few sections, we present the properties and design of such an oscillator. Let us first consider the predictions for the measured Δf and ΔQ^{-1}, if the oscillator is locked on resonance. We start with the model described by Equations D.9 and D.10, and expand about the pole ω_0 to make prediction for the frequency shift and dissipation.

Expanding the susceptibility given by Equation D.9 by a complex perturbation about the resonance frequency ω_0, and ignoring the dissipation of the empty oscillator Q_{osc}^{-1}, we obtain

$$\frac{\chi^{-1}(T)|_{\omega_R}}{I_{osc}(1-\delta_{T\to 0})} = 0 = \omega_0^2 - [1+\delta(T)]\omega_R^2 - \frac{C_p\omega_R^p}{1-i\omega_R\tau(T)} \tag{D.12}$$

where $\omega_R = \omega_0[1+\varepsilon(T)]$ and $\varepsilon(T) = \Delta\omega(T)/\omega_0 - (i/2)\Delta Q^{-1}(T)$. Not writing the temperature dependence explicitly, Equation D.12 becomes

$$[1-(1+\delta)(1+\varepsilon^2)][1-i(1+\varepsilon)\omega_0\tau] = C_p\omega_0^{p-2}(1+\varepsilon)^p. \tag{D.13}$$

We can now find the complex frequency shift $\varepsilon(T)$ by neglecting terms quadratic or smaller in δ or ε and rearranging:

$$-2\varepsilon(T) = \delta(T) + C_p\omega_0^{p-2}\frac{1+i\omega_0\tau(T)}{1+\omega_0^2\tau^2(T)}. \tag{D.14}$$

It is now clear why a variable-frequency oscillator is essential. Since we do not know C_p independently, measurements at a single frequency ω_0 are insufficient to determine the type of dissipative physics controlling the dynamics in low-temperature solid helium. Measurements at several different ω_0 are thus required. To connect the result expressed in Equation D.14 to the actual observables of measurement, we can conveniently split it into the following conjugate parts:

$$-2\frac{\Delta\omega(T)}{\omega_0} = \delta(T) + \frac{C_p\omega_0^{p-2}}{1+\omega_0^2\tau^2(T)} \tag{D.15a}$$

$$\Delta Q^{-1}(T) = C_p\omega_0^{p-2}\frac{\omega_0\tau(T)}{1+\omega_0^2\tau^2(T)} \tag{D.15b}$$

Using Equation D.15, we can also immediately see what the saturated values of the frequency shift and the dissipation should be:

$$-\frac{\Delta\omega_{sat}}{\omega_0} = -\frac{\Delta\omega(T\to\infty)}{\omega_0} = \frac{1}{2}\left(\frac{\rho_s^0}{\rho}\right)\frac{I_{He}}{I_{osc}} + \frac{C_p}{2}\omega_0^{p-2} \tag{D.16a}$$

$$\Delta Q_{peak}^{-1} = \Delta Q^{-1}(T^*) = \left(\frac{1}{2*\omega_0^2}\right)C_p\omega_0^p \tag{D.16b}$$

By measuring these quantities at various resonance frequencies, valuable information about the physics governing the dynamics of solid helium can be obtained, taking us closer to solving this complex mystery. The next section describes how such a variable-frequency torsion oscillator might be practically constructed.

D.4 The Proposed Mechanism for Changing the Frequency

The resonant frequency of a torsion oscillator is given by

$$f = \frac{1}{2\pi}\sqrt{\frac{K}{I}} \tag{D.17}$$

where K is the torsion constant and I is the moment of inertia. Therefore, the two obvious ways of changing the resonance frequency are to either change the torsion constant or vary the moment of inertia. As discussed above, we are constrained to change the frequency at low temperature to preserve the solid sample and further obtain a sufficiently wide range of frequencies.

There are room temperature torsion oscillators whose frequencies are varied by moving masses radially outward from the torsion rod, thereby changing the moment of inertia. While this operation is relatively simple to perform on a big oscillator sitting on a table at room temperature, its extremely challenging at millikelvin temperatures deep inside a dilution refrigerator. We choose to focus, instead, on changing the torsion spring constant.

The torsion constant of a torsion oscillator is given by [72]

$$K = \frac{\pi G a^4}{32L} \tag{D.18}$$

where G is the shear modulus, a is the diameter, and L is the length of the torsion rod.

This motivates the idea of varying the spring constant (and hence the frequency) of the TO by changing the effective length of the torsion rod. We propose making the torsion rod triangular in cross section and varying the active length by sliding up and down over it a tight-fitting sleeve with a triangular hole.

The next question is how to move, from outside, the sleeve up and down deep inside a dilution refrigerator. We propose an actuation mechanism that involves the expansion and contraction of a pair of concentric bellows. The space between the bellows is filled with liquid ^{4}He through a fill line, which comes all the way out of the cryostat and connects to a room temperature pressure reservoir. By increasing (decreasing) the pressure in the room temperature reservoir, the bellows can be expanded (contracted), thus moving the sleeve down (up). Detailed drawings of the variable-frequency torsion oscillator are shown in a later section below.

We propose that the torsion rod be made of beryllium copper (BeCu) to achieve a high Q and the sleeve have sheets of sapphire, which make contact with the rod. Highly polished sapphire on polished BeCu can slide with minimal friction while applying a large normal force.

D.5 Design and Specifications

This section presents the designs and specifications of the various parts of the proposed variable-frequency torsion oscillator (VFTO).

D.5.1 Frequency Range

We begin with a rough estimate of the frequency range we might expect by varying the length of a torsional oscillator. For simplicity, we assume that the torsion rod is a uniform cylinder of Beryllium-Copper (BeCu) and that the cell is a uniform cylinder of Stycast 1266 (we will later modify the torsion rod to have a triangular cross-section and a fill line, and the cell will have a cavity to hold helium, in addition to ears for the drive and detect electrodes and the magnets for the SQUID and so on). The diameter of the torsion rod, as well as the radius and height of the cell are chosen, for this estimate, to be similar to the single-frequency torsion oscillator we have successfully used in our laboratory. Although we are concerned with the torsion mode of the TO, we need to consider the frequencies of the other modes, especially the floppy mode (a motion similar to that of a simple pendulum). For a successful measurement, the frequencies of the torsion mode and the floppy mode should not be too close to each other.

As discussed above, the frequency of either the torsion mode or the floppy mode is given by Equation D.17. The spring constants and the moments of inertia for the two modes [72] are given below.

Torsion Mode:

$$I = \frac{1}{2}(\rho\pi r^2 h)r^2 \tag{D.19a}$$

$$K = \frac{\pi G a^4}{32L} \tag{D.19b}$$

Floppy Mode:

$$I = (\rho\pi r^2 h)\left[\left(L + \frac{h}{2}\right)^2 + \frac{r^2}{4} + \frac{h^2}{12}\right] \tag{D.20a}$$

$$K = \frac{3\pi E a^4}{64L} \tag{D.20b}$$

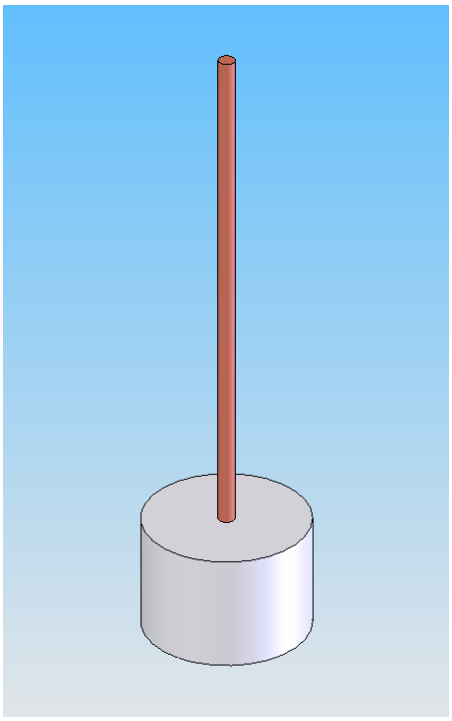

Figure D.2: A schematic (to scale with the parameters given above) of the torsion oscillator (BeCu rod and Stycast cell) used for the estimate of the frequency range.

where, r is the radius of the cell (5 mm), h is the height of the cell (7 mm), ρ is the density of the cell material (1180 kgm^{-3}), a is the diameter of the rod (1 mm), L is the length of the rod (variable), G is the shear modulus of the rod material (5.3×10^{10} Nm^{-2}), and E is the Young's modulus of the rod material (1.31×10^{11} Nm^{-2}).

Figure D.2 is a schematic of the torsional oscillator used to make the estimates. It consists of a BeCu torsion rod and a Stycast 1266 cell. It is drawn to scale corresponding to the parameter values given above. The length of the torsion rod is 31 mm. Using Equations D.17, D.19, and D.20, we can calculate the frequencies of the torsion and floppy modes as a function of the free length (Figure D.3). We see that the torsion mode frequency varies by a factor of ~ 5 when the length is changed by 3 cm.

Clearly, in the region where the floppy mode frequency matches that of the torsion mode, we have a problem. We would like the difference between the two mode fre-

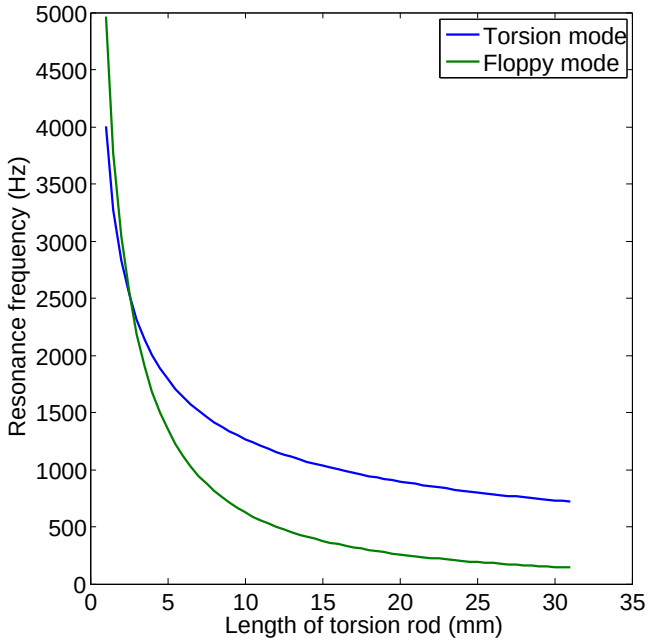

Figure D.3: Torsion and floppy mode frequencies as a function of rod length for the torsional oscillator shown in Figure D.2. The torsion mode frequency varies by a factor of ~5 over a length of 3 cm.

quencies to be at least 100 Hz. Figure D.4 shows the difference between the torsion and floppy mode frequencies as a function of torsion rod length and highlights the region where the absolute value of the difference is less than or equal to 100 Hz. This corresponds to a range of about 300 Hz in the torsion frequency between 2352 Hz and 2659 Hz. This is less than 10% of the entire torsional frequency range.

It is important to note that the estimates presented here are rough and will not exactly correspond to the actual variable-frequency torsion oscillator. The torsion rod will be of a triangular cross-section, the cell will have cavities and ears and so on. By changing the parameters used in the estimate, it is possible to play around with the torsional and floppy mode frequencies if desired.

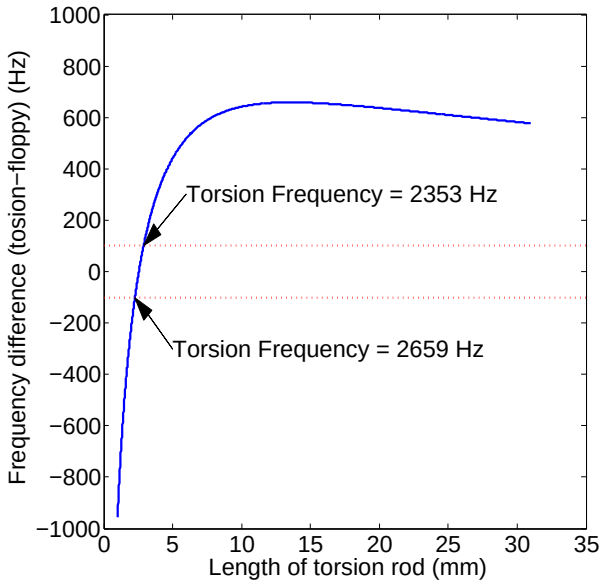

Figure D.4: The frequency difference between the torsion and floppy modes as a function of the length of the torsion rod. The region where the absolute value of the difference is less than or equal to 100 Hz corresponds to torsion frequencies between 2353 Hz and 2659 Hz (~300 Hz).

D.5.2 Frequency Change and Resolution

The resonance frequency of a high Q torsional oscillator is given by Equation D.17. The angular amplitude of such an oscillator is given by

$$|A(\omega_0)| = \frac{\Gamma_{ext} Q}{I\omega_0^2} \tag{D.21}$$

where Γ_{ext} is the applied external torque and I is the moment of inertia. The frequency resolution is then

$$\frac{\delta\omega_0}{\omega_0} \sim Q^{-1} \sim \frac{-2\delta I}{I_0} \tag{D.22}$$

This is the reason we demand such high Q oscillators for these studies (typically 10^6 at low temperatures). Thus we get a frequency resolution of ~1 ppm.

The next question we ask is: what is the change in the resonance frequency of the VFTO due to the supersolid transition? If one assumes that all the change in the fre-

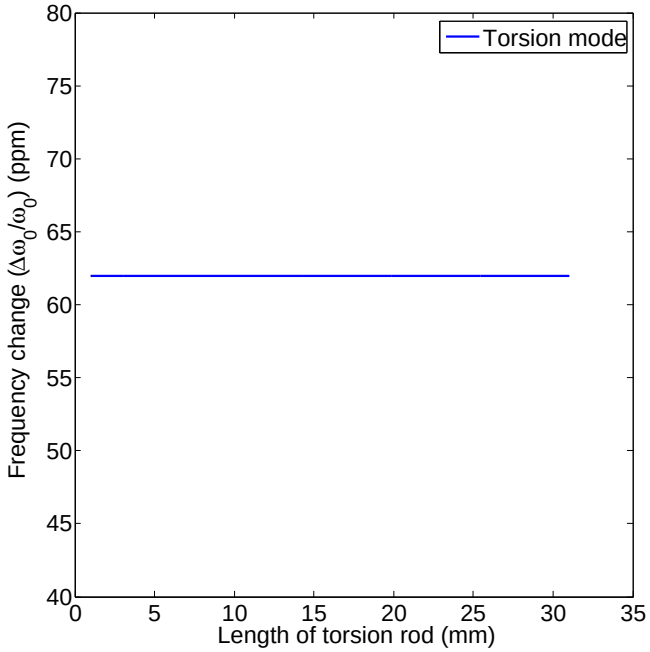

Figure D.5: Frequency change (in ppm) as a function of the length of the torsion rod assuming a 1% effective decoupling. The solid helium is modeled as a 100 micron wide annular cavity whose radius and height are the same as that of the cell shown in Figure D.2

quency of the TO is due to mass decoupling, then the observed change in moment of inertia of the helium as a result of the transition varies widely from 0.01 – 20% [12] depending on the sample quality. In our group we have found this number to be about 5% [37]. Let us assume that the solid helium occupies a 100 micron wide annular cavity whose radius and height are the same as that of the cell shown in Figure D.2 This is a very good approximation to the TO in previously used in our lab [37, 64]. Assuming a conservative 1% change in the effective moment of inertia of the solid helium after the 'supersolid' transition, we can estimate the frequency change (Equation D.22) as a function of the torsion rod length (Figure D.5).

We see that the relative frequency change is independent of torsion frequency (or rod length) and is about 62 ppm. This is much higher than the estimated resolution of 1 ppm (assuming $Q \sim 10^6$). We note that there will probably be a loss in Q due to the clamping mechanism discussed below. The estimate made above indicates that we might be able

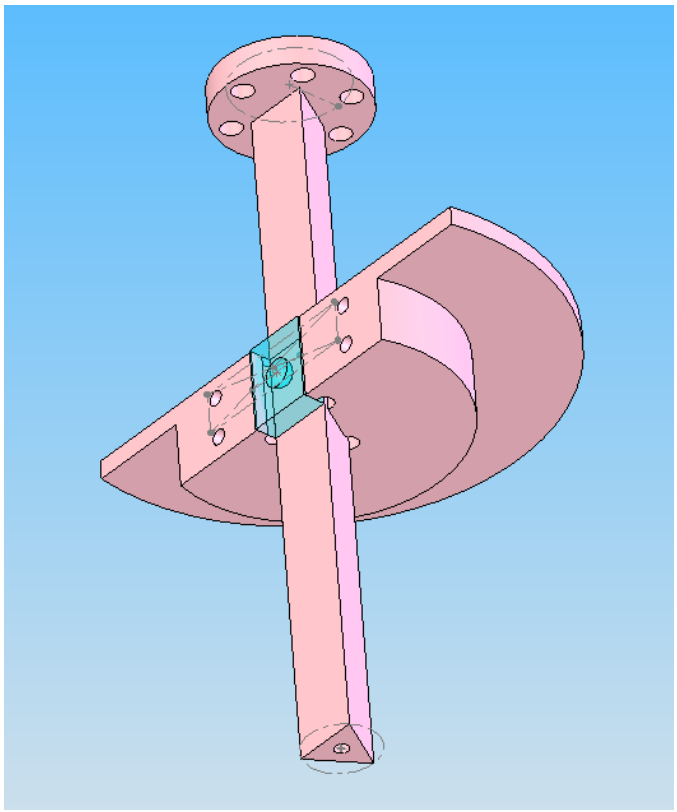

Figure D.6: The clamping mechanism. A triangular torsion rod sits in a V-shaped hole in a half-sleeve making contract on two sides. A third piece (sapphire) presses on the third side. Sapphire plates may be added on the other two sides as well in the next iteration of the design. The sleeve clamps the rod such that only the part of the rod below the clamp is free to rotate, effectively changing the length of the torsion rod and thereby changing the resonance frequency of oscillation. Note that the sleeve needs to be restricted from oscillating itself. This is accomplished by guide rods (discussed later). The cell is not shown.

to have enough signal to noise even if we lose Q by a factor of ~5.

D.5.3 Clamping Mechanism

Since we propose to vary the frequency of the torsional oscillator by changing the free length of the torsion rod, we need a very good clamping mechanism. There are three issues that need to be considered:

1. The torsion rod needs to be clamped well enough that the clamp effectively con-

strains the motion of the rod thereby reducing the free length.

2. The clamp should have the least effect on the Q of the oscillator.
3. The friction between the clamp and the torsion rod needs to be as small as possible to prevent excessive heating while the clamp is being moved (an alternative solution is to devise a mechanism by which we can unclamp, move and re-clamp).

To achieve the above criteria, we first modify the torsion rod to have a triangular cross-section instead of the traditional circular cross-section. The triangular torsion rod sits in a V-shaped hole in a half-sleeve. Finally a third piece pushes on the rod from the third side. In this way, we apply a uniform force from all three sides on the torsion rod. For the materials used in the clamping mechanism, we borrow technology used in clamping the scanning tunneling microscope (STM) head in our laboratories. The torsion rod needs to be highly polished and is designed to slide on highly polished sapphire plates. Note that the sleeve needs to be restricted from oscillating itself. This is accomplished by guide rods (discussed later). All this is shown in Figure D.6.

D.5.4 Clamp Motion—the Bellows Assembly

The next step is to devise a mechanism by which the clamp sleeve may be moved up and down. This is accomplished by a flexible bellows assembly, involving two concentric bellows enclosing a closed volume between them. The enclosed volume is filled with liquid helium through a fill line that goes all the way to a pressure reservoir at room temperature outside the cryostat. By carefully changing the pressure in the reservoir, the pressure inside the bellow can be changed leading to precise control over the expansion or contraction of the bellows. If the sleeve is attached to the bellows, the sleeve can be

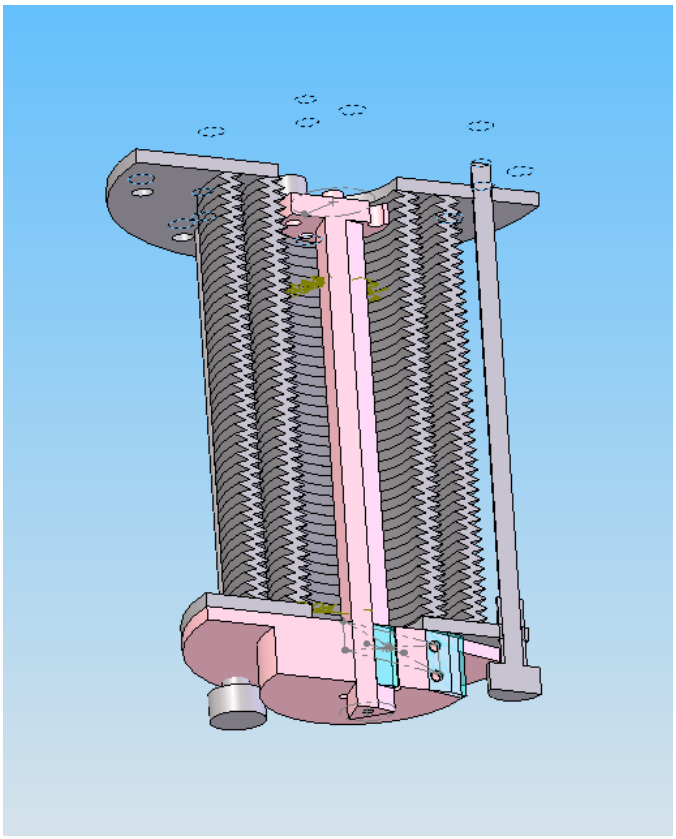

Figure D.7: The bellows assembly. The space between two concentric bellows is filled with helium. By varying the pressure of this helium, the bellows can be expanded or contracted to move the sleeve up and down the torsion rod. The cell is not shown.

moved up or down, thereby changing the free length of the torsion rod. The bellows assembly is shown in Figure D.7.

D.5.5 The Full Design

The latest design of the variable-frequency torsion oscillator (VFTO) is presented here. The design is not ready to be sent for machining yet. Several aspects (especially the cell) still need to be worked on and finalized. However, most of the basic parts are in place. Figure D.8 presents the current state of the VFTO design.

The following are some of what remains to be done:

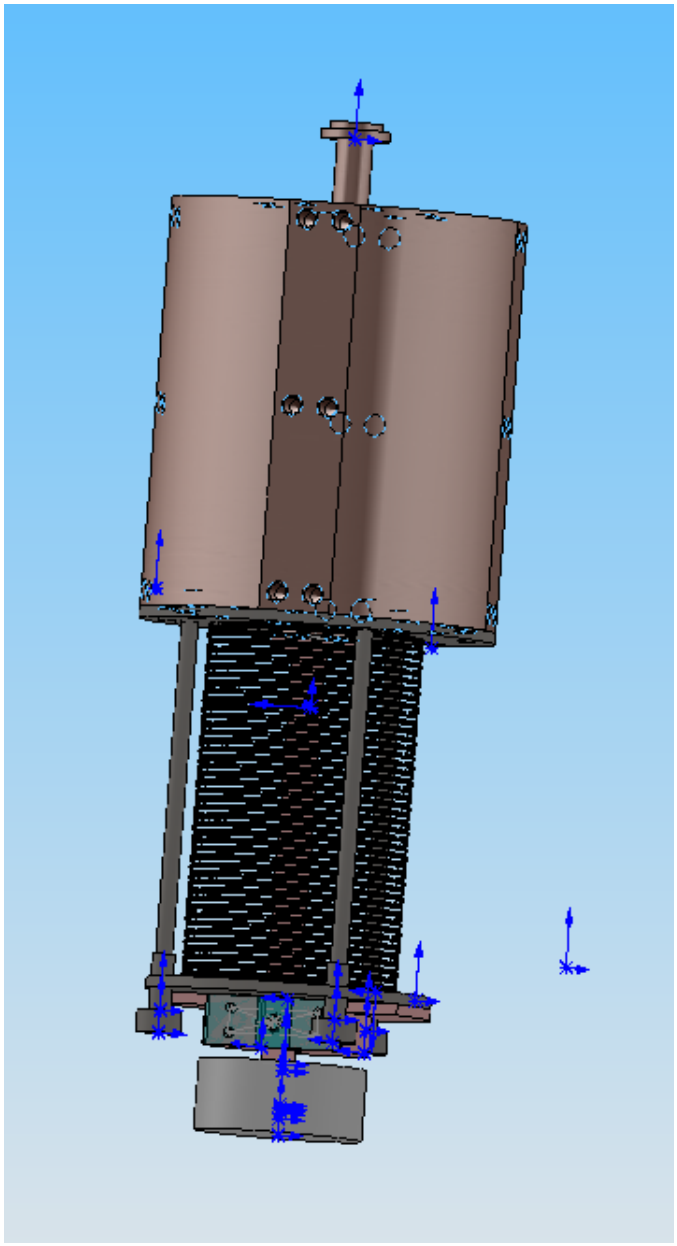

Figure D.8: The full VFTO design. Notice the big copper vibration isolation block that the whole assembly is mounted on.

1. Design the cell (with cavities, ears, magnets, etc.). BeCu and Stycast are two options.
2. More work remains to be done on the clamping assembly with regard to the sapphire plates. Include sapphire plates on the other two sides of the torsion rod as well. Consider designing a mechanism by which the rod can be unclamped, moved, and re-clamped (if heating becomes an issue).
3. All the dimensions have to be carefully looked at once again, including making them all compatible with the space inside the vacuum can in the cryostat.

BIBLIOGRAPHY

[1] A. D. Allen, J. F.; Misener. Flow of liquid helium II. *Nature*, 141:75, 1938.

[2] Vinay Ambegaokar, B. I. Halperin, David R. Nelson, and Eric D. Siggia. Dynamics of superfluid films. *Physical Review B*, 21(5):1806, 1980.

[3] M. H. Anderson, J. R. Ensher, M. R. Matthews, C. E. Wieman, and E. Cornell. Observation of Bose-Einstein condensation in a dilute atomic vapour. *Science*, 269:198–201, 1995.

[4] P. W. Anderson. Two new vortex liquids. *Nature Physics*, 3(3):160–162, 2007.

[5] P. W. Anderson. Bose fluids above T_c: Incompressible vortex fluids and "supersolidity". *Physical Review Letters*, 100(21):215301, 2008.

[6] Philip W. Anderson. A Gross-Pitaevskii treatment for supersolid helium. *Science*, 324(5927):631–632, 2009.

[7] A. F. Andreev. Supersolidity of glasses. *Jetp Letters*, 85(11):585–587, 2007.

[8] A. F. Andreev and I. M. Lifshitz. Quantum theory of defects in crystals. *Soviet Physics Jetp-Ussr*, 29(6):1107, 1969.

[9] Y. Aoki, J. Graves, and H. Kojima. Oscillation frequency dependence of nonclassical rotation inertia of solid He-4. *Physical Review Letters*, 99(1):015301, 2007.

[10] Y. Aoki, M. C. Keiderling, and H. Kojima. New dissipation relaxation phenomenon in oscillating solid He-4. *Physical Review Letters*, 100(21):215303, 2008.

[11] A. V. Balatsky, M. J. Graf, Z. Nussinov, and S. A. Trugman. Entropy of solid He-4: The possible role of a dislocation-induced glass. *Physical Review B*, 75(9):094201, 2007.

[12] S. Balibar. The enigma of supersolidity. *Nature*, 464(7286):176–182, 2010.

[13] J. R. Beamish, A. D. Fefferman, A. Haziot, X. Rojas, and S. Balibar. Elastic effects in torsional oscillators containing solid helium. *Physical Review B*, 85(18):180501, 2012.

[14] G. Biroli, C. Chamon, and F. Zamponi. Theory of the superglass phase. *Physical Review B*, 78(22):224306, 2008.

[15] D. J. Bishop and J. D. Reppy. Study of the superfluid transition in two-dimensional He-4 films. *Physical Review Letters*, 40(26):1727, 1978.

[16] M. Boninsegni, A. B. Kuklov, L. Pollet, N. V. Prokof'ev, B. V. Svistunov, and M. Troyer. Fate of vacancy-induced supersolidity in He-4. *Physical Review Letters*, 97(8):080401, 2006.

[17] M. Boninsegni, A. B. Kuklov, L. Pollet, N. V. Prokof'ev, B. V. Svistunov, and M. Troyer. Luttinger liquid in the core of a screw dislocation in helium-4. *Physical Review Letters*, 99(3):035301, 2007.

[18] J. Bossy, J. V. Pearce, H. Schober, and H. R. Glyde. Excitations of nanoscale quantum liquids under pressure and the Bose glass phase. *Physical Review B*, 78(22):224507, 2008.

[19] D. M. Ceperley and B. Bernu. Ring exchanges and the supersolid phase of He-4. *Physical Review Letters*, 93(15):155303, 2004.

[20] G. V. Chester. Speculations on Bose-Einstein condensation and quantum crystals. *Physical Review A*, 2(1):256, 1970.

[21] H. Choi, S. Kwon, D. Y. Kim, and E. Kim. Observation of hidden phases in supersolid He-4. *Nature Physics*, 6(6):424–427, 2010.

[22] A. Clark, J. West, and M. Chan. Nonclassical rotational inertia in helium crystals. *Physical Review Letters*, 99(13):135302, 2007.

[23] A. C. Clark, J. D. Maynard, and M. H. W. Chan. Thermal history of solid He-4 under oscillation. *Physical Review B*, 77(18):184513, 2008.

[24] A. Clarke, J.; Braginski. *The SQUID Handbook*, volume 1. Wiley-VCH, 2004.

[25] Kenneth S. Cole and Robert H. Cole. Dispersion and absorption in dielectrics I. alternating current characteristics. *The Journal of Chemical Physics*, 9(4):341, 1941.

[26] D. W. Davidson and R. H. Cole. Dielectric relaxation in glycerol, propylene glycol, and n-propanol. *The Journal of Chemical Physics*, 19(12):1484, 1951.

[27] J. Day and J. Beamish. Pressure-driven flow of solid helium. *Physical Review Letters*, 96(10):105304, 2006.

[28] J. Day and J. Beamish. Low-temperature shear modulus changes in solid He-4 and connection to supersolidity. *Nature*, 450(7171):853–856, 2007.

[29] J. Day, O. Syshchenko, and J. Beamish. Nonlinear elastic response in solid helium: Critical velocity or strain? *Physical Review Letters*, 104(7):075302, 2010.

[30] R. J. Donnelly and C. F. Barenghi. The observed properties of liquid helium at the saturated vapor pressure. *Journal of Physical and Chemical Reference Data*, 27:1217–1274, 1998.

[31] V. Gadagkar, E. J. Pratt, B. Hunt, M. Yamashita, M. J. Graf, A. V. Balatsky, and J. C. Davis. Generalized rotational susceptibility studies of solid ^{4}He. *Journal of Low Temperature Physics*, 169(3-4):180–196, 2012.

[32] M. J. Graf, Z. Nussinov, and A. V. Balatsky. The glassy response of solid He-4 to torsional oscillations. *Journal of Low Temperature Physics*, 158(3-4):550–559, 2009.

[33] V. N. Grigor'ev, V. A. Maidanov, V. Y. Rubanskii, S. P. Rubets, E. Y. Rudavskii, A. S. Rybalko, Y. V. Syrnikov, and V. A. Tikhii. Observation of a glassy phase of He-4 in the region of supersolid effects. *Physical Review B*, 76(22):224524, 2007.

[34] R. B. Hallock, M. W. Ray, and Y. Vekhov. A summary of mass flux measurements in solid ^{4}He. *Journal of Low Temperature Physics*, 169(3-4):264–277, 2012.

[35] E. Hoskinson, Y. Sato, I. Hahn, and R. E. Packard. Transition from phase slips to the josephson effect in a superfluid ^{4}He weaklink. *Nature Physics*, 2(1):23–26, 2005.

[36] B. Hunt. *Relaxation Dynamics of Solid Helium-4*. PhD thesis, Cornell University, 2009.

[37] B. Hunt, E. Pratt, V. Gadagkar, M. Yamashita, A. V. Balatsky, and J. C. Davis. Evidence for a superglass state in solid ^{4}He. *Science*, 324(5927):632–636, 2009.

[38] I. Iwasa, K. Araki, and H. Suzuki. Temperature and frequency dependence of the sound velocity in hcp ^{4}He crystals. *Journal of the Physical Society of Japan*, 46(4):1119–1126, 1979.

[39] I. Iwasa and H. Suzuki. Sound velocity and attenuation in hcp ^{4}He crystals containing ^{3}He impurities. *J. Phys. Soc. Jpn.*, 49(5):1722–1730, 1980.

[40] Izumi Iwasa. Dislocation-vibration model for nonclassical rotational inertia. *Physical Review B*, 81(10):104527, 2010.

[41] Izumi Iwasa. Switching of dislocations in solid helium between pinned and unpinned states in the torsional oscillator experiments. *Journal of Low Temperature Physics*, 2012. doi: 10.1007/s10909-012-0817-y.

[42] P. Kapitza. Viscosity of liquid helium below the λ point. *Nature*, 141:74, 1938.

[43] Duk Kim and Moses Chan. Absence of supersolidity in solid helium in porous vycor glass. *Physical Review Letters*, 109(15):155301, 2012.

[44] E. Kim and M. H. W. Chan. Observation of superflow in solid helium. *Science*, 305(5692):1941–1944, 2004.

[45] E. Kim and M. H. W. Chan. Probable observation of a supersolid helium phase. *Nature*, 427(6971):225–227, 2004.

[46] M. Kondo, S. Takada, Y. Shibayama, and K. Shirahama. Observation of nonclassical rotational inertia in bulk solid He-4. *Journal of Low Temperature Physics*, 148(5-6):695–699, 2007.

[47] S. E. Korshunov. Two-level systems and mass deficit in quantum solids. *Jetp Letters*, 90(2):156–159, 2009.

[48] A. J. Leggett. Can a solid be superfluid. *Physical Review Letters*, 25(22):1543, 1970.

[49] C. Lie-zhao, D. F. Brewer, C. Girit, E. N. Smith, and J. D. Reppy. Flow and torsional oscillator measurements on liquid helium in restricted geometries under pressure. *Physical Review B*, 33(1):106–117, 1986.

[50] X. Lin, A. C. Clark, and M. H. W. Chan. Probable heat capacity signature of the supersolid transition. *Nature*, 449(7165):1025–1028, 2007.

[51] X. Lin, A. C. Clark, Z. G. Cheng, and M. H. W. Chan. Heat capacity peak in solid He-4: Effects of disorder and He-3 impurities. *Physical Review Letters*, 102(12):125302, 2009.

[52] A. Lisunov, V. Maidanov, V. Rubanskyi, S. Rubets, E. Rudavskii, A. Rybalko, and V. Tikhiy. Search for a disordered phase in solid ^{3}He deformed in situ. *Physical Review B*, 83(13):132201, 2011.

[53] Humphrey Maris. Effect of elasticity on torsional oscillator experiments probing the possible supersolidity of helium. *Physical Review B*, 86(2):020502, 2012.

[54] Humphrey J. Maris and Sebastien Balibar. Effect of helium elasticity on torsional oscillator measurements. *Journal of Low Temperature Physics*, 162(1-2):12–22, 2010.

[55] M. W. Meisel. Supersolid He-4 - an overview of past searches and future possibilities. *Physica B: Condensed Matter*, 178(1-4):121–128, 1992.

[56] Z. Nussinov, A. V. Balatsky, M. J. Graf, and S. A. Trugman. Origin of the decrease in the torsional-oscillator period of solid He-4. *Physical Review B*, 76(1):014530, 2007.

[57] M. Paalanen, D. Bishop, and H. Dail. Dislocation motion in hcp ^{4}He. *Physical Review Letters*, 46(10):664–667, 1981.

[58] Ho Jung Paik. Superconducting tunable-diaphragm transducer for sensitive acceleration measurements. *Journal of Applied Physics*, 47(3):1168, 1976.

[59] A. Penzev, Y. Yasuta, and M. Kubota. Annealing effect for supersolid fraction in He-4. *Journal of Low Temperature Physics*, 148(5-6):677–681, 2007.

[60] A. Penzev, Y. Yasuta, and M. Kubota. ac vortex-dependent torsional oscillation response and onset temperature T_0 in solid He-4. *Physical Review Letters*, 101(6):065301, 2008.

[61] S. V. Pereverzev, A. Loshak, S. Backhaus, J. C. Davis, and R. E. Packard. Quantumoscillations between two weakly coupled reservoirs of superfluid ^{3}He. *Nature*, 388:449–451, 1997.

[62] L. Pollet, M. Boninsegni, A. B. Kuklov, N. V. Prokof'ev, B. V. Svistunov, and M. Troyer. Superfluidity of grain boundaries in solid He-4. *Physical Review Letters*, 98(13):135301, 2007.

[63] E. Pratt. *Superglass Dynamics of Solid Helium*. PhD thesis, Cornell University, 2010.

[64] E. Pratt, B. Hunt, V. Gadagkar, M. Yamashita, M. Graf, A. V. Balatsky, and J. C. Davis. Interplay of rotational, relaxational, and shear dynamics in solid ^{4}He. *Science*, 332:821–824, 2011.

[65] Nikolay Prokof'ev. What makes a crystal supersolid? *Advances in Physics*, 56(2):381–402, 2007.

[66] M. Ray and R. Hallock. Mass flow through solid ^{4}He induced by the fountain effect. *Physical Review B*, 84(14):144512, 2011.

[67] M. W. Ray and R. B. Hallock. Observation of unusual mass transport in solid hcp He-4. *Physical Review Letters*, 100(23):235301, 2008.

[68] M. W. Ray and R. B. Hallock. Observation of mass transport through solid He-4. *Physical Review B*, 79(22):224302, 2009.

[69] M. W. Ray and R. B. Hallock. Observation of thermomechanical equilibration in the presence of a solid He-4 conduit. *Physical Review B*, 82(1):012502, 2010.

[70] L. Reatto. Bose-Einstein condensation for a class of wave functions. *Physical Review*, 183(1):334, 1969.

[71] John D. Reppy, Xiao Mi, Alexander Justin, and Erich J. Mueller. Interpreting torsional oscillator measurements: Effect of shear modulus and supersolidity. *Journal of Low Temperature Physics*, 168(3-4):175–193, 2012.

[72] R. C. Richardson and E. N. Smith. *Experimental Techniques in Condensed Matter Physics at Low Temperatures*. Key-Westview, Boulder, 1998.

[73] A. S. C. Rittner, W. Choi, E. J. Mueller, and J. D. Reppy. Absence of pressure-driven supersolid flow at low frequency. *Physical Review B*, 80(22):224516, 2009.

[74] Ann Rittner and John Reppy. Observation of classical rotational inertia and nonclassical supersolid signals in solid He-4 below 250 mk. *Physical Review Letters*, 97(16):165301, 2006.

[75] Ann Rittner and John Reppy. Disorder and the supersolid state of solid He-4. *Physical Review Letters*, 98(17):175302, 2007.

[76] Ann Rittner and John Reppy. Probing the upper limit of nonclassical rotational inertia in solid helium 4. *Physical Review Letters*, 101(15):155301, 2008.

[77] Xavier Rojas, Ariel Haziot, Victor Bapst, S. Balibar, eacute, bastien, and Humphrey J. Maris. Anomalous softening of ^{4}He crystals. *Physical Review Letters*, 105(14):145302, 2010.

[78] S. Sasaki, F. Caupin, and S. Balibar. Wetting properties of grain boundaries in solid He-4. *Physical Review Letters*, 99(20):205302, 2007.

[79] S. Sasaki, R. Ishiguro, F. Caupin, H. J. Maris, and S. Balibar. Superfluidity of grain boundaries and supersolid behavior. *Science*, 313(5790):1098–1100, 2006.

[80] S. I. Shevchenko. One-dimensional superfluidity in Bose crystals. *Sov. J. Low Temp. Phys.*, 13:61, 1987.

[81] J. J. Su, M. J. Graf, and A. V. Balatsky. Glass anomaly in the shear modulus of solid He-4. *Physical Review Letters*, 105(4):045302, 2010.

[82] J. J. Su, M. J. Graf, and A. V. Balatsky. A glassy contribution to the heat capacity of hcp He-4 solids. *Journal of Low Temperature Physics*, 159(3-4):431–440, 2010.

[83] Jung-Jung Su, Matthias J. Graf, and Alexander V. Balatsky. Shear modulus in viscoelastic solid ^{4}He. *Journal of Low Temperature Physics*, 162(5-6):433–440, 2010.

[84] Jung-Jung Su, Matthias J. Graf, and Alexander V. Balatsky. The role of glassy dynamics in the anomaly of the dielectric function of solid helium. *New Journal of Physics*, 13(11):113024, 2011.

[85] H. Suzuki. Plastic flow in solid helium. *Journal of the Physical Society of Japan*, 35(5):1472–1479, 1973.

[86] H. Suzuki. Plastic flow in hcp ^{4}He. II. *Journal of the Physical Society of Japan*, 42(6):1865–1872, 1977.

[87] B. Svistunov. Supersolidity of helium-4: Disordered scenarios. *Physica B-Condensed Matter*, 404(3-4):521–523, 2009.

[88] O. Syshchenko, J. Day, and J. Beamish. Frequency dependence and dissipation in the dynamics of solid helium. *Physical Review Letters*, 104(19):195301, 2010.

[89] Ka-Ming Tam, Scott Geraedts, Stephen Inglis, Michel J. P. Gingras, and Roger G. Melko. Superglass phase of interacting bosons. *Physical Review Letters*, 104(21):215301, 2010.

[90] D. J. Thouless. Flow of a dense superfluid. *Annals of Physics*, 52(3):403, 1969.

[91] D. R. Tilley and J. Tilley. *Superfluidity and Superconductivity*. IOP, Bristol, 3 edition, 1990.

[92] R. Wanner, I. Iwasa, and S. Wales. Evidence for dislocations in solid h.c.p. helium-4 from sound velocity experiments. *Solid State Communications*, 18:853–856, 1976.

[93] J. S. Wu and P. Phillips. Minimal model for disorder-induced missing moment of inertia in solid He-4. *Physical Review B*, 78(1):014515, 2008.

[94] C. D. Yoo and A. T. Dorsey. Theory of viscoelastic behavior of solid He-4. *Physical Review B*, 79(10):100504, 2009.